INFORMATION TO USERS

This manuscript has been reproduced from the microfilm master. UMI films the text directly from the original or copy submitted. Thus, some thesis and dissertation copies are in typewriter face, while others may be from any type of computer printer.

The quality of this reproduction is dependent upon the quality of the copy submitted. Broken or indistinct print, colored or poor quality illustrations and photographs, print bleedthrough, substandard margins, and improper alignment can adversely affect reproduction.

In the unlikely event that the author did not send UMI a complete manuscript and there are missing pages, these will be noted. Also, if unauthorized copyright material had to be removed, a note will indicate the deletion.

Oversize materials (e.g., maps, drawings, charts) are reproduced by sectioning the original, beginning at the upper left-hand corner and continuing from left to right in equal sections with small overlaps. Each original is also photographed in one exposure and is included in reduced form at the back of the book.

Photographs included in the original manuscript have been reproduced xerographically in this copy. Higher quality 6" x 9" black and white photographic prints are available for any photographs or illustrations appearing in this copy for an additional charge. Contact UMI directly to order.

UMI

A Bell & Howell Information Company
300 North Zeeb Road, Ann Arbor MI 48106-1346 USA
313/761-4700 800/521-0600

Investigation of Current and Novel Rectangular Dielectric Resonator Antennas for Broadband Applications at L-Band Frequencies

by
Michael Cooper, B. Eng

A thesis submitted in partial fulfilment
of the requirements for the degree of
Master of Engineering.

Ottawa-Carleton Institute for Electrical Engineering
Faculty of Engineering
Department of Electronics
Carleton University
Ottawa, Canada

Acceptance Form

The undersigned hereby recommend to
the Faculty of Graduate Studies and Research
acceptance of the thesis

Investigation of Current and Novel
Rectangular Dielectric Resonator Antennas
for Broadband Applications at L-Band Frequencies

Submitted by
Michael Cooper, B. Eng.

In partial fulfilment of the requirements for the degree of
Master of Engineering.

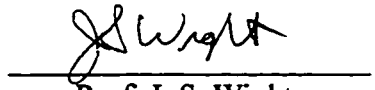

Prof. J. S. Wight,
thesis co-supervisor

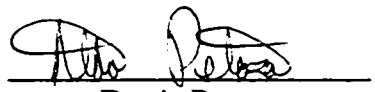

Dr. A. Petosa
thesis co-supervisor

Chair,
Department of Electronics

Carleton University
July 1997

Abstract

The rectangular dielectric resonator antenna (DRA) is investigated for potential use in broad band L-Band applications. This thesis presents experimental verification of the existing theory and implementations of the rectangular DRA as a linearly, dual linearly or circularly polarized antenna. A novel modification, edge-grounding, to the rectangular dielectric resonator antenna is proposed for increasing the bandwidth of a compact DRA. Experimental and analytic work on the novel edge-grounded DRA is presented. The edge-grounded technique applied to the broad band multi-segment DRA, several stacked layers of material with different dielectric constants, results in an antenna element with a bandwidth similar to the multi-segment DRA, but with a significantly more compact geometry. The results presented on the existing and novel broad band performance of the compact rectangular dielectric resonator antenna demonstrate that it has potential for application in the new L-band personal and satellite communication services.

Acknowledgement

I would like to thank those who helped me during the development of this thesis especially all the staff at the Communications Research Centre and Carleton University, my fellow grad students, my friends, and my supervisors Dr. A. Petosa and Professor J.S. Wight.

Table of Contents

List of Figures viii

List of Tables x

List of Appendices xi

Chapter 1
Introduction 1
1.1 Trends in Personal Wireless Communications 1
1.2 L-Band Wireless Applications 2
1.2.1 PCS 1.9 Benchmark 2
1.2.2 MSAT Benchmark 3
1.3 Microstrip Patch Antennas 5
1.3.1 Dual Polarization 5
1.3.2 Circular Polarization 7
1.4 Dielectric Resonator Antennas 7
1.4.1 History of Dielectric Resonators 7
1.4.2 Linear Polarization 9
1.4.3 Circular Polarization 15
1.4.4 Linear Arrays 16
1.4.5 Numerical Methods 16
1.5 Thesis Objectives 17
1.6 Thesis Methodology 18
1.6.1 Experimental Work 18
1.6.2 Analytic Work 19

Chapter 2
Rectangular Dielectric Resonator Antenna Theory 21
2.1 Introduction 21
2.2 Truncated Dielectric Waveguide Model 22
2.2.1 Resonant Frequency 24
2.2.2 Field Structure of TE_{111} Mode 26
2.2.3 Impedance Bandwidth 30
2.3 Circular Polarization 33
2.4 Radiation Pattern 39
2.5 DRA Geometry - Bandwidth Effect 40
2.6 Triangular Dielectric Resonator Antenna 47

Chapter 3
Experimental Results 51
3.1 Introduction 51
3.2 Feed Excitation Structures 53
3.2.1 Probe Feed Excitation 54
3.2.2 Aperture Feed Excitation 57
3.2.3 Direct Microstrip Feed Excitation 60
3.3 Linear Polarization 62
3.3.1 Resonant Frequency and Bandwidth 62
3.3.2 Accuracy of Theoretical Calculations 65
3.3.3 Radiation Pattern 67
3.4 Dual Linear Polarization 68
3.5 Circular Polarization 72
3.5.1 Experimental Results 72
3.5.2 Practical Usefulness 74
3.6 Parasitic Array 75
3.6.1 Experimental Results 75
3.6.2 Practical Usefulness 76

Chapter 4
Multi-Segment Rectangular DRA 79
4.1 General 79
4.2 DRA Bandwidth Standard Comparison 80
4.3 Introduction 82
4.4 Theoretical Analysis 85
4.5 Experimental Results 90
4.6 Comparison of Theoretical and Experimental Results 91
4.7 Other Broadband DRA Structures 94
4.8 Practical Usefulness 94

Chapter 5
Novel Edge-Grounded Rectangular DRA 96
5.1 Introduction 96
5.2 Homogeneous DRA 98
5.2.1 Resonant Frequency 98
5.2.2 Impedance Bandwidth 101
5.2.3 Experimental Results 104
5.2.4 Comparison of Measurement and Theory 104
5.2.5 Practical Usefulness 105
5.3 Multi-Segment DRA 106
5.3.1 Introduction 106
5.3.2 Theoretical Analysis 106

5.3.3 Experimental Results 110
5.3.4 Comparison of Theoretical and Experimental Results 111
5.3.5 Practical Usefulness 112

Chapter 6
Conclusions and Recommendations 114
6.1 General 114
6.2 Objectives Accomplished 115
6.2.1 Experimental 115
6.2.2 Analytical 116
6.3 Significance of This Work 116
6.4 Future Work 117

References 118

List of Figures

Figure 1.1 Half and Quarter Wavelength Array Spacing for Large Angle Beam Squinting 4
Figure 1.2 Microstrip Patch Antenna 6
Figure 1.3 Dielectric Resonator Antenna 8
Figure 1.4 Experimental Millimetric Array 10
Figure 1.5 Cylindrical, Rectangular, Hemispherical Probe Fed DRA 12
Figure 1.6 Direct Microstrip, Microstrip to Aperture, and Coplanar Waveguide Feed to Cylindrical DRA 12
Figure 1.7 Radiation Modes of Cylindrical DRA 14
Figure 1.8 Modified and Novel Rectangular Dielectric Resonator Antennas 20

Figure 2.1 Rectangular Dielectric Waveguide and Resonator Geometry 23
Figure 2.2 Orientation of Transverse E-field for Lowest Order Mode of Isolated Rectangular DR and DR on Ground Plane. 29
Figure 2.3 Phase Design for Single Feed Rectangular DRA 36
Figure 2.4 Orientation of Single Slot Fed Rectangular DRA, With Linear Modes Illustrated 37
Figure 2.5 Orientation of Single Slot Fed Cruciform DRA, With Linear Modes Illustrated 38
Figure 2.6 Cubic, Low Profile and Thin Transverse Dimension DRA Shapes 41
Figure 2.7 Plot of Bandwidth vs Normalized Width for ε_r=10 to 100 43
Figure 2.8 Plot of Bandwidth vs Aspect Ratio for ε_r=20 44
Figure 2.9 Plot of Bandwidth vs Dielectric Constant for Fixed Width 45
Figure 2.10 Plot of Normalized Width vs Bandwidth for Thin Transverse and Low Profile DRA Geometries 46
Figure 2.11 Dimensions of Triangular Dielectric Resonator and Slot Feed Circuit . . 49
Figure 2.12 Orientation of Transverse E-field for Lowest Order Mode of Rectangular DRA 50

Figure 3.1 Dimensions of Rectangular DRA and Probe Feed 55
Figure 3.2 Dimensions of Rectangular DRA and Aperture Feed 58
Figure 3.3 Dimensions of Rectangular DRA and Direct Microstrip Feed 61
Figure 3.4 Plot of Resonant Frequency Prediction for Linearly Polarized Square DRA 66
Figure 3.5 Typical Measured Radiation Pattern for DRA 69
Figure 3.6 Dual Linearly Polarized Probe Fed DRA 71
Figure 3.7 Dual Linearly Polarized 4 Element Parasitic Array of DRA 77
Figure 3.8 Measured Radiation Pattern 4 Element Parasitic Array of DRA 78

Figure 4.1 Dimensions of Rectangular Multi-Segment DRA and Probe Feed 81
Figure 4.2 Probe Through Ground Plane Versus Probe From Microstrip Line 84
Figure 4.3 Limit Cases of Thin and Thick Lower Segments 86
Figure 4.4 Conceptual Orientation of Transverse Electric Field for Multi-segment DRA 87

Figure 5.1 Dimensions of Rectangular Edge-grounded DRA and Probe Feed 97
Figure 5.2 Orientation of Transverse Electric Field for Lowest Order Mode 99
Figure 5.3 Dimensions of Rectangular Edge-grounded Multi-segment DRA and Probe Feed 107
Figure 5.4 Conceptual Orientation of Transverse Electric Field for Edge-grounded Multi-segment DRA 109

List of Tables

Table 2.1 Comparison Triangular DRA Design Theory With Reported Measurement . 48

Table 3.1 Dimensions, Theoretical Values for Resonant Frequency and Bandwidth . . 53
Table 3.2 Slot Feed Dimensions 59
Table 3.3 Experimental Results using Probe Feeds 63
Table 3.4 Experimental Results using Aperture Feeds 64
Table 3.5 Experimental Results using Direct Microstrip Feeds 65
Table 3.6 Prediction Error for Rectangular DRA Theory 67
Table 3.7 Theoretical Values of CP Designed DRA 72
Table 3.8 Linear Polarization Measurements on CP DRA 73
Table 3.9 Prediction Error for CP DRA 73
Table 3.10 Circular Polarization Measurements on CP DRA 74

Table 4.1 Results of Probe Fed DRAs on Ground Plane and on Dielectric Substrate . . 83
Table 4.2 Prediction of Multi-Segment DRA using Average Dielectric Constant 89
Table 4.3 Multi-Segment DRA Broad Band Results 90
Table 4.4 Effect of Probe Length on Resonance of Multi-Segment DRA 91
Table 4.5 Prediction Error for Average Dielectric Constant Technique 92
Table 4.6 DRA Standard Using the Measured Value of Resonant Frequency 92
Table 4.7 Multi-Segment Bandwidth Increase 93

Table 5.1 Edge-Grounded DRA Theoretical Values 103
Table 5.2 Edge-grounded DRA Measurements 104
Table 5.3 Prediction Error for Edge-Grounded DRA Theory 105
Table 5.4 Multi-Segment Edge-Grounded DRA Limiting Resonances 108
Table 5.5 Resonant Frequency Prediction for Multi-Segment Edge-Grounded DRA . 110
Table 5.6 Multi-Segment Edge-Grounded DRA Measurements 110
Table 5.7 Prediction Error : Multi-Segment Edge-Grounded DRA 111
Table 5.8 Bandwidth of DRA Standard 111
Table 5.9 Multi-Segment Edge-Grounded DRA Bandwidth Increase 112

List of Appendices

Appendix A
Direct Microstrip Feed Measurements 124

Appendix B
Linear Pattern Simulation vs Measurement 128

Appendix C
Dual Polarization Isolation Measurements 131

Appendix D
Rectangular Circularly Polarized DRA Measurements 134

Appendix E
Multi-Segment Rectangular DRA Network Analyser Measurements 137

Appendix F
Edge-Grounded Rectangular DRA Measurements 141

Chapter 1

Introduction

1.1 Trends in Personal Wireless Communications

There is currently a world wide expansion in the area of personal communications services. In some areas this is being driven by the introduction of wireless communication service to remote, rugged or underdeveloped regions where there was previously few communication services at all. The services are being provided by land based specialized mobile radio systems and by satellite, both in point-to-point and point-to-multi-point configurations. The wireless implementation has the advantage of relatively rapid roll-out, compared to infrastructure required for wired systems. This is especially true in the area of satellite communications where coverage areas of existing satellites are large and only a user terminal is required for wireless access. In more heavily populated and developed regions the most common personal wireless service in use is the cellular phone. With the advent of digital technology, messaging, fax, email and other services are being included with the basic voice service, helping fuel a rapid growth in this area.

1.2 L-Band Wireless Applications

Many of the above mentioned services are operating at L-band, the frequency band from 1 to 2 Gigahertz (GHz). Wireless applications currently operating at L-Band include the global positioning system (GPS), the new digital personal communications service - denoted PCS 1.9 in North America and 1.8 in Europe, the mobile communications satellite services INMARSAT and MSAT, proposed globally accessible systems such as Iridium and other SMR distribution systems.

The antenna is a critical component of the wireless system because it is the interface between the mobile user and the service provider. At L-Band the wavelength is short enough for the formation of precision directional and shaped beams at the basestation, and terminal in the case of the satellite services. At the terminal end, the antenna is small enough to be portable, and the field of integrated circuit design is mature for the mass production of these units to be economically feasible. The trends in antenna design are similar to those of any electrical device - towards structures of smaller size and lighter weight which are cheaper and more efficient.

Although the design of antenna systems was not the focus of this thesis, the potential for practical system implementation of the antennas that were investigated was evaluated. The two Canadian mobile communications services chosen as the benchmarks for this purpose were PCS 1.9 and MSAT.

1.2.1 PCS 1.9 Benchmark

The PCS 1.9 digital mobile wireless communications service operates in the frequency band 1.85 to 1.99 GHz, a relative bandwidth of 7.3 %, and uses linear polarization (typically vertical transmission from the basestation). The basestation and terminal unit antenna requirements are quite different. The most important requirement for the terminal unit is portability, meaning the antenna must be compact and efficient - to

extend the battery life. However, the performance of the antenna is strongly affected by the design of the terminal unit and its operating environment [1]. Since that was not the focus of this thesis, the portable unit was not considered.

The basestation antenna is commonly implemented as a vertically oriented array. The requirements for the array are high power handling, vertical beam shaping, and linear, dual linear, or circular polarization. Typical electrical specifications for these antenna are a SWR of 1.3 to 1.5, an azimuth plane radiation pattern of 30 to 120 degrees, beam pattern shaping and tilting in the elevation plane. To achieve the standard level of beam shape [2] the array element spacing will be approximately 0.75 wavelength (λ_0). To improve the received signal quality diversity antennas have been investigated. These include orthogonal linear polarization (which will be called dual polarization in this thesis although strictly speaking the term dual is not limited to the case of orthogonal linear polarizations of the same frequency), and circular polarization. The current specification for dual polarization PCS basestation antennas is for an isolation of 30 dB between the two ports [Microcell 97].

1.2.2 MSAT Benchmark

The MSAT mobile communications system operates in the frequency band of 1.53 to 1.66 GHz, a relative bandwidth of 8.7 %. The service is circular polarization, right-hand direction, since the orientation of the user terminal with respect to the geosynchronous satellite will vary. The terminal implementation relevant to this thesis would be similar to a planar array for use on a car such as in [4]. This antenna must be able to tilt the beam peak towards the zenith, since across Canada the MSAT satellite will be 10 to 50 degrees above the horizon. To achieve this degree of beam tilt from a planar array oriented horizontally, the array elements will be spaced less than $0.5\lambda_0$ apart, Figure 1.1.

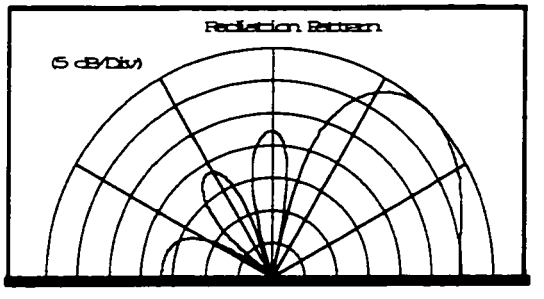

array element spacing = 0.25 λ_0
$\Delta\phi$ = 63.5 deg

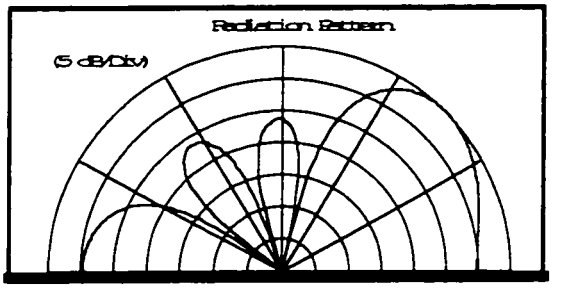

array element spacing = 0.5 λ_0
$\Delta\phi$ = 127 deg

Figure 1.1
Half and Quarter Wavelength Array Spacing for Large Angle Beam Squinting

1.3 Microstrip Patch Antennas

The most common array element used in the arrays described above is the microstrip patch antenna. A typical microstrip patch antenna is shown in Figure 1.2. It consists of an arbitrarily shaped metal layer on a substrate backed by a ground plane. The structure can include multiple metal and dielectric layers. Typical patch dimensions are on the order of $\lambda_g/3$ to $\lambda_g/2$, where the guided wavelength depends of the dielectric constant and the dimension of the antenna. Feed excitation of the antenna has been demonstrated with edge-fed, slot-coupled, proximity-coupled and probe-coupled techniques.

The extensive use of microstrip antennas is a result of their low cost, light weight, reproducibility and size (low profile) when compared to more traditional antennas such as the horn, reflector or dipole. The disadvantages of microstrip antennas such as narrow bandwidth (1-6%), surface wave excitation and conductor losses are more significant at higher frequencies than L-Band [5] [6]. Techniques for increasing the impedance bandwidth by using an air dielectric substrate or stacked patches are more easily implemented at L-Band where there are lower conductor losses, and less stringent dimensional fabrication tolerances.

1.3.1 Dual Polarization

This section is not representative of the state of the art of microstrip patch implementation, but is rather an example of recently published work in the field. Using a ring microstrip antenna, a cross slot feed and a three layer dielectric (the metal layers were patch : feed line : crossed slot : feed line) a port to port isolation of 20 dB across the 3% bandwidth was measured by Sawamura [7]. Roston used offset slots and a foam dielectric for the patch to achieve an isolation of 22dB for an impedance bandwidth (SWR < 1.5) of 9.3% [8].

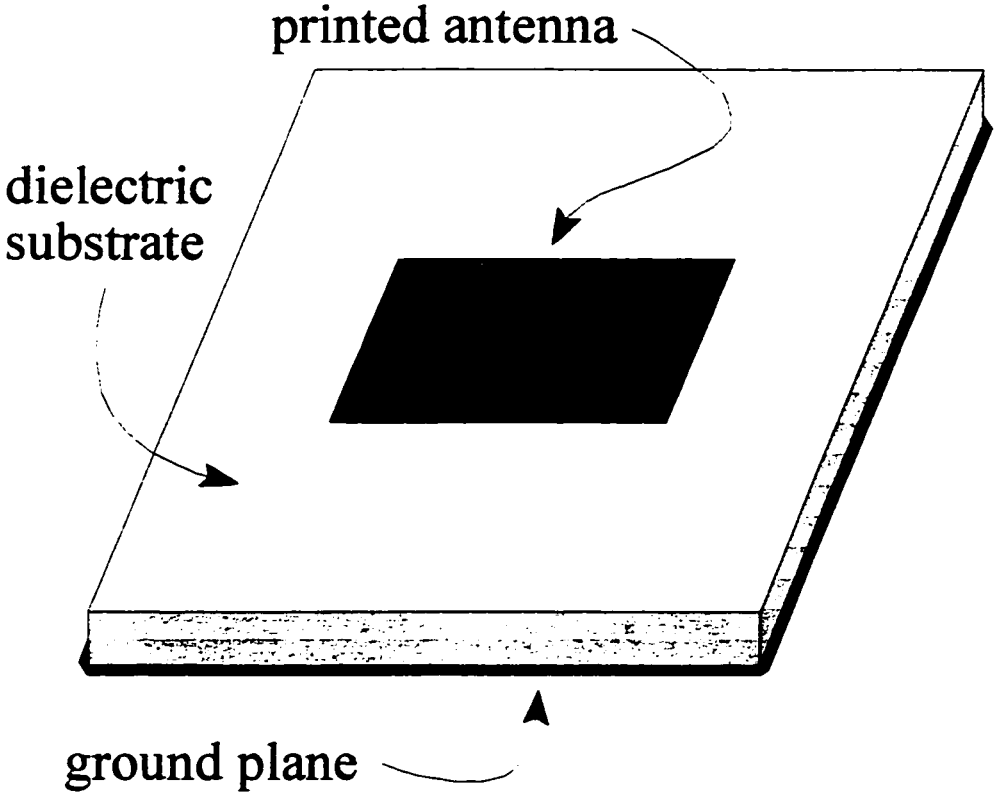

Figure 1.2
Microstrip Patch Antenna

1.3.2 Circular Polarization

Iwasaki reported on a single proximity feed rectangular microstrip patch. The impedance bandwidth was 3.5% and the axial ratio bandwidth was 0.55% for the single patch, and using sequential rotation for an array of six patches an impedance bandwidth of 11.6% and a 3dB axial ratio of 6% was achieved [9]. The sequential rotation technique for improving the axial ratio bandwidth of circularly polarized arrays is applicable for boresight beams such as in [9].

Telikepalli of CAL presented a comparison of stacked patches, the first being two solid squares, and the second a slotted feed patch with a square parasitic patch [10]. The bottom patch was fed in phase quadrature to generate circular polarization. The slotted patch had a 3dB beamwidth of 98 degrees as compared to 78 degrees for the solid patch. In terms of circular polarization performance, this corresponded to an axial ratio 0.75 dB less at low elevation angles for the slotted antenna. In a scanned array implementation the wide beam slotted antenna improved the gain by 0.9dB, at an elevation angle of 35 degrees, 2 degrees lower than the solid element. This result illustrates the advantage of using an element with a wide beamwidth in both principal planes for titled beam applications.

A third circularly polarized microstrip patch antenna was developed by Huang [11]. The feed patch of a four element Yagi-Uda planar array (2 directors, 1 reflector) was fed in phase-quadrature, generating a circularly polarized pattern at 20 to 60 degrees above the horizon. Four of the Yagi-Uda arrays were combined to achieve a minimum gain of 10dBic across the MSAT bandwidth.

1.4 Dielectric Resonator Antennas

1.4.1 History of Dielectric Resonators

A dielectric resonator (DR) consists of an arbitrarily shaped low-loss temperature

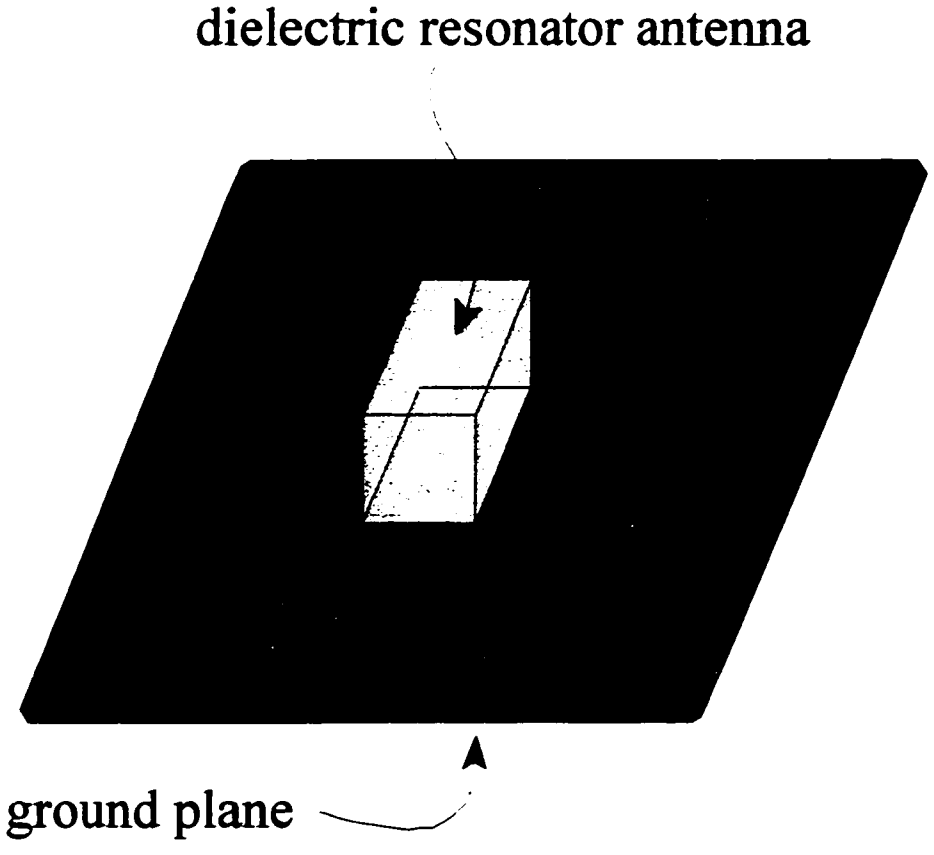

Figure 1.3
Dielectric Resonator Antenna

stable material as in Figure 1.3. The use of dielectric resonators was first proposed by Richtmeyer in 1939 [12]. It was not until 1962 when the first experimental results on the use of single Rutile crystals as resonators was demonstrated [13]. In the late 1970's the first low-loss temperature stable material, Barium Tetritnade, was created [14].

The first use of the dielectric resonator was in microwave circuit applications. In 1968, a high permittivity dielectric resonator was demonstrated to occupy only 3 to 5% of the volume of an equivalent waveguide filter, traditional technology at the time [15]. To use DR in circuit implementations, there must be available a knowledge of the properties of the DR; resonant frequency, Q-factor, modes and coupling characteristics to circuit components. Early theoretical and experimental work on dielectric resonators includes; resonant frequencies and modes of the DR by Yee [16], and experimental data on circuit implementations by Karp [17].

Significant theoretical work on the modal and resonant behaviour of low-loss, very high permittivity resonators was done by Van Bladel [18] [19]. Further work on analytic models based on variations of the dielectric waveguide model developed through the work of Okaya&Barash and Marcatili [20] yielded more accurate determinations of DR circuit properties [21] [22] [23]. With computers, the application of numerical methods to electromagnetic problems in the 1980's lead to the solution of resonant frequency and Q-factor for many shapes of dielectric resonators, summarized in [24].

1.4.2 Linear Polarization

Richtmeyer suggested in 1939 that a dielectric resonator must radiate. The electromagnetic fields in a DR used in a circuit application are contained by a surrounding metallic surface. With an air boundary, it is evident that there will be some radiation from the DR. In 1981, in what may be the first reported use of the dielectric resonator as an

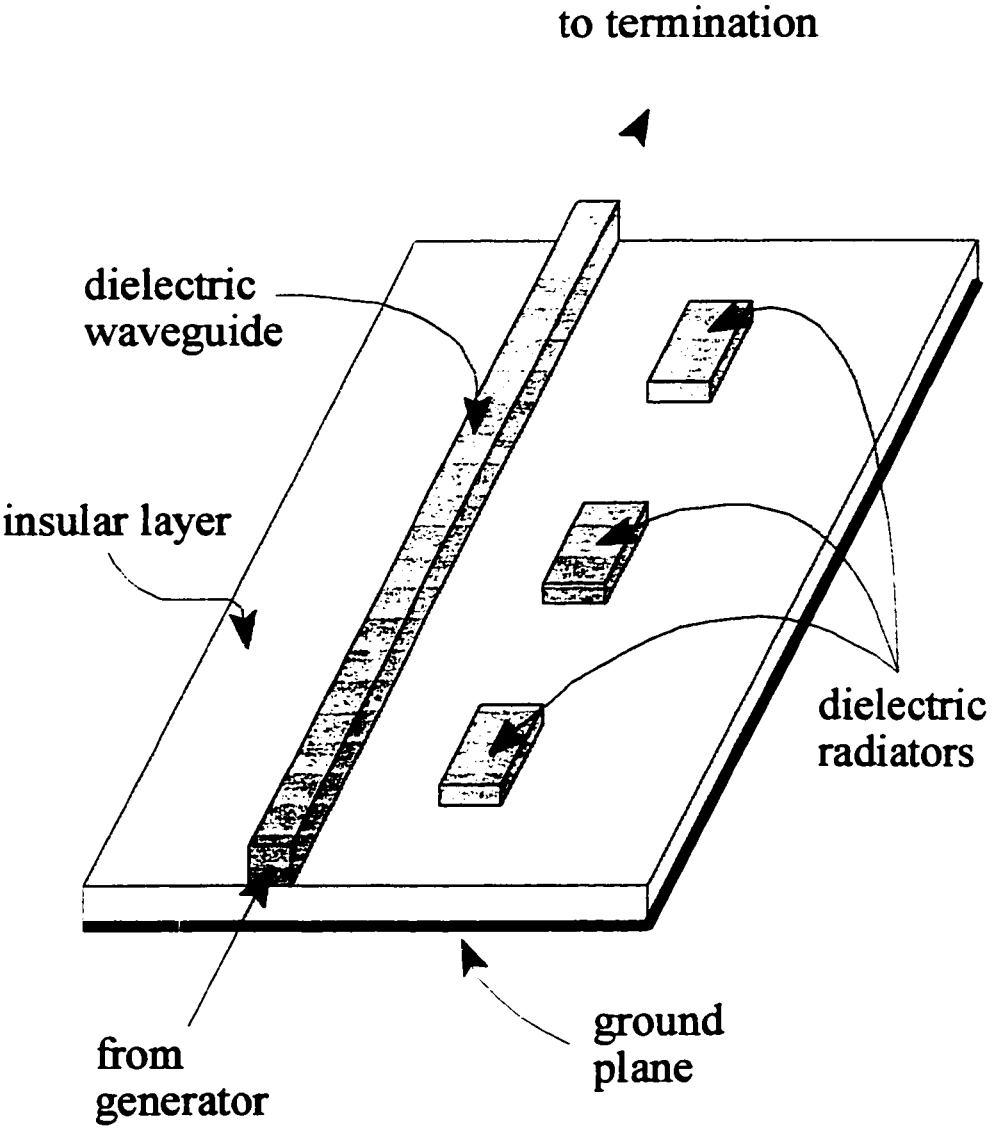

Figure 1.4
Experimental Millimetric Array

antenna, a linearly polarized array of dielectric resonators proximity fed by a dielectric waveguide on a ground plane was presented by Birand and Gelsthorpe [25], Figure 1.4.

Subsequently, extensive work on single element linearly polarized DRA was done by Long and McAllister, et al. Rectangular, cylindrical, and hemispherical DRA were excited by a probe through a ground plane, Figure 1.5 [26] [McAllister 83]. For the lowest order resonance of all three shapes, they observed efficient radiation in the direction normal to the ground plane. It was found that varying the position and the length of the probe could be used to better match the DRA to the feed. Due to the spherical symmetry of the hemisphere, its geometry is separable, and an exact analysis of the air/dielectric interface is possible. They observed that approximating all walls as perfect magnetic conductors (PMC) gave accurate results for the cylindrical geometry. For the analysis of the rectangular resonator, this model was replaced by a truncated dielectric waveguide with PMC walls to better approximate the resonance of the rectangular geometry.

Following the pioneering work by Long and McAllister, different feed excitations of those three shapes of DRA have been reported, Figure 1.6. Kranenburg & Long excited a cylindrical DRA by slightly overlapping an open circuited microstrip feed line [28]. St-Martin, et al, used a non-resonant slot fed by a microstrip transmission line to excite a cylindrical DRA [29]. Kranenburg also used a co-planar waveguide to feed a cylindrical DRA [30]. These new coupling techniques have the advantages of simple fabrication and integration with microwave integrated circuits. The other shapes have been similarly excited, aperture coupling to the rectangular DRA [31] and to the hemispherical DRA [32] were demonstrated. In that same paper, Ittipiboon also demonstrated aperture coupling to a triangular cross section DRA.

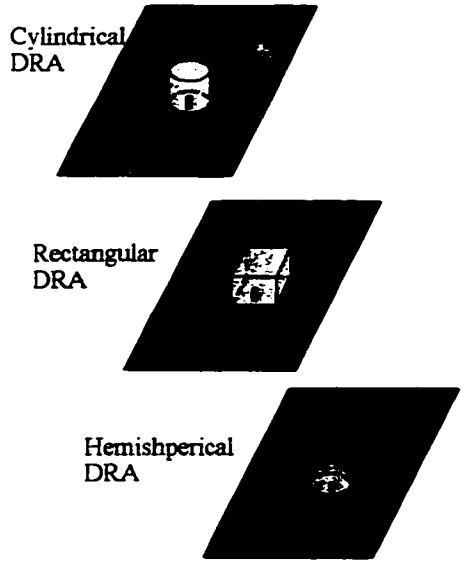

Figure 1.5
Cylindrical, Rectangular, Hemispherical Probe Fed DRA

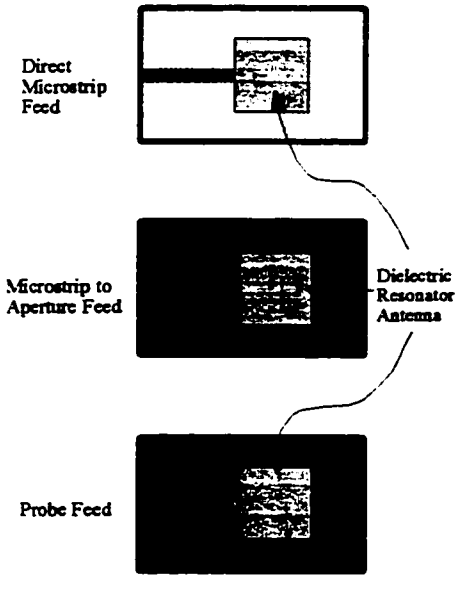

Figure 1.6
Direct Microstrip, Microstrip to Aperture, and
Coplanar Waveguide Feed to Cylindrical DRA

Several stacked and parasitic DRA configurations have been demonstrated that increase the bandwidth of the cylindrical DRA. Kishk used a probe to excite a stacked cylindrical DRA, the top resonator designed to resonate at 12 GHz and the larger bottom resonator at 10 GHz, both resonators made of a dielectric with ε_r=10.5 [33]. An impedance bandwidth for a SWR < 2 of 25% was reported, over twice the bandwidth of the single element. Simons & Lee also demonstrated an impedance bandwidth increase through the use of parasitic DRA [34]. Shum excited a stacked annular ring DRA by an axi-symmetric probe [35]. The DRA were separated from each other and the ground plane by a small air gap. The original element had a 5% bandwidth, the addition of the air gap improved this to 10% and the addition of a second element increased the bandwidth to 18%.

Dr Mongia made significant contributions to the study of DRA. In [36] he quantified the radiation modes of the cylindrical resonator, see Figure 1.7, and developed analytic expressions for determining the resonant frequency of these modes. The previously described cylindrical and rectangular DRA were excited in the lowest order mode which radiates like a horizontal magnetic dipole. Mongia proposed and investigated a half split cylindrical DRA. This DRA was excited by a probe [23] and an aperture [37]. Mongia demonstrated the first electric monopole mode antenna, an annular dielectric ring fed in the centre with a probe [38], the same configuration that Shum later used in a stacked arrangement. In [39], the results of an investigation of the efficiency of the DRA were presented, with typical efficiency values of 98 % reported.

Up to this point the largest value of dielectric constant used in DRA was around 40. Mongia reported in [40], a low profile rectangular DRA with ε_r=100 excited by a microstrip fed aperture in the horizontal magnetic dipole mode. An impedance bandwidth of 3% was reported. In [41], an aperture coupled cylindrical DRA designed to resonate in the magnetic quadrupole mode was presented.

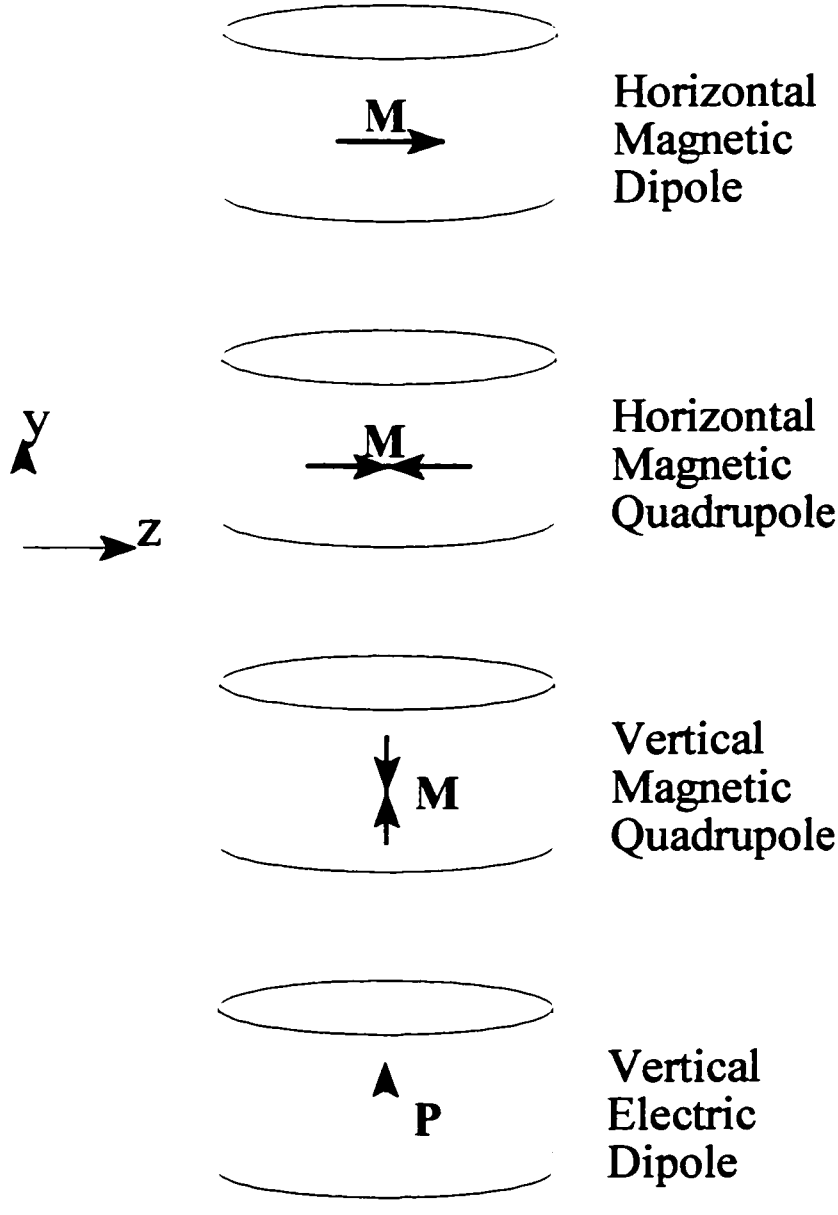

Figure 1.7
Radiation Modes of Cylindrical DRA

Petosa reported in [42] a direct microstrip fed multi-segment DRA. As opposed to the previous stacked antennas, the both layers of dielectric were not resonant. The lower layer, ε_r =40, was used to increase the coupling to the microstrip line, which was reported to be weak when only the upper resonant segment, ε_r = 10, was used.

1.4.3 Circular Polarization

The dielectric resonator antenna is a linearly polarized antenna. When excited in the fundamental mode it radiates a primarily linearly polarized wave. To produce circularly polarized radiation from a linearly polarized antenna requires radiating two fields of equal amplitude in space-phase quadrature in the far-field, which when combined form circular polarization. This can be done by simultaneously exciting multiple modes with a single feed, or using multiple feeds to individually excite the modes on one or more elements. Several circularly polarized DRA have been reported.

Haneishi and Takazawa implemented a planar array of chopped corner DRA [43]. The 2dB axial ratio bandwidth for the individual element was 3%. The elements were paired using sequential rotation to improve the boresight axial ratio bandwidth to 15%.

Mongia presented in [44] an annular probe fed DRA. The two probes excited the two orthogonal $HE_{11\delta}$ modes in phase quadrature through the use of a directional coupler. The limiting factor for this type of antenna was the impedance bandwidth and not the axial ratio. The directional coupler was able to maintain the phase-quadrature and equal amplitude conditions of the two linear modes over a much broader bandwidth than the antenna could efficiently radiate.

The cruciform shaped circularly polarized DRA was developed by Ittipiboon [45]. This antenna is formed from two linearly polarized DRA elements of different lengths, oriented 90 degrees with respect to each other, excited by an aperture oriented at 45 degrees with respect to the linear elements, Figure 2.5. This antenna produced a 3dB axial

ratio over a wide 100 degree beamwidth, with a bandwidth of 4% for the same 3dB axial ratio (ε_r=10.8).

Finally, Oliver generated circular polarization from a single rectangular DRA excited by an aperture, Figure 2.4, or by a probe [46]. A 3dB axial ratio bandwidth of 6.6% was measured for the lowest permittivity (ε_r=10) element, and the same wide beam as observed by Ittipiboon.

1.4.4 Linear Arrays

Several arrays of DRA have been reported after the first one by Birand & Gelsthorpe. Petosa demonstrated a similar dielectric waveguide fed array of DRA in [47]. Microstrip fed arrays of DRA, where the DRA are loosely coupled to a microstrip line instead of the dielectric waveguide were shown in [48] [49]. Petosa also showed passive beam scanning with a four element parasitic array where the single driven DRA is excited by an aperture. The paired resonators of Haneishi and Takazawa were integrated into a 4x4 array. In [50] Loos investigated the coupling between linearly polarized DRA, and integrated a 2x2 array.

1.4.5 Numerical Methods

With the speed and power of the computer today, many DRA geometries have been numerically solved. The numerical techniques used include the method of moments (MoM), the finite element method (FEM), the finite-difference time domain method (FDTD) and the transmission line matrix method (TLM). Kishk used the MoM to predict the radiation performance of a probe fed cylindrical resonator, including the effects of a finite sized ground plane [51]. Leung used the MoM to calculate the input impedance and radiation patterns of the first three modes of the hemispherical DRA using a probe feed [52] and an aperture feed [53]. The FDTD method was used by Shum and Luk to predict return loss for an aperture fed rectangular DRA [54]. Dhouib used the TLM method to also analyse the return loss of the rectangular DRA with aperture coupling [55]. Carrie

reported a similar TLM method for calculating the radiation of the circularly polarized cruciform DRA, reported by Ittipiboon, singly and inside a metal cavity topped with a radome [56]. Finally, Faggetter developed a moment method specific to the dielectric resonator where the fields in and outside the resonator are assumed to be produced by a mesh of equivalent electric surface currents of the dielectric boundary, which was shown to substantially reduce the matrix size required for computation [57]. This technique was applied to the resonators of [26] with good agreement for the calculated input impedance.

1.5 Thesis Objectives

There is a need for compact broadband antennas for linear, dual and circular polarization applications. Research to date has focussed on higher frequencies, 6 to 40 GHz, where dielectric resonator antennas have demonstrated superior performance to microstrip patch antennas. For dielectric resonator antennas to be useful at L-Band, they must demonstrate comparable performance to microstrip patch technology in terms of size, complexity, ease of implementation, as well as meeting the same electrical specifications.

The dielectric resonator antenna has been shown to radiate a wide beam pattern with low cross polarization, to be easily excited by numerous feed structures, to have a broadband impedance performance, to be able to radiate circular polarization, to have a high efficiency, and to be compact. Can it meet the performance specifications of Sections 1.2.1 & 1.2.2 with a simple design procedure and compact element comparable to existing technology?

The geometry that will be investigated is the rectangular dielectric resonator antenna with two orthogonal lowest order modes that can be used in dual and circular polarization applications. There is not a lot of detailed analytic work on the rectangular shape, making it a good candidate for extensive experimental testing for the purposes of

gathering more data on this shape. The ability of existing rectangular DRA configurations to meet the electrical performance benchmarks outlined in Sections 1.2.1 & 1.2.2, for a typical linear and circular polarization implementation will be theoretically and experimentally investigated.

Probe, aperture, and direct microstrip feeding have been used to excite the rectangular DRA. All three techniques have been used in this investigation in order to observe the effect the different feeds have on the performance of the DRA. The probe feed was used most extensively since it easily matched to most rectangular shapes and was easily modified for tuning purposes.

Three novel modifications to the rectangular DRA were investigated for their potential as compact broad band antennas. The geometries for these antennas are shown in Figure 1.8, without the feed structures. The first structure is called a **multi-segment** DRA, consistent with the terminology of Petosa, which is formed from several segments of dielectric material with different values of permittivity. The **edge-grounded** DRA has one wall of the DR covered with a grounded conductor. The **multi-segment edge-grounded** DRA is the combination the above.

1.6 Thesis Methodology

1.6.1 Experimental Work

The experimental work was the main undertaking of this work. Aperture, probe and direct microstrip coupling were used to excite linearly and circularly polarized rectangular dielectric resonator antennas. Many different shapes and dielectric constants were used, with the focus on determining the requirements necessary to meet the benchmarks of Sections 1.2.1 and 1.2.2. The design expressions and methodology came from the existing published body of work described in Section 1.4.

Three novel modified rectangular dielectric resonator antennas are proposed. Using probe coupling a variety of different shapes and dielectric constants of these DRA were investigated.

1.6.2 Analytic Work

No new theory for the design of regular rectangular dielectric resonator antennas is developed. The accuracy of the existing second order model of the rectangular DRA is verified, along with the circular polarization design methodology.

Simple predictors for the bandwidth and resonant frequency for the modified rectangular DRA are developed. The analysis of the modified DRA is based on the existing theoretical treatment of the regular rectangular DRA. A simple standard for quantifying the change in bandwidth for a modified dielectric resonator antenna that takes into account a shift in resonant frequency is proposed.

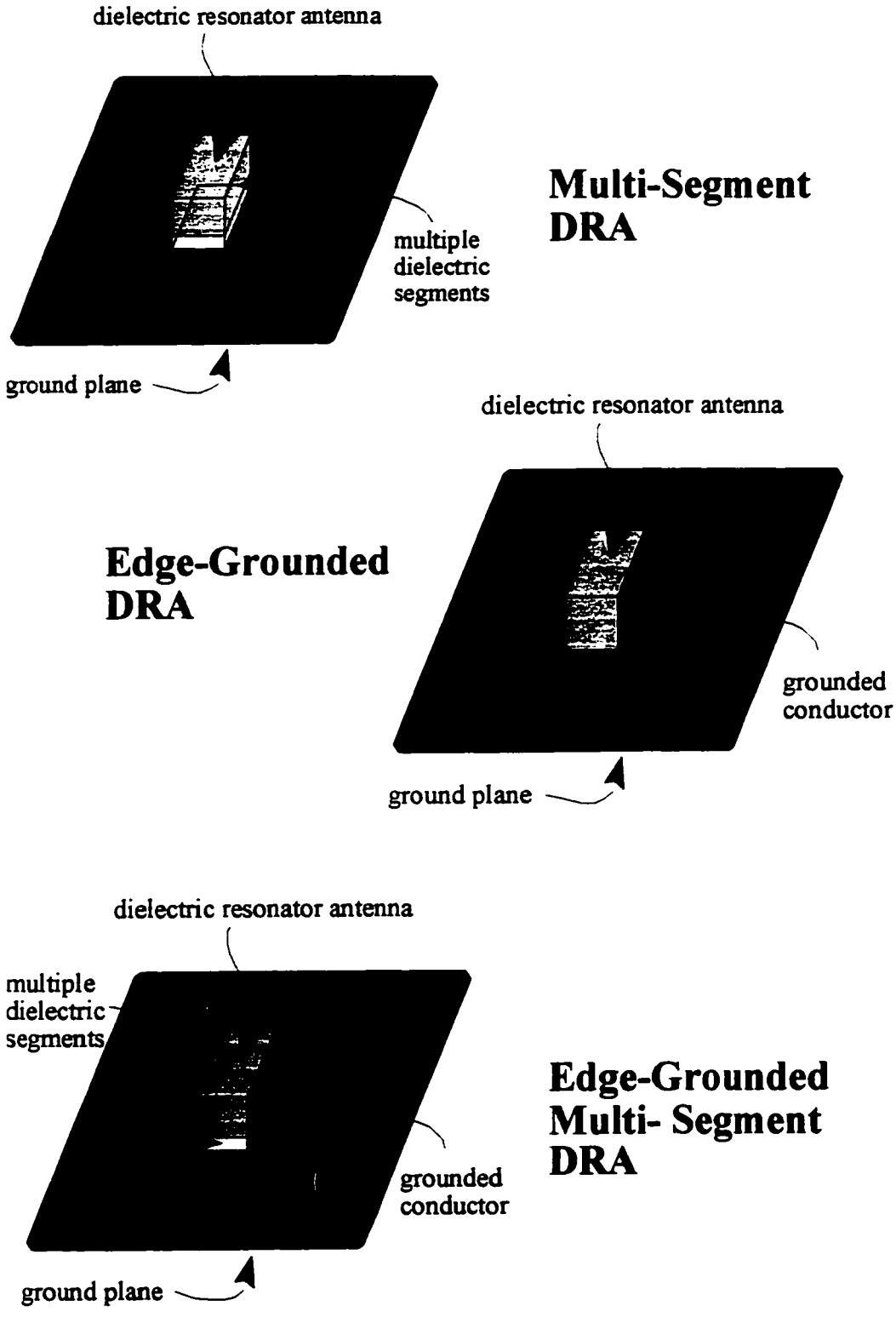

Figure 1.8
Modified and Novel Rectangular Dielectric Resonator Antennas

Chapter 2

Rectangular Dielectric Resonator Antenna Theory

2.1 Introduction

This section outlines the theory of rectangular dielectric resonator antennas used in the design and analysis of the DRA in this work. The model that will be used is that presented by Guillon & Garault [21], which was an integration of the Okaya & Barash [13] concept of mixed magnetic walls for a dielectric resonator with Marcatili's [20] use of a truncated dielectric waveguide with internal fields matched to external fields decaying in the direction away from the resonator. The G&G model is an isotropic dielectric waveguide (DWM) with PMC sidewalls truncated to form the DRA. The truncated walls are modelled using the imperfect magnetic wall (IMW) technique as in Marcatili.

Using this model, exact expressions are formulated for resonant frequency and impedance bandwidth of linearly polarized DRA. The model is independent of the method of excitation of the DRA and an expression for the input impedance of the DRA is not derived. This model was the one used by Mongia [36], Ittipiboon [31], Petosa [47], Loos [50], and Oliver [46].

While higher order modes have been shown to radiate potentially useful patterns,

these modes suffer from inherently lower bandwidths as compared to the lowest order resonant mode of the rectangular DRA. Since achieving a broad bandwidth and compact geometry is an objective, the lowest order resonant mode of the rectangular DRA was investigated.

The field structure of this mode was used in the theoretical calculation of the radiation pattern for the DRA excited in the lowest order. The predictors for resonant frequency and impedance bandwidth were used in the development of a design procedure for a single aperture coupled broad band circularly polarized rectangular DRA. These expressions were also used to model the variation of the bandwidth of the DRA with respect to its geometry.

Only square planform DRA were designed, so that the option of generating dual linear or circular polarization, as well as linear polarization was available. The effects of this choice will be described in Section 2.4.

2.2 Truncated Dielectric Waveguide Model

The rectangular DRA will be modelled as a truncated section of isotropic dielectric waveguide, see Figure 2.1. Solutions have been formulated for the modal structure of a wave propagating in such a waveguide. To derive simple analytic expressions for the field structure in the resonator several simplifying assumptions have been made. Since the DRA will be in general resting on a conducting surface, and thus the equivalent dielectric waveguide would also incorporate the mirror image of the DRA then only field structures which satisfy the requirement of symmetry in the vertical plane will be considered.

No rigorous classification of modes of an isolated rectangular DRA exist [58]. A general classification of the modes of an arbitrarily shaped dielectric resonator of very high permittivity was given by Van Bladel [18]. In it modes which satisfy the first part of

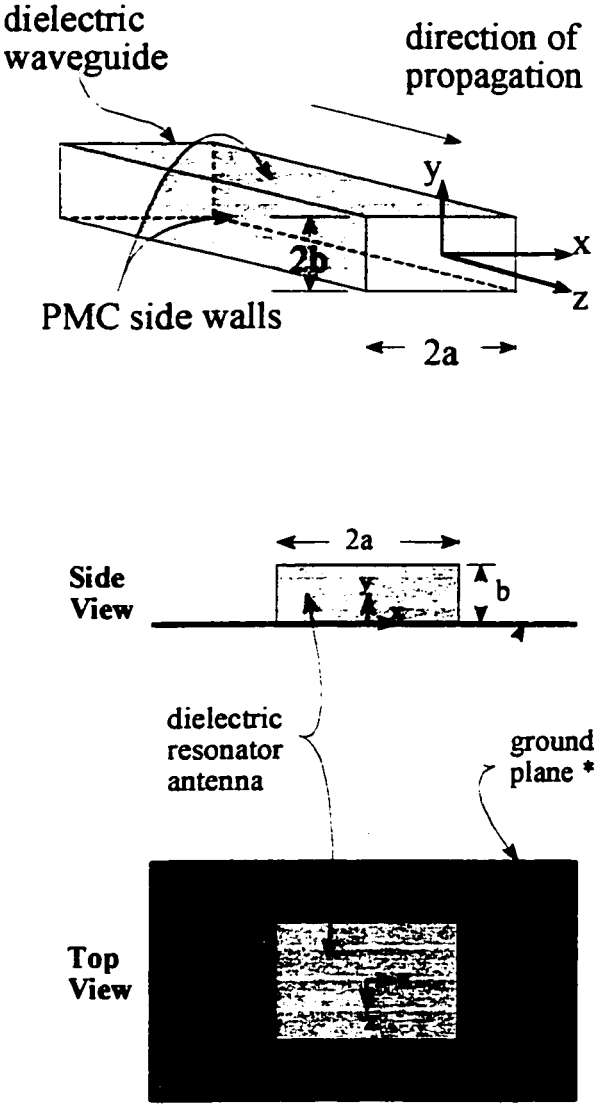

Figure 2.1
Rectangular Dielectric Waveguide and Resonator Geometry

Equation 2.1 for all surfaces of the DRA are considered 'non-confined'. Modes which satisfy all of Equation 2.1, at all walls of the DR, in other words satisfy all conditions for a magnetic wall, are described as 'confined'.

$$\begin{aligned} \boldsymbol{E}\cdot\boldsymbol{n} &= 0 \\ \boldsymbol{n}\times\boldsymbol{H} &= 0 \end{aligned} \tag{2.1}$$

Van Bladel also showed that only bodies of revolution, such as the cylinder and the sphere, can support confined modes, so only the first part of Equation 2.1 is satisfied at all surfaces of the rectangular DRA. Okaya and Barash suggested that the modes of the rectangular DR could be divided into TE and TM types. The TM modes were not experimentally observed, and when analysed using the dielectric waveguide model the fields of the TM modes do not satisfy the first part of Equation 2.1. The TE modes do satisfy the first part of Equation 2.1 and will be the focus of this work.

2.2.1 Resonant Frequency

Following the method of analysis of TE modes in rectangular coordinates given by Balanis [59], inside the dielectric waveguide the electric and magnetic fields must satisfy the homogeneous vector Helmholtz equations :

$$\begin{aligned} \nabla^2\boldsymbol{H} + \epsilon_r k_0^2 \boldsymbol{H} &= 0 \\ \nabla^2\boldsymbol{E} + \epsilon_r k_0^2 \boldsymbol{E} &= 0 \end{aligned} \tag{2.2}$$

In rectangular coordinates, the separation equation is given by :

$$k_x^2 + k_y^2 + k_z^2 = \epsilon_r k_0^2 \tag{2.3}$$

For a Z-directed TE propagating mode in rectangular coordinates the fields can be expressed as :

$$\begin{aligned} E &= E_{xy}(x,y)e^{-jk_z z} \\ H &= H_{xy}(x,y)e^{-jk_z z} + H_z(x,y)e^{-jk_z z} \end{aligned} \tag{2.4}$$

Applying the separated gradient expression :

$$\nabla^2 = \nabla_t^2 - k_z^2 \tag{2.5}$$

to the Helmholtz equation for the magnetic field yields :

$$\begin{aligned} &\nabla_t^2 H_z + k_c^2 H_z = 0 \\ &\text{where} \quad k_c^2 = \epsilon_r k_0^2 - k_z^2 = k_x^2 + k_y^2 \end{aligned} \tag{2.6}$$

The H_z component of the magnetic field can be used as a scalar potential function in the solution of the scalar Helmholtz equation. The general form of the solution for the magnetic field term is :

$$H_z = [A\cos(k_x x) + B\sin(k_y y)][C\cos(k_x x) + D\sin(k_y y)] \tag{2.7}$$

Enforcing the magnetic conductor boundary condition at |x|=a and |y|=b yields the following values for k_x, k_y :

$$\begin{aligned} k_x &= \frac{m\pi}{2a}, \quad m = 1,2,... \\ k_y &= \frac{n\pi}{2b}, \quad n = 1,2,... \end{aligned} \tag{2.8}$$

For the lowest order TE mode, m=n=1, of the homogeneous dielectric waveguide modelled with perfect magnetic walls, the solution of the scalar potential has the form :

$$H_z = A\cos(k_x x)\cos(k_y y) \tag{2.9}$$

As done in Mongia, it is assumed that the fields outside the DRA have a similar variation along the X and Y directions as the fields inside the resonator, but they decay exponentially in the Z-direction (Marcatili's approximation for imperfect magnetic walls). Matching the fields along the surface of the DRA at |z|=d leads to the transcendental equations for the wave number k_z :

$$k_z d = p\pi - \tan^{-1}\left(\frac{k_z}{k_{z0}}\right)$$
$$k_{z0} = \sqrt{(\epsilon_r - 1)k_0^2 - k_z^2} \qquad \textbf{(2.10)}$$

This simple set of equations is the basis for design and analysis of the DRA in this work. For the lowest order mode of p=1, Equation 2.10 can be expressed so as to calculate the dimension d.

$$d = \frac{1}{k_z}\tan^{-1}\left(\frac{k_{z0}}{k_z}\right) \qquad \textbf{(2.11)}$$

And for analysis purposes the separation Equation 2.3 can be expressed to calculate resonant frequency.

$$f_0 = \frac{c}{2\pi\sqrt{\epsilon_r}}\sqrt{k_x^2 + k_y^2 + k_z^2} \qquad \textbf{(2.12)}$$

2.2.2 Field Structure of TE_{111} Mode

The field components of the TE_{111} mode can be found from the scalar potential, H_z, using standard relations for Z-directed TE modes :

$$
\begin{aligned}
\boldsymbol{H}_{xy} &= -\frac{jk_z}{k_c^2}\nabla_t H_z \\
&= -\frac{jk_z}{k_x^2+k_y^2}\left(\frac{\partial}{\partial x}\boldsymbol{a}_x+\frac{\partial}{\partial y}\boldsymbol{a}_y\right)A\cos(k_x x)\cos(k_y y) \\
&= \frac{jAk_xk_z}{k_x^2+k_y^2}\sin(k_x x)\cos(k_y y)\boldsymbol{a}_x+\frac{jAk_yk_z}{k_x^2+k_y^2}\cos(k_x x)\sin(k_y y)\boldsymbol{a}_y
\end{aligned}
\tag{2.13}
$$

$$
\begin{aligned}
\boldsymbol{E}_{xy} &= -\frac{\omega\mu_0}{k_z}\boldsymbol{a}_z\times\boldsymbol{H}_{xy} \\
&= -\frac{\omega\mu_0}{k_z}\left[-\frac{jAk_yk_z}{k_x^2+k_y^2}\cos(k_x x)\sin(k_y y)\boldsymbol{a}_x+\frac{jAk_xk_z}{k_x^2+k_y^2}\sin(k_x x)\cos(k_y y)\boldsymbol{a}_y\right] \\
&= j\omega\mu_0 A\frac{k_y}{k_x^2+k_y^2}\cos(k_x x)\sin(k_y y)\boldsymbol{a}_x-j\omega\mu_0\frac{Ak_x}{k_x^2+k_y^2}\sin(k_x x)\cos(k_y y)\boldsymbol{a}_y
\end{aligned}
\tag{2.14}
$$

When the dielectric waveguide is truncated, an interference pattern between the forward and reverse travelling waves is created. Observing the same notation as in Equation 2.4 for the electric and magnetic field components, the interference field patterns can be expressed as :

$$
\begin{aligned}
\boldsymbol{H}_{resonant} &= \boldsymbol{H}^+ + \boldsymbol{H}^- \\
&= (\boldsymbol{H}_{xy}+\boldsymbol{H}_z)e^{-jk_z z}+(-\boldsymbol{H}_{xy}+\boldsymbol{H}_z)e^{jk_z z} \\
&= \boldsymbol{H}_{xy}(e^{-jk_z z}-e^{jk_z z})+\boldsymbol{H}_z(e^{-jk_z z}+e^{-jk_z z}) \\
&= -j2\sin(k_z z)\boldsymbol{H}_{xy}+2\cos(k_z z)\boldsymbol{H}_z
\end{aligned}
\tag{2.15}
$$

$$
\begin{aligned}
\boldsymbol{E}_{resonant} &= \boldsymbol{E}^+ + \boldsymbol{E}^- \\
&= \boldsymbol{E}_{xy}e^{-jk_z z}+\boldsymbol{E}_{xy}e^{jk_z z} \\
&= 2\cos(k_z z)\boldsymbol{E}_{xy}
\end{aligned}
\tag{2.16}
$$

And the field components for the TE_{111}^{z} mode of the rectangular dielectric resonator are given by :

$$
\begin{aligned}
E_x &= j\omega\mu_0 A \frac{k_y}{k_x^2 + k_y^2} \cos(k_x x)\sin(k_y y)\cos(k_z z) \\
E_y &= -j\omega\mu_0 A \frac{k_x}{k_x^2 + k_y^2} \sin(k_x x)\cos(k_y y)\cos(k_z z) \\
E_z &= 0 \\
H_x &= A \frac{k_x k_z}{k_x^2 + k_y^2} \sin(k_x x)\cos(k_y y)\sin(k_z z) \\
H_y &= A \frac{k_y k_z}{k_x^2 + k_y^2} \cos(k_x x)\sin(k_y y)\sin(k_z z) \\
H_z &= A \cos(k_x x)\cos(k_y y)\cos(k_z z)
\end{aligned}
\qquad \textbf{(2.17)}
$$

Following the nomenclature of rectangular dielectric waveguides used by Marcatili, equations 2.17 describe the TE_{111}^{z} mode where the electric field is transverse to the Z-axis. For a DRA in free space there are three such modes; TE_{111}^{x}, TE_{111}^{y}, and TE_{111}^{z}.

On a ground plane, located at y=0, only the TE_{111}^{x} and TE_{111}^{z} are present since they satisfy the boundary conditions for a PEC in that plane and the TE_{111}^{y} mode does not. The PEC boundary conditions are :

$$
\begin{aligned}
\boldsymbol{H}\cdot\boldsymbol{n} &= 0 \\
\boldsymbol{n}\times\boldsymbol{E} &= 0
\end{aligned}
\qquad \textbf{(2.18)}
$$

And in the plane y=0, the TE_{111}^{z} mode is given by :

$$
\begin{aligned}
E_x &= 0 \qquad E_y = f(x,z) \qquad E_z = 0 \\
H_x &= g(x,z) \qquad H_y = 0 \qquad H_z = k(x,z)
\end{aligned}
\qquad \textbf{(2.19)}
$$

which evidently satisfies the PEC boundary conditions for $\mathbf{n} = \mathbf{a}_y$. The fields of the TE_{111}^{y}

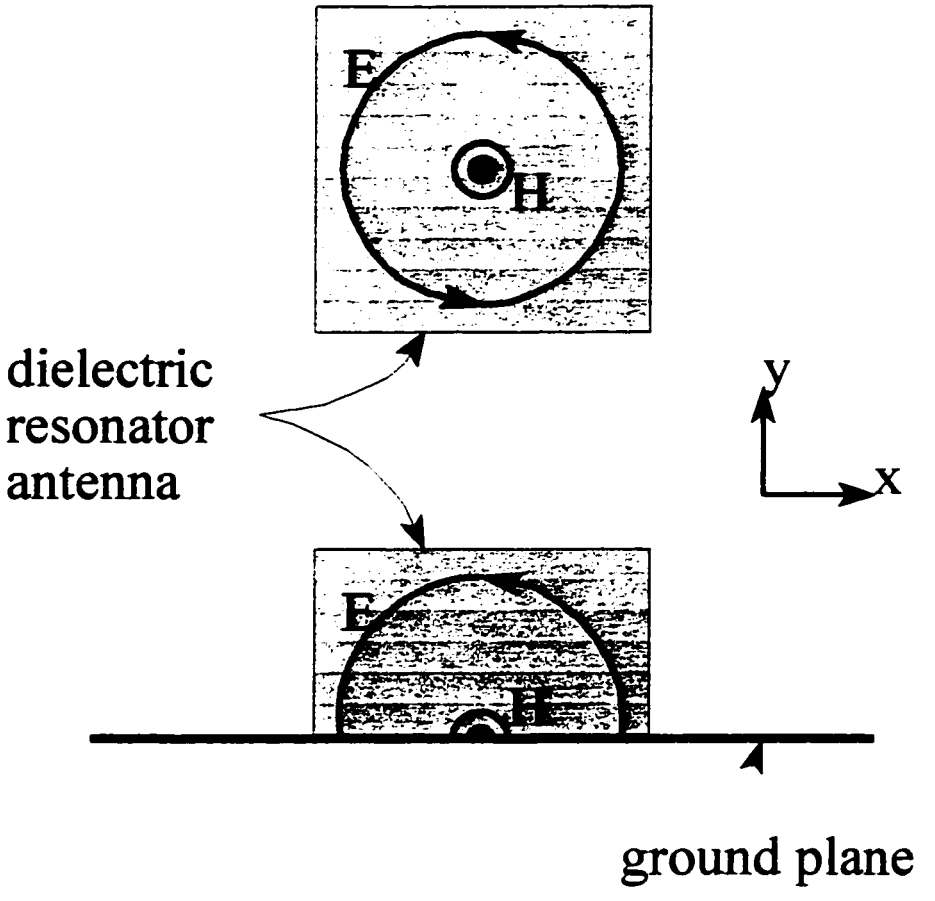

Figure 2.2
Orientation of Transverse E-field for Lowest Order Mode of Isolated Rectangular DR and DR on Ground Plane.

mode will obviously not satisfy the boundary conditions.

2.2.3 Impedance Bandwidth

Using the expressions for the internal field structure of the DRA an analytic expression for the bandwidth of the antenna will be developed, as presented by Mongia [58]. Equation 2.20 relates the calculated radiation Q-factor of the DRA to the observed bandwidth for a specific SWR (S).

$$BW = \frac{S-1}{\sqrt{S}Q_{rad}} \tag{2.20}$$

A number of assumptions are made. First, Equation 2.20 assumes the equivalent circuit of an antenna can be represented by a RLC shunt resonator across a lossless transmission line. In practice, the self reactance of the feed will effect both the resonant frequency and bandwidth of the DRA [50] as will be seen when different feed excitation schemes are used on identical DRA. Second, for all work to follow, impedance bandwidth will refer to a SWR of 2:1 for the matched antenna, which results in Equation 2.21.

$$BW = \frac{1}{\sqrt{2}Q_{rad}} \tag{2.21}$$

For a SWR of 1.5, Equation 2.20 yields BW = $0.41/Q_{rad}$. For the PCS 1.9 Benchmark of a bandwidth of 7.3% for a SWR of 1.5, the equivalent bandwidth for a SWR of 2:1 is given by :

$$BW_{PCS} = \frac{BW_2}{BW_{1.5}} \cdot 7.3\% = 12.6\% \tag{2.22}$$

The Q-factor of a shielded dielectric resonator is typically defined as $1/\tan\delta$. For low loss dielectric materials the dielectric loss is a very small fraction compared to the radiative loss for unshielded DR and thus the unloaded Q-factor can be approximated solely by the radiation Q-factor of the antenna which is given by the standard relation :

$$Q_{rad} = \frac{2\omega_0 W_e}{P_{rad}} \tag{2.23}$$

The isolated dielectric resonator occupies the space defined by :

$$\begin{aligned} -a < x < a \\ -b < y < b \\ -d < z < d \end{aligned} \tag{2.24}$$

Van Bladel [18] showed that a homogeneous dielectric body radiates like an equivalent volume electric polarization current source of density $\mathbf{J_P}$:

$$\begin{aligned} \boldsymbol{J}_p &= j\omega\epsilon_0(\epsilon_r - 1)\boldsymbol{E} \\ &= j\omega\epsilon_0(\epsilon_r - 1)[E_x\boldsymbol{a}_x + E_y\boldsymbol{a}_y] \end{aligned} \tag{2.25}$$

It has been shown that the lowest order dielectric resonator antenna mode radiates like a magnetic dipole, so it is possible to find the magnetic dipole moment of an isolated rectangular dielectric resonator :

$$\begin{aligned} \boldsymbol{p}_m &= \tfrac{1}{2}\int \boldsymbol{R}\times\boldsymbol{J}_p\,dV \\ &= \tfrac{1}{2}\int (x\boldsymbol{a}_x + y\boldsymbol{a}_y + z\boldsymbol{a}_z) \times j\omega\epsilon_0(\epsilon_r - 1)[E_x\boldsymbol{a}_x + E_y\boldsymbol{a}_y]\,dV \\ &= \frac{j\omega\epsilon_0(\epsilon_r - 1)}{2}\int -zE_y\boldsymbol{a}_x + zE_x\boldsymbol{a}_y + [xE_y - yE_x]\boldsymbol{a}_z\,dV \\ &= \frac{-\omega^2\mu_0\epsilon_0(\epsilon_r - 1)A}{2(k_x^2 + k_y^2)}\iiint zk_x\sin(k_x x)\cos(k_y y)\cos(k_z z)\boldsymbol{a}_x \\ &\qquad + zk_y\cos(k_x x)\sin(k_y y)\cos(k_z z)\boldsymbol{a}_y \\ &\qquad - xk_x\sin(k_x x)\cos(k_y y)\cos(k_z z) \\ &\qquad - yk_y\cos(k_x x)\sin(k_y y)\cos(k_z z)\boldsymbol{a}_z\,dxdydz \end{aligned} \tag{2.26}$$

Since,

$$\begin{aligned} \int_{-a}^{a} \sin(\tfrac{\pi x}{2a})dx &= 0, \qquad p_{m_x} = 0 \\ \int_{-b}^{b} \sin(\tfrac{\pi y}{2b})dy &= 0, \qquad p_{m_y} = 0 \end{aligned} \tag{2.27}$$

Then,

$$p_m = \frac{-\omega^2 \mu_0 \epsilon_0 (\epsilon_r - 1)A}{2(k_x^2 + k_y^2)} \iiint -x k_x \sin(k_x x)\cos(k_y y)\cos(k_z z) - y k_y \cos(k_x x)\sin(k_y y)\cos(k_z z)\, a_z \, dxdydz \tag{2.28}$$

$$p_m = \frac{\omega^2 \mu_0 \epsilon_0 (\epsilon_r - 1)A}{2(k_x^2 + k_y^2)} [\frac{16\sin(k_z d)}{k_x k_y k_z}]\, a_z$$

Due to the high dielectric constant of the DRA, as compared to the surrounding medium, most of the stored energy is contained inside the DRA. From the expression for the field structure of the TE_{111} mode determined in Section 2.2.2, when the stored energy in the electric field is at a maximum, the stored energy in the isolated DRA can be calculated as :

$$\begin{aligned} W_e &= \frac{1}{2}\int \epsilon E \cdot E^* dV \\ &= \frac{\epsilon_0 \epsilon_r}{2}\int E_x^2 + E_y^2 dV \\ &= \frac{\epsilon_0 \epsilon_r}{2}\frac{\omega^2 \mu_0^2 A^2}{(k_x^2 + k_y^2)^2}\iiint k_y^2 \cos^2(k_x x)\sin^2(k_y y)\cos^2(k_z z) + k_x^2 \sin^2(k_x x)\cos^2(k_y y)\cos^2(k_z z)\, dxdydz \end{aligned} \tag{2.29}$$

$$= \frac{\epsilon_0 \epsilon_r}{2}\frac{\omega^2 \mu_0^2 A^2}{(k_x^2 + k_y^2)^2}\, [abk_y^2(\frac{\sin(2k_z d)}{2k_z} + d)] + [abk_x^2(\frac{\sin(2k_z d)}{2k_z} + d)]$$

$$W_e = \frac{\epsilon_0 \epsilon_r}{2}\frac{\omega^2 \mu_0^2 A^2}{(k_x^2 + k_y^2)^2}\, [abd(\frac{\sin(2k_z d)}{2k_z d} + 1)(k_x^2 + k_y^2)]$$

And a simple analytic expression for the bandwidth of a rectangular DRA excited in the TE_{111}^{Z} mode can be calculated :

$$
\begin{aligned}
BW &= \frac{P_{rad}}{2\sqrt{2}\omega W_e} \\
&= \frac{10k_0^4|p_m|^2}{2\sqrt{2}\omega W_e} \\
&= \frac{10k_0^4\left(\frac{\omega^2\mu_0\epsilon_0(\epsilon_r-1)A}{2(k_x^2+k_y^2)}\left[\frac{16\sin(k_z d)}{k_x k_y k_z}\right]\right)^2}{2\sqrt{2}\omega\frac{\epsilon_0\epsilon_r}{2}\frac{\omega^2\mu_0^2A^2}{(k_x^2+k_y^2)^2}\left[abd\left(\frac{\sin(2k_z d)}{2k_z d}+1\right)(k_x^2+k_y^2)\right]} \\
BW &= \frac{320k_0^4\omega\epsilon_0(\epsilon_r-1)^2\sin^2(k_z d)}{\sqrt{2}\epsilon_r(abd)k_x^2k_y^2k_z^2(k_x^2+k_y^2)\left(\frac{\sin(2k_z d)}{2k_z d}+1\right)}
\end{aligned}
\tag{2.30}
$$

2.3 Circular Polarization

Circular polarized radiation from a linear radiator such as the rectangular DRA is achieved by the generation in the far field of two linearly polarized waves equal in magnitude, orthogonal in space and orthogonal in phase [60]. The interference pattern for these waves creates a wave with a rotating polarization vector. Axial ratio, a ratio of the maximum to minimum magnitude of the rotating polarization vector is a commonly used measure of the quality of circular polarization that is generated. In terms of generating broadband circular polarization from the single aperture fed DRA, the limiting factor is typically the magnitude of the axial ratio [44]. For the methods which generate the phase quadrature condition in an external circuit and then individually excite the orthogonal modes, a broad band axial ratio performance is more easily maintained.

A number of methods of generating circular polarization from DRA have been

demonstrated. These methods include exciting the degenerate modes of a square, cylindrical or annular DRA in phase quadrature [44] or exciting a rectangular [46], Figure 2.4, or cross shaped DRA [45], Figure 2.5, with a single aperture to radiate circular polarization. The results published by Oliver for a single aperture fed rectangular DRA showed broad band performance similar to the MSAT benchmark [46]. Since aperture coupling is compact and requires a less complex feed circuit, this method was selected for experimental investigation. The theoretical treatment will focus on the design methodology for the single aperture fed rectangular DRA. The same technique is also applicable to the cruciform shape.

Exciting the spatially orthogonal TE_{111}^{Z} and TE_{111}^{X} modes of square planform DRA (planform refers to the horizontal or XZ plane) in phase quadrature generates circular polarization at boresight from the ground plane. In [46], Oliver demonstrated that it was possible to generate circular polarization using a single aperture feeding a non-square resonator. The orthogonal TE_{111}^{Z} and TE_{111}^{X} modes can be designed such that at the desired resonant frequency they are excited 90 degrees out of phase.

Assuming the DRA to behave like a simple RLC resonator, the 3dB frequency points of the linear resonance are 45 degrees out of phase with the Q-point or resonant frequency. To achieve the 90 degrees phase shift between the linear resonances of the DRA, dimensions are selected such that the frequency of the lower 3dB point of one resonant mode lines up with the frequency of the upper 3dB point of the other linear resonant mode, Figure 1.3. This technique can be applied to the TE_{111}^{Z} and TE_{111}^{X} modes of a rectangular resonator, or on to the lowest order modes in each arm of a cruciform resonator :

$$f_1 + \frac{\Delta f_1}{2} = f_2 - \frac{\Delta f_2}{2} \qquad \textbf{(2.31)}$$

Frequencies f_1 and f_2 are the resonant frequencies of the linearly polarized modes, and Δf_1

and Δf_2 are the 3dB bandwidths. Oliver [62] showed for a DRA that can be modelled as a shunt RLC resonator, where the real part of the antenna impedance is matched to the transmission line, the loaded Q-factor of the DRA is half the value of radiation Q-factor. Since the loaded Q-factor defines the relative 3dB bandwidth of the resonator :

$$BW_{3dB} = \frac{1}{Q_L} = \frac{2}{Q_R} \tag{2.32}$$

These two equations are combined to form an error function, e_{cp}. For the design of a CP DRA the error function represents frequency difference between the 3dB frequency points of the linearly polarized spatially orthogonal modes :

$$e_{cp} = (\frac{f_2}{Q_{r2}} + \frac{f_1}{Q_{r1}}) - (f_2 - f_1) \tag{2.33}$$

The bandwidth of this structure does not have the same simple analytic solution as did the linear polarization mode. The radiation properties, namely axial ratio, of the circularly polarized DRA are equally or more important than the impedance bandwidth for this antenna. For frequencies away from optimum for circular polarization the phase difference between the orthogonal polarizations decreases and one linear mode will be excited more strongly than the other. As a rough guide on the expected bandwidth of this structure it is reasonable to put the upper limit at the impedance bandwidth of the linear mode with the narrower bandwidth.

The design process for the cross shaped circularly polarized DRA is identical to that described for the rectangular DRA. Conceptually the cross shaped DRA is formed from the superposition of two rectangular DRA. The lowest order TE_{111} mode for each of the rectangular DRA is designed such that the resonant frequencies are 90 degrees out of phase.

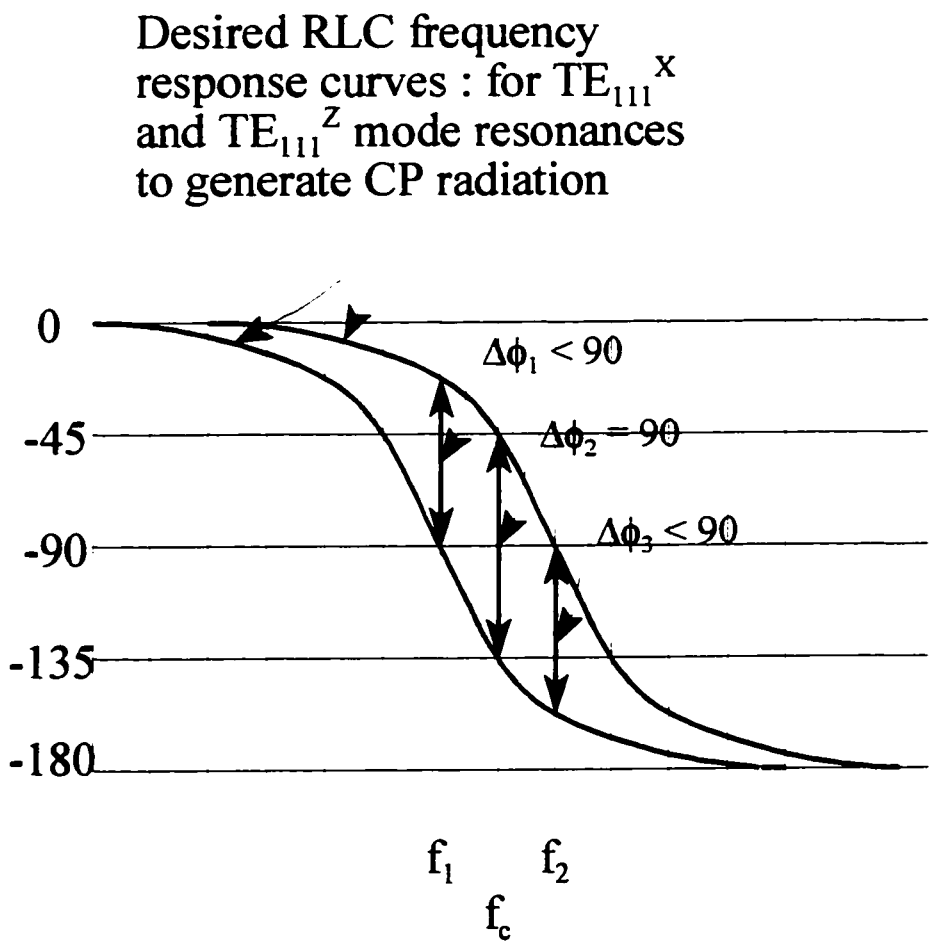

Figure 2.3
Phase Design for Single Feed Rectangular DRA

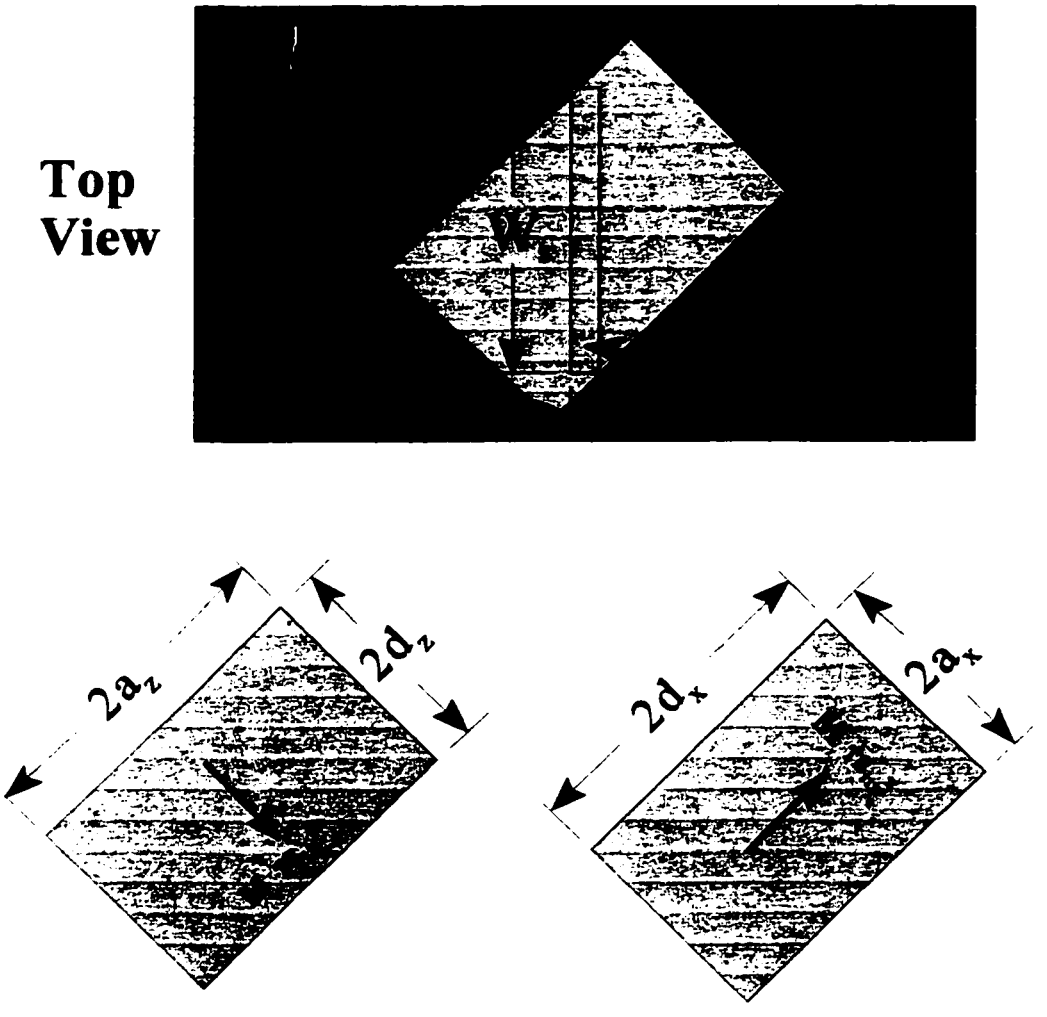

Figure 2.4
Orientation of Single Slot Fed Rectangular DRA, With Linear Modes Illustrated

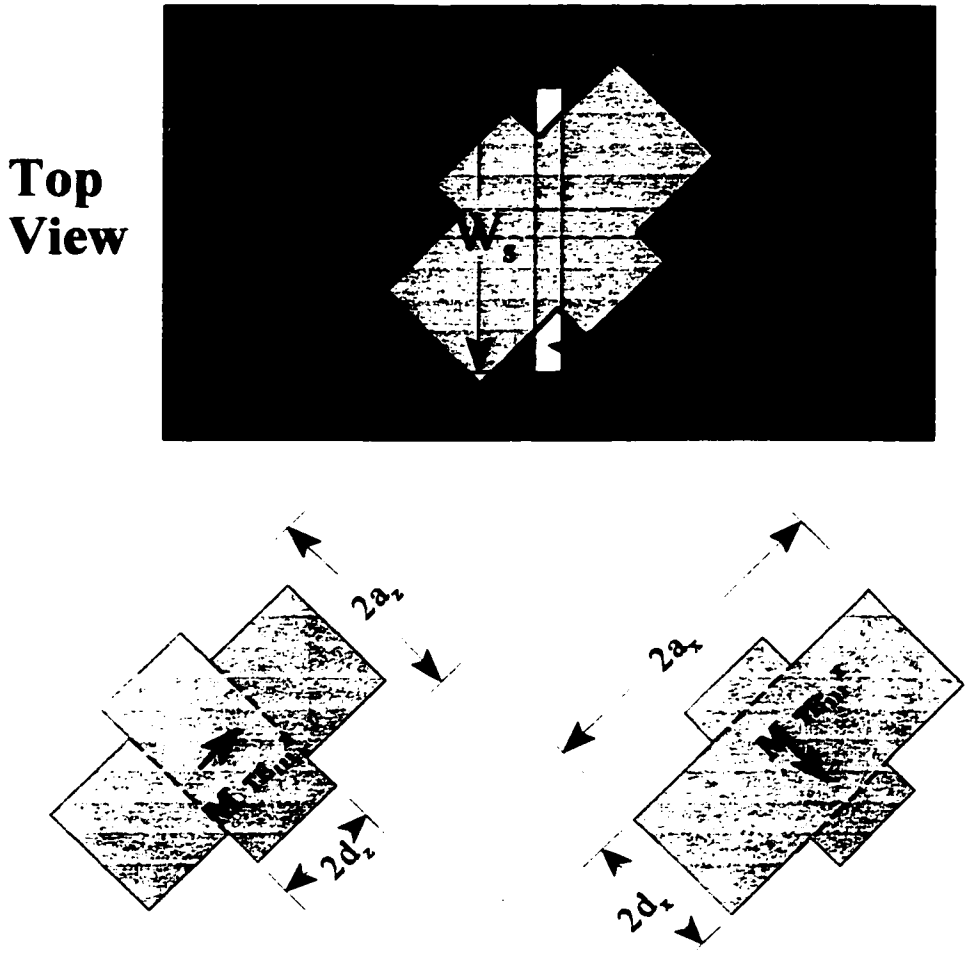

Figure 2.5
Orientation of Single Slot Fed Cruciform DRA, With Linear Modes Illustrated

2.4 Radiation Pattern

To a first order the radiation pattern of the $TE_{111}{}^{Z}$ mode of a compact DRA is that of a short Z-directed horizontal magnetic dipole over a ground plane. Loos [50] outlined several methods for calculating the radiation pattern of the dielectric resonator antenna from a knowledge of the internal fields. One method took advantage of the concept that as formulated by Van Bladel homogeneous dielectric bodies radiate like a volume polarization current. The radiation pattern at each point of interest in the far-field can be determined by summing the contributions of each piece of volume current. The field structure inside the DRA is assumed to be that of the dominant $TE_{111}{}^{Z}$ mode as expressed in Equation 2.17. The relation between the electric field inside resonator and the equivalent volume polarization current [19] is given by :

$$\boldsymbol{J}_p = j\omega\epsilon_0(\epsilon_r - 1)\boldsymbol{E} \tag{2.34}$$

The scattered field from the antenna, developed in [63] can then be found from the current term in :

$$\begin{aligned} \boldsymbol{E}^S &= -j\omega\boldsymbol{A} - \nabla\boldsymbol{F} \\ &= \frac{-j\omega\mu_0}{4\pi}\iiint \boldsymbol{J}\frac{e^{-jk_0R}}{R}dV - \frac{\nabla}{4\pi\epsilon_0}\iiint \rho\frac{e^{-jk_0R}}{R}dV \\ &\approx \frac{-j\omega\mu_0}{4\pi}\iiint \boldsymbol{J}\frac{e^{-jk_0R}}{R}dV \end{aligned} \tag{2.35}$$

The discrete charge term is ignored, as it was shown to have little effect on the resulting pattern. Loos found that this technique predicted patterns that agreed with the wide beamwidth radiation patterns observed through measurement.

2.5 DRA Geometry - Bandwidth Effect

In general, increasing values of dielectric constant correspond to more compact but narrow bandwidth DRA. However, the shape of the DRA, Figure 2.6, also plays a significant role in determining the bandwidth of the antenna [58]. Using the expression for the bandwidth of the TE_{111} mode from Equation 2.30, design curves presented in Figures 2.7-2.10 were generated in order to investigate the effect of DRA geometry on the impedance bandwidth.

In Figure 2.7, the parameter of height (b) is varied while the square planform (2a = 2d) of the DRA is maintained. The calculated bandwidth is plotted versus the normalized width of the DRA, for values of dielectric constant ranging from 10 to 100. The square planform was selected to isolate the effect on the bandwidth to variation of one dimension of the DRA. The normalized width of the DRA was plotted so the minimum dimensions for a desired bandwidth are easy to read from the graph. The height (b) of the DRA varies inversely as the width (2a), so the larger widths would have relatively lower profiles for a particular dielectric constant. It is evident from the expressions for the fields of the $TE_{111}{}^{z}$ mode of Equation 2.17 the Y and X dimensions are interchangeable. The only difference between them is the chosen convention for this report of locating the ground plane at y=0. Thus the results of Figure 2.7, are identical for varying the width (a) and plotting bandwidth results versus normalized height. In that case, the relationship between the height and the transverse dimension is forced to remain constant (b=d).

In Figure 2.7, the minimum bandwidth corresponds to a cubic shape (a=b=d). The location of the minima vary depending on the dielectric constant because the width dimension is normalized to the resonant frequency, and larger values of dielectric constant result in more compact geometries. The cubic shape has the narrowest bandwidth. As the height (width varies inversely with height) of the DRA is decreased, or increased, from the

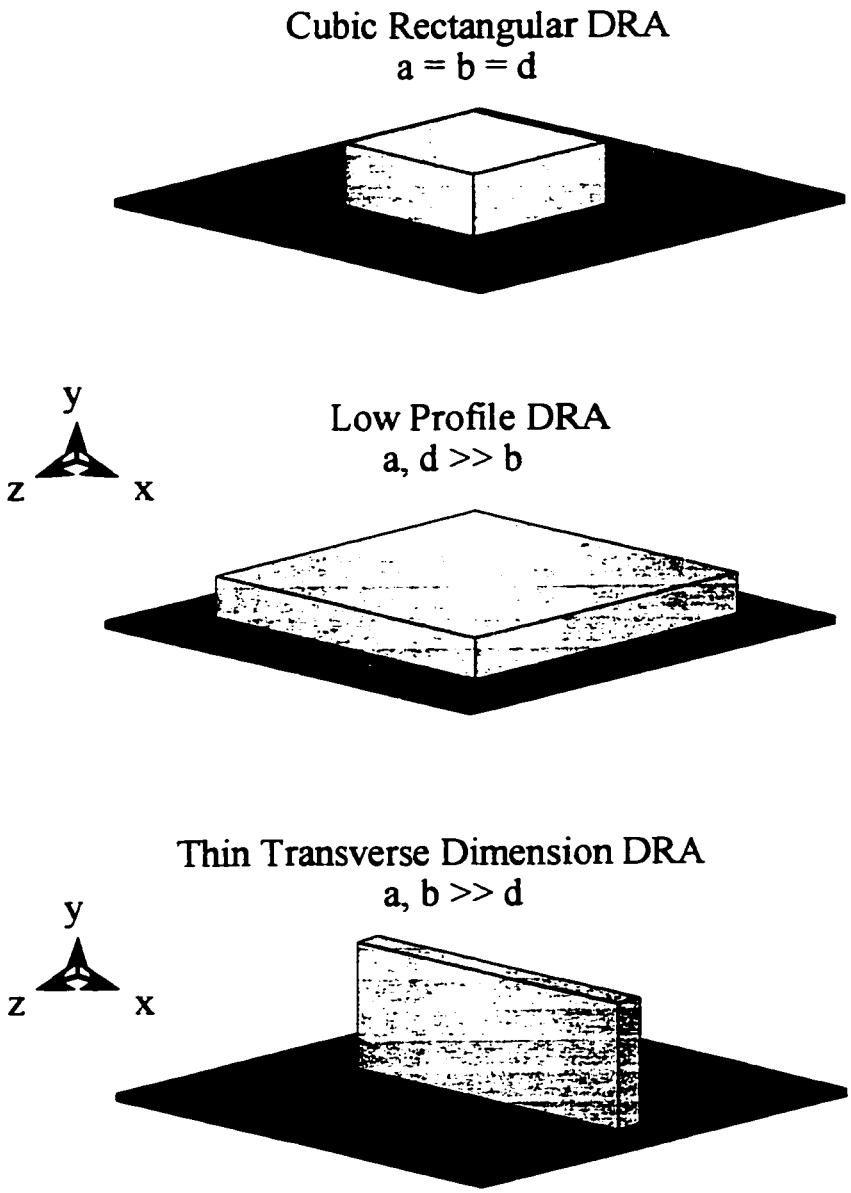

Figure 2.6
Cubic, Low Profile and Thin Transverse Dimension DRA Shapes

cubic shape dimension the bandwidth of the DRA is increased. Figure 2.7 shows the bandwidth can be increased up to 6 times over that of the cubic DRA by proper selection of geometry. This effect was demonstrated in [40] where a broad bandwidth of over 3% was recorded for a low profile rectangular DRA with a dielectric constant of 100.

It is evident that large improvements in bandwidth can be achieved by proper selection of aspect ratio, Figure 2.8. However, for broad band low profile DRA there are limitations on the practical implementation of some geometries. The planform of the DRA element is desirable to be as small as possible for the array implementations of Sections 1.2.1 & 1.2.2. To minimize the potential level of mutual coupling between elements a gap of $\lambda_0/4$ between the edges of adjacent DRA elements is chosen, based on the work in [50]. For the PCS 1.9 benchmark the maximum square DRA dimension becomes $\lambda_0/2$ and for the MSAT benchmark becomes $\lambda_0/4$. Figure 2.9 shows the limitations on bandwidth as a function of dielectric constant for a square planform DRA limited by $\lambda_0/4$ and $\lambda_0/2$. It can be seen that the bandwidth specifications for the two applications are theoretically possible given these dimensional constraints.

While all the DRA used in this investigation had square planforms (except the CP elements), so they could be used as dual linearly or circularly polarized antennas, there is another geometry that should be considered when investigating the bandwidth of the DRA. If only linear polarization is desired then the transverse dimension (d) may be varied independently of the width (a). Figure 2.10 compares the theoretical bandwidth for the square planform geometry where the height is variable against the bandwidth effect of varying the transverse dimension and maintaining the relationship a=b. It is evident from the plot that a broader bandwidth is achieved for thin transverse dimensions. For the same value of bandwidth a 20% reduction in width is possible, however the height is increased. Figure 2.6 conceptually shows the best and worst geometries of DRA in terms of bandwidth performance.

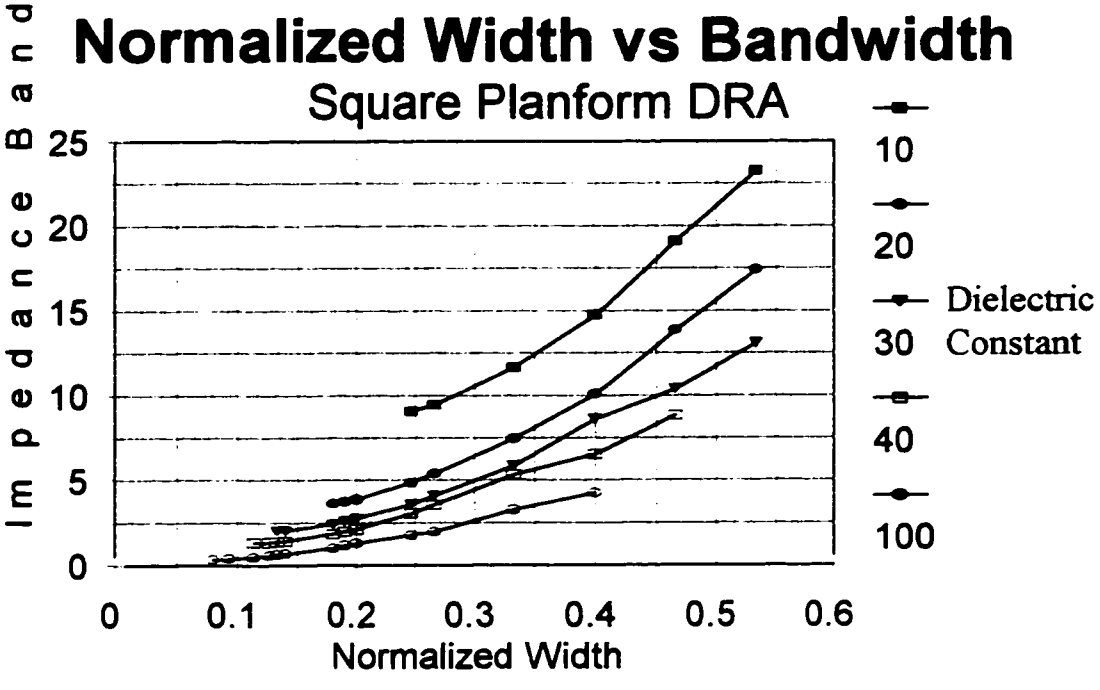

Normalized width = a/λ_0
Square Planform : a = d

Figure 2.7
Plot of Bandwidth vs Normalized Width for ε_r=10 to 100

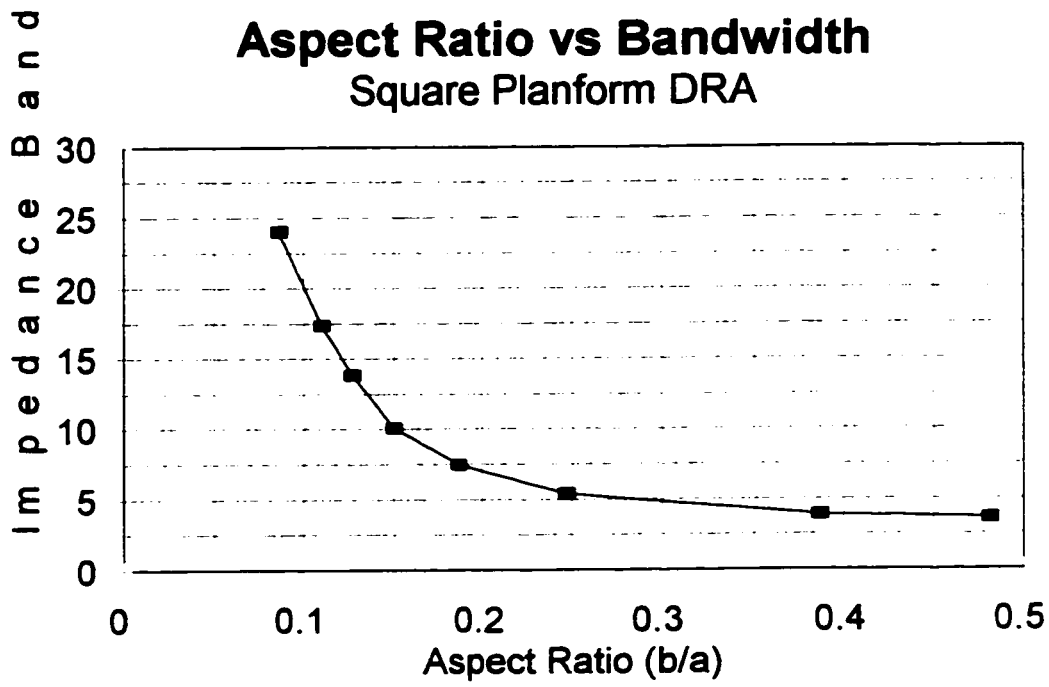

Figure 2.8
Plot of Bandwidth vs Aspect Ratio for ε_r=20

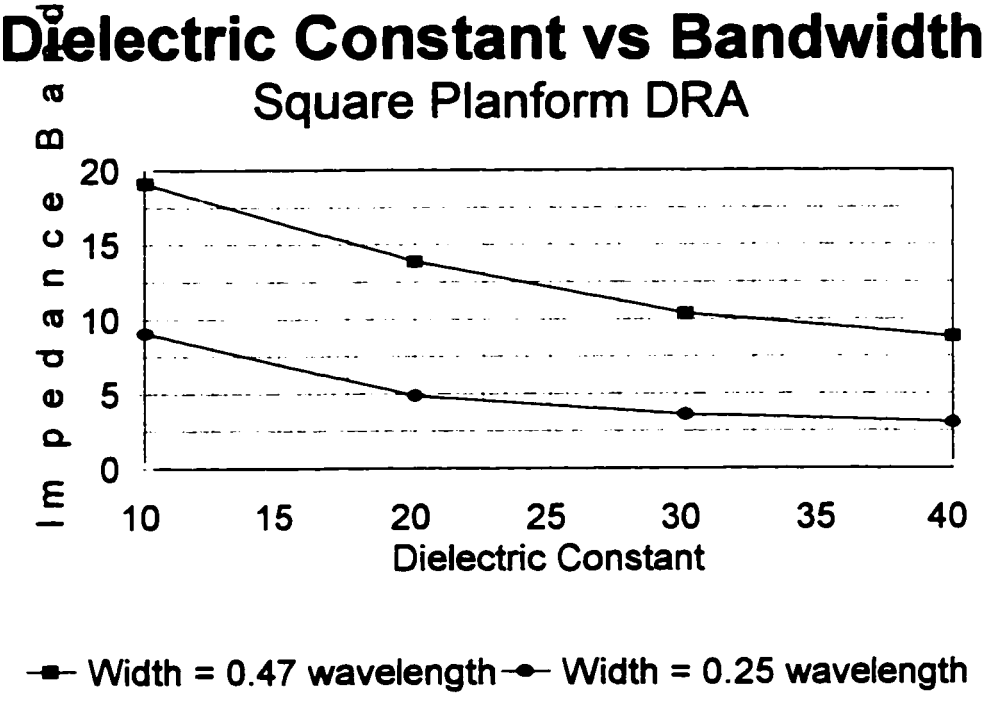

Figure 2.9
Plot of Bandwidth vs Dielectric Constant for Fixed Width

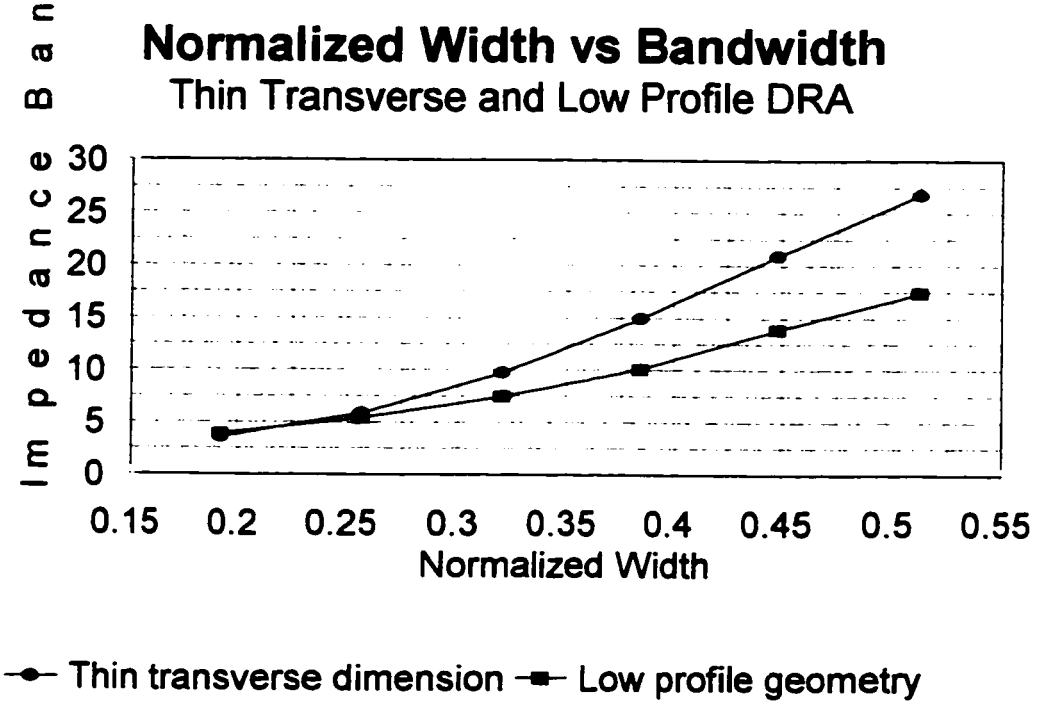

Normalized width = a/λ_0
For thin transverse geometry : a = b
For low profile geometry : a = d

Figure 2.10
Plot of Normalized Width vs Bandwidth for Thin Transverse and Low Profile DRA Geometries of Figure 2.6

2.6 Triangular Dielectric Resonator Antenna

An example of the benefit of using a simple conceptual model of the rectangular DRA is the ease with which it can be extended to similar shapes. Ittipiboon [31] reported on a DRA with a triangular cross section excited by a slot feed, Figure 2.11. A wide impedance bandwidth and broad beamwidth radiation pattern similar to that of the rectangular DRA excited in the TE_{111}^{Z} mode was observed. The DWM with IMW described in Section 2.2 for the rectangular DRA in free space predicts the resonance of the triangular cross section element.

The triangular DRA is equivalent to a square cross section DRA in free space, Figure 2.12, when the width (w) has a value of twice the height (h). The wave numbers k_x and k_y are equal for the square cross section DRA. As a result the fields of the square DRA excited in the TE_{111}^{Z} mode evaluated in the plane x=y are given by :

$$\begin{aligned} E_x &= K_1 \\ E_y &= -K_1 \\ E_z &= 0 \\ H_x &= K_2 \\ H_y &= K_2 \\ H_z &= A\cos(k_x x)\cos(k_y y)\cos(k_z z) \end{aligned} \tag{2.36}$$

By inspection it can be seen that the resultant electric field is perpendicular to the plane x=y and the magnetic field is in the plane x=y, which satisfies the conditions for a PEC located in this plane. Since the physical DRA and the resonant field structure is symmetrical about the plane x=y, then by the same reasoning applied to the rectangular DRA on a ground plane, the triangular cross section DRA on a ground plane is analogous to the square cross section DRA in free space. From the dimensions in Figure 2.11, Equations 2.12 and 2.30 may be used to calculate resonant frequency and impedance bandwidth for the triangular resonator. In Table 2.1, the measured resonant frequency and

bandwidth reported in [31] are compared with the values calculated using this method.

Theoretical		Measured		Resonant Frequency Prediction Error	Ratio of Calculated to Measured Bandwidth
f_r (GHz)	BW (%)	f_r (GHz)	BW (%)		
9.0	10.0	8.53	11.7	5.5 %	0.85

Table 2.1 Comparison Triangular DRA Design Theory With Reported Measurement

The calculated values for resonant frequency and impedance bandwidth agree with the measured values to within the typical accuracies for rectangular DRA for this model as shown in Section 3.3.2. Obviously this one sample is not enough to validate the DWM with IMW, the comprehensive experimental validation will be shown in Chapter 3. This demonstration of the application of the model simply shows the ease with which this model can be extended to DRA shapes with similar boundaries. The triangular DRA has a larger footprint on the ground plane that the equivalent rectangular DRA, however the sloped sidewalls may reduce the mutual coupling between elements [50], allowing for closer spacing in array configurations.

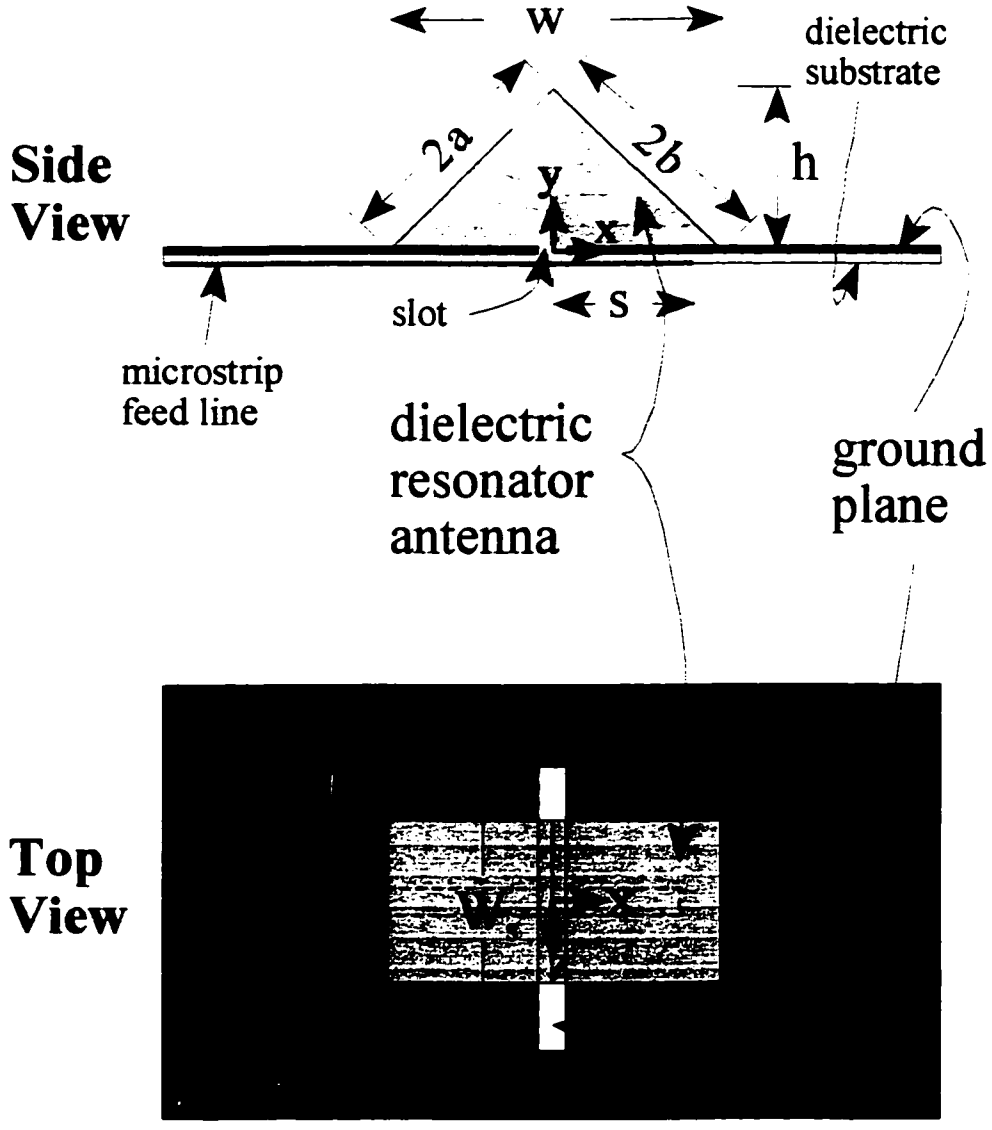

Figure 2.11
Dimensions of Triangular Dielectric Resonator and Slot Feed Circuit

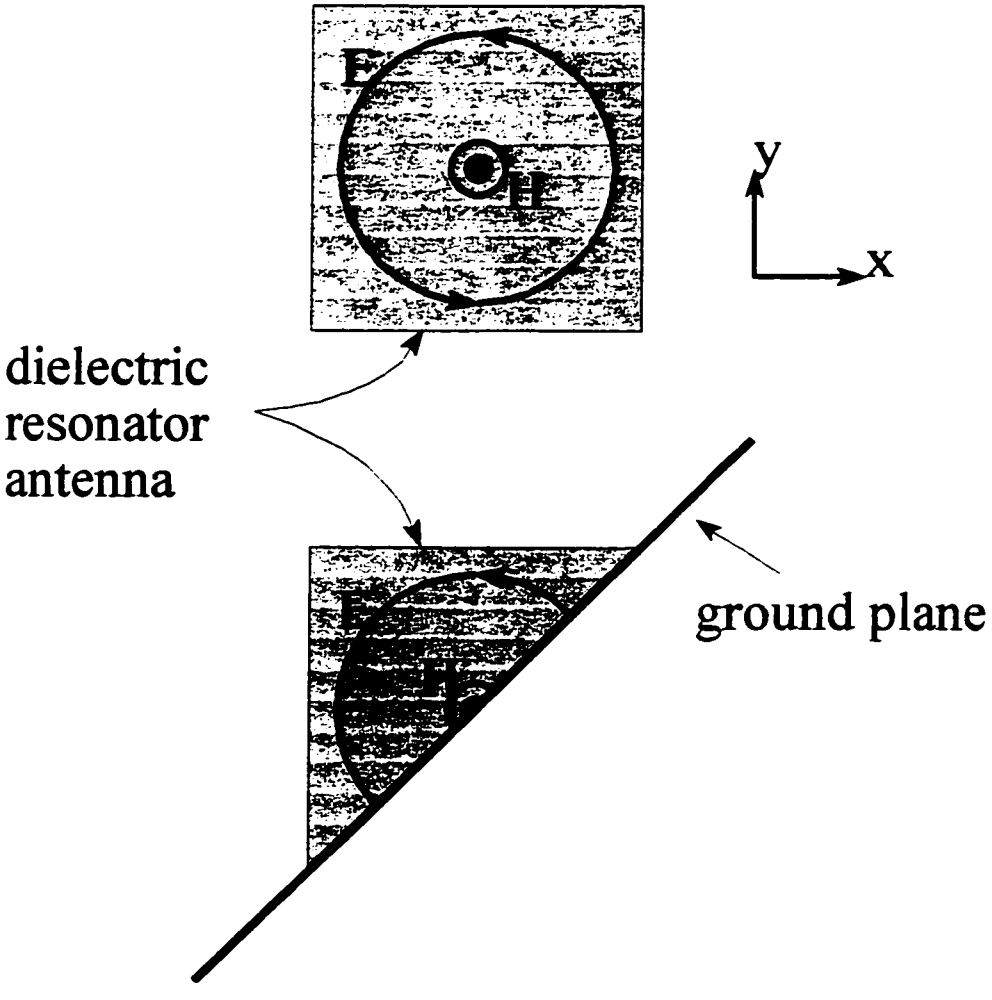

Figure 2.12
Orientation of Transverse E-field for Lowest Order Mode of Rectangular DRA

Chapter 3

Experimental Results

3.1 Introduction

The design expressions and methodology developed in Chapter 2 for rectangular DRA were used to design DRA of a range of dielectric constants and dimensional parameters. Many linearly, dual linearly and circularly polarized DRA were fabricated and their electrical parameters, resonant frequency, impedance bandwidth, radiation pattern, port to port isolation and axial ratio, were measured.

For linearly polarized DRA the PCS 1.9 benchmark used for evaluation had the requirements of a relative bandwidth of 12.6% (nominal centre frequency of 1.9 GHz), and cross polarization levels better than -15dB. The requirements for dual linearly polarized elements were the same as for linear DRA with the additional requirement of an isolation of at least 30dB between the two ports.

For circularly polarized DRA the objective was to determine the dimensional and material parameters of an element suitable for use in a planar array of an MSAT terminal. The MSAT benchmark was a relative bandwidth of 8.5% (nominal centre frequency of 1.6

GHz), and a wide beam width radiation pattern of greater than 100 degrees. The full MSAT array would also have quality of circular polarization requirements for axial ratio, cross polarization and system requirements of gain or G/T. These antenna parameters depend to a large extent on the specific array implementation. An arbitrary specification for the single circularly polarized DRA was selected to be a maximum axial ratio of 3dB and no requirement was specified for the cross polarization measurement since all pattern measurements were only magnitude, performed with a rotating linear source.

The design equations and methods used in the work reported in this chapter are not novel. Most of the experimental work performed for this section had previously been performed on DRAs of similar shape at other frequencies by other researches and reported in the literature. This experimental work was intended to examine the accuracy of the design expressions for rectangular DRA, to verify the results achieved by referenced works, and to determine the potential applicability of the rectangular DRA to the specified L-Band applications.

Table 3.1 lists the dimensions and dielectric constants of the DRA used in the experimental work for this report. The DRA were fabricated from MCT, Stycast HiK500, and Stycast HiHiK, whatever material was available in the lab. The dimensions of the fabricated DRA were limited by the available materials and so some dimensions were not able to be tested, specifically the shapes with large widths (ie $2a = \lambda_0/2$).

DRA	Dielectric Constant	Height (b) (cm)	Width (2a) (cm)	Transverse (2d) (cm)	Resonant Frequency (GHz)	Impedance Bandwidth (%)
D10L1	10	2.54	5.2	5.2	1.45	9.0
D10L2	10	2.54	4.75	4.75	1.525	8.9
D10L3	10	2.54	4.5	4.5	1.585	9.2
D12H	12	2.85	2.75	2.75	2.02	9.0
D12L	12	1.27	5.25	5.25	2.00	11.2
D20L1	20	1.28	4.7	4.7	1.586	4.9
D20L2	20	0.92	5.3	5.3	2.00	8.6
D25H	25	2.0	2.54	2.54	1.61	2.9
D25M	25	1.6	2.54	2.54	1.71	2.7
D25S	25	1.2	2.54	2.54	1.915	2.7
D40H	40	1.47	2.11	2.11	1.58	1.4
D40L1	40	0.80	5.36	5.36	1.59	4.0
D40L2	40	0.63	5.3	5.3	1.97	5.8
D100	100	1.5	1.2	1.2	1.57	0.5
CP20	20	1.28	5.0	2.35	CP design values shown in Section 3.5	
CP40	40	0.93	5.3	2.45		

Table 3.1 Dimensions, Theoretical Values for Resonant Frequency and Bandwidth

3.2 Feed Excitation Structures

In all experimental work the characteristic impedance of the microstrip or coaxial transmission line used to feed the antenna element was 50 ohms. The objective in terms of design of the excitation structure is to match the DRA directly to the transmission line without the use of a matching circuit. Being able to match the antenna directly to the

transmission line results in a more compact, low loss (less circuitry) solution with a shorter potential design cycle.

The lowest order modes of rectangular DRA have been shown to be excited by probe, aperture and direct microstrip line coupling techniques, Section 1.4.2. The following is a qualitative discussion of the application of these techniques to the L-Band DRA that were used in this investigation.

3.2.1 Probe Feed Excitation

The probe feed excitation structure matched most of the measured DRA to 50 ohms characteristic impedance transmission line by adjusting the height and width of the probe. The probe feed structure consists of a probe butted up against the side of the DRA element as shown in Figure 3.1. The coupling of the probe and the DRA was observed to be very sensitive to the surface contact, or air gap, between the metal and the dielectric. Another common method of implementing the probe excitation is to drill a hole in the dielectric and insert the probe inside the DRA. This technique has also been reported to be very sensitive to the surface contact between the probe and the DRA.

The E_y component of the electric field for the TE_{111}^{z} mode can be seen from Equation 2.17 to be maximum at the edge of the DRA, at $z=0$, $|x|=a/2$. The strength of coupling from the probe to the DRA can also be varied by moving the probe parallel to the X axis which requires holes to be drilled in the dielectric. Moving the probe parallel to the Z-axis results in an increase in cross polarization by exciting the TE_{111}^{x} mode. The technique of probe feeding inside the DRA has been reported to obtain larger coupling than edge feeding even though the Y-directed electric field intensity is less. [61]

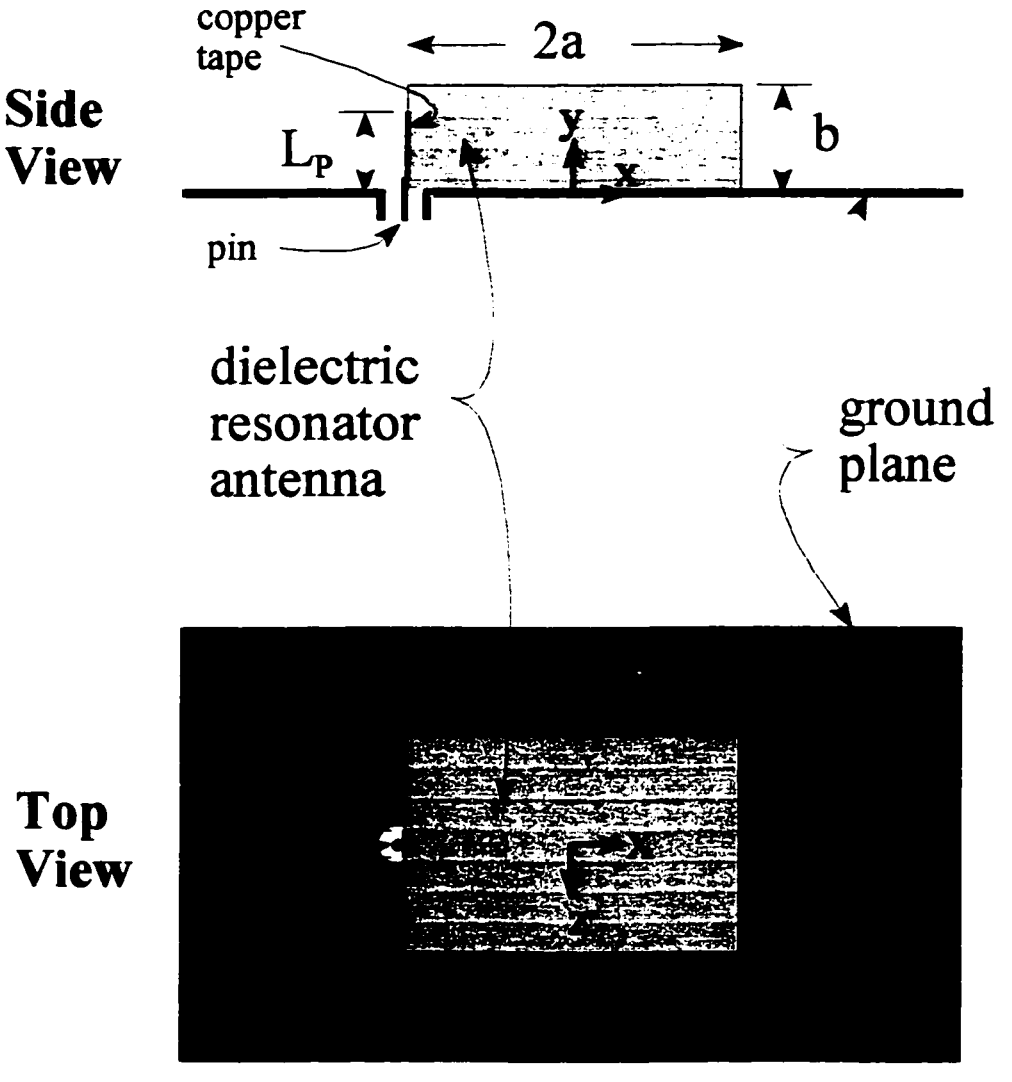

Figure 3.1
Dimensions of Rectangular DRA and Probe Feed

The input impedance of a probe is a function of the electric field **E** around the probe and the current density **J** on the probe :

$$Z_{probe} \propto \left(\int \boldsymbol{E} \cdot \boldsymbol{J} dV \right)^2 \tag{3.1}$$

The electric field for the TE_{111}^{Z} mode is tangential to the wall of the dielectric at the probe location and is not substantially affected by any air gap, since the tangential electric field is continuous across a dielectric interface. The current distribution on a probe is a function of the permittivity of the surrounding medium, Equation 3.2, which in this case would be between that of air and the permittivity of the dielectric.

$$\boldsymbol{J} \propto \sin(\sqrt{\epsilon_r} k_0 (y - l)) \tag{3.2}$$

The best implementation in terms of repeatability and range of coupling achievable was accomplished by implementing the probe as piece of copper tape. The glue backing on the tape was used to maintain a consistent separation between the metal of the probe and the dielectric. The increased surface contact to the higher dielectric, as compared to a typical cylindrical probe, increased the current density on the probe and increased the strength of coupling, similar to the effect observed for a probe inserted into a hole in the dielectric. With the use of the copper tape as a probe, matching to DRA with low dielectric constants (ε_r=10) was not a problem. However, the difficulty Mongia reported matching to low profile DRA was observed, but at the lower aspect ratio of 1/4 for the copper tape as opposed to ½ for the cylindrical probe.

The copper tape as probe technique lent itself well to rapid prototyping of elements in terms of critically coupling to the DRA for measurement of the resonant frequency and bandwidth. The probe itself can be fed through the ground plane from a microstrip or coaxial transmission line. Probe coupling has been used to excite linear, dual linear, and circular polarization [46].

3.2.2 Aperture Feed Excitation

The magnetic field of a microstrip transmission line can be coupled through an aperture in the ground plane to excite the TE_{111}^{Z} mode in a DRA, Figure 3.2. The impedance match of this structure can be adjusted over a small range by trimming the matching stub on the microstrip line and over a large range by adjusting the position of the DRA over the aperture.

This method of excitation of the DRA can be considered to be the dual of the probe feed excitation. The magnetic field produced by the microstrip line is primarily parallel to the length of the aperture in the ground plane. To the DRA the aperture appears as a magnetic current source in the Z-direction, dual to the Y-directed electric current source of the probe feed. From Equation 2.17, it can be seen that a Z-directed aperture of negligible width will couple to the H_z field of a rectangular DRA placed over the aperture and excite the TE_{111}^{Z} mode. Practically, the width of the aperture is kept very small compared to the length, so that coupling from the microstrip line is constrained to the desired magnetic field of the DRA.

The cross polarization performance of the aperture feed is more robust than the probe feed since the DRA must be rotated with respect to the aperture to excite both the TE_{111}^{Z} and TE_{111}^{X} modes. For a square DRA, the excitation of the orthogonal mode results in a rotation of the axis of polarization. For a rectangular DRA where the resonant frequencies of these modes are different from each other the angled aperture provides a means of generating from a single feed a dual frequency/dual linearly polarized antenna or a circularly polarized antenna.

The aperture feed excitation has the advantage of isolating the radiating surface of the antenna from the corporate feed circuitry and signal processing elements. This eliminates any potential coupling between the radiating elements and the feed elements, leaves more substrate space for the feed, and makes protecting the feed structure from the

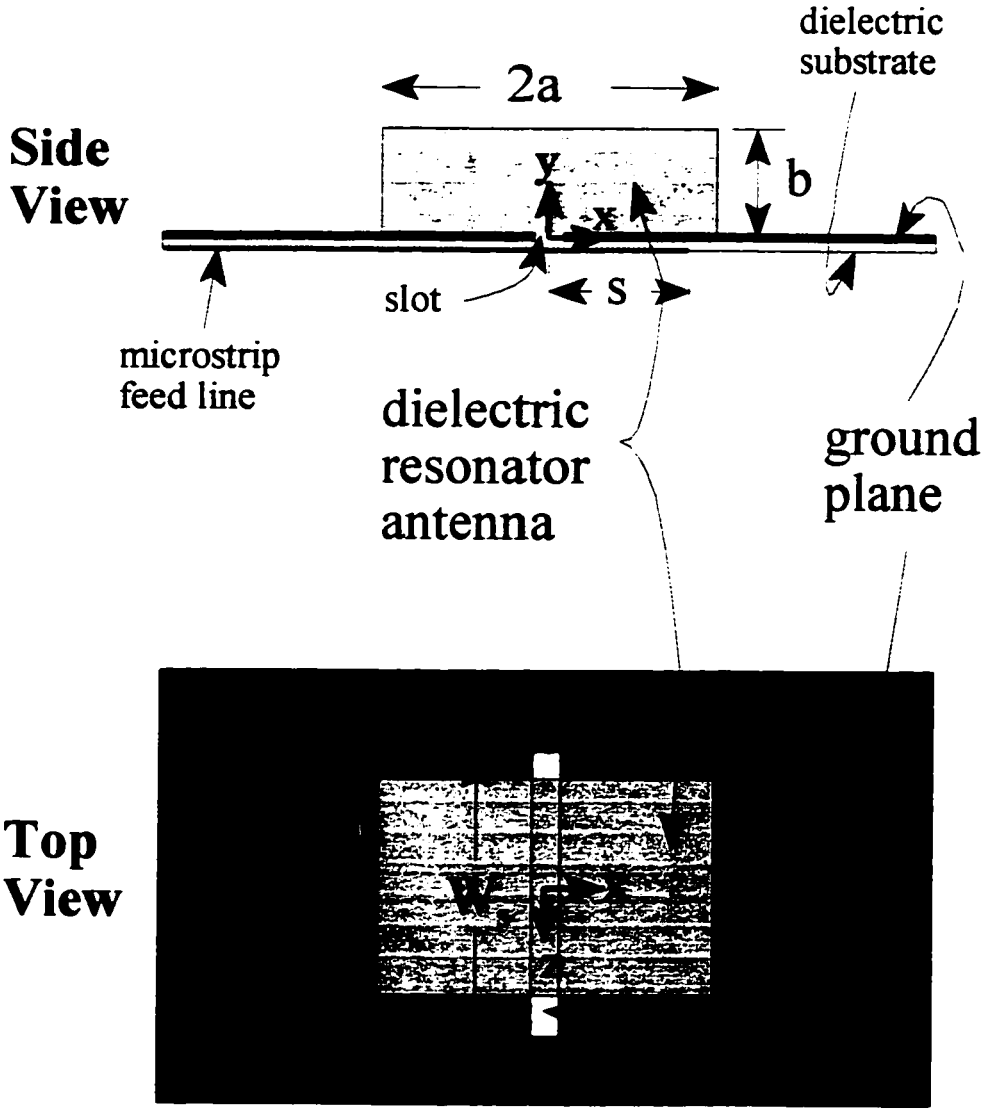

Figure 3.2
Dimensions of Rectangular DRA and Aperture Feed

environment easier. The impedance bandwidths measured for DRA excited by an aperture were similar for the same DRA excited by a probe.

The microstrip substrate used had a dielectric constant of 2.5 and a thickness of 0.079 cm. The width of all microstrip lines used in probe, direct microstrip and aperture coupling were designed for a characteristic impedance of 50 ohms, which resulted in a line width of 0.224 cm. Several different size of apertures were used, Table 3.2. The microstrip stub length (S), the length of the open circuited microstrip line after the aperture was selected to be $\lambda_g/4$ at a frequency of 1.6 GHz. The effect of the stub length on the strength of coupling to the DRA was not as significant as was choice of aperture size and the placement of the DRA with respect to the aperture. The effect of different stub lengths was not rigorously investigated and may have affected the measured value of resonant frequency slightly.

Aperture Designation	Length of Microstrip Stub (S) (cm)	Length of Aperture (L_s) (cm)	Width of Aperture (W_s) (cm)
S1	3.2	0.3	1.5
S2	3.2	0.3	1.75
S3	3.2	0.3	2.0
S4	3.2	0.3	2.25
S5	3.2	0.3	2.5
S6	3.2	0.3	2.75
S7	3.2	0.3	3.0

Table 3.2 Slot Feed Dimensions

3.2.3 Direct Microstrip Feed Excitation

The simplest feed excitation method is the direct microstrip coupling. The DRA is placed directly on the end of an open circuited microstrip line, Figure 3.3, with the DRA overlapping the microstrip line by a small amount, typically on the order of $0.02\lambda_0$. The overlap distance controls the strength of coupling, and varies with the dielectric constant and dimension of the DRA. In general this method did not produce an impedance match to the 50 ohm microstrip transmission line that was used to excite the DRA, see Annex A. Typically the DRAs were under coupled, with a real impedance value of 10-30 ohm. For linearly polarized series arrays such as those demonstrated by [49] which do not require a 50 ohm element match, the simplicity of the direct microstrip feed structure is attractive.

The direct microstrip to DRA coupling shown in Figure 3.3 excites both TE_{111}^{z} and TE_{111}^{x} modes, although much stronger coupling occurs to the TE_{111}^{z} mode. As with the other feed excitation techniques, misalignment of the DRA with respect to the microstrip line can excite the other (TE_{111}^{x}) linear mode [61].

The direct microstrip feed excitation has the advantage of locating the feed and antenna elements on the same substrate for an array implementation, allowing the circuit board to be securely supported at the back of the ground with a completely rigid structure. This means that the DRA are directly supported by a mechanical structure and not the circuit board. At L-Band the size of DRA required to achieve the desired bandwidths, Section 3.3, is such that the issue of mechanical support would be important.

As previously mentioned, the direct microstrip feed did not achieve the desired match of the DRA to the 50 ohm transmission line used, an observation also noted in [61]. A single open circuited stub or a single section of low impedance transmission line was used to transform the measured impedance to match the 50 ohm characteristic impedance of the transmission line. The objective of doing so was to provide a common reference point from which to compare the performance of the different feed excitations. This

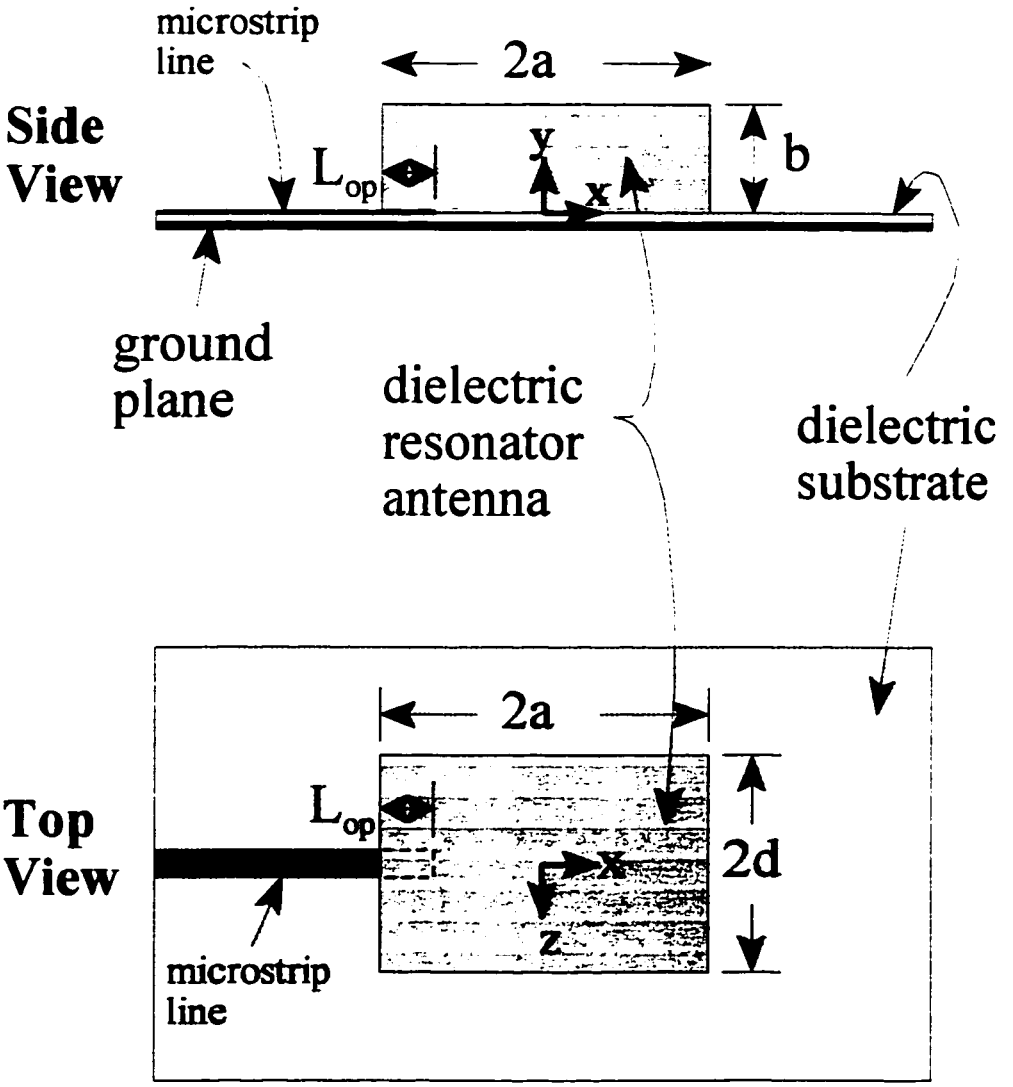

Figure 3.3
Dimensions of Rectangular DRA and Direct Microstrip Feed

matching was implemented on the actual circuit with copper tape, and on a linear circuit simulator using the measured S-parameters of the DRA. It was observed that this technique resulted in broader bandwidths than either probe feeding or aperture feeding.

3.3 Linear Polarization

Several DRA were designed using the expressions developed in Chapter 2. Dielectric constants varied from 10 to 100, and aspect ratios from cubic to low profile. The impedance bandwidth, resonant frequency and radiation patterns of these DRA were measured using the feed excitation methods described. The objective of this experiment on square planform DRA was to verify the accuracy of Equations 2.12 and 2.30, to investigate the practical aspects of implementation of the three feed excitation techniques, Figures 3.1-3.3, and to experimentally determine the minimum DRA requirements of dielectric constant, feed mechanism, and shape to achieve the PCS 1.9 and MSAT benchmarks.

3.3.1 Resonant Frequency and Bandwidth

Measurements of resonant frequency and impedance bandwidth using probe, aperture and direct microstrip feed excitation structures are shown in Tables 3.3-3.5.

DRA	Resonant Frequency (GHZ)	Impedance Bandwidth (%)
D10L1	1.315	8.2
D10L2	1.394	8.4
D10L3	1.45	7.0
D12H	1.98	10.1
D25H	1.69	3.6
D25M	1.76	3.2
D25S	1.895	4.2
D40H	1.75	1.9
D100	1.85	1.0

Table 3.3 Experimental Results using Probe Feeds

The bandwidth can be seen to be generally inversely proportional to dielectric constant. Several DRAs were measured using both aperture and probe feeds, such as D12H, D25H, D40H and D100 (Table 3.4 and 3.5). The different feed excitation methods measured consistent values, the resonant frequencies agreed to within 4% and the bandwidths to within 10% of each other.

DRA	Resonant Frequency (GHZ)	Impedance Bandwidth (%)
D12H	1.93	11.2
D12L	1.75	7.5
D20L1	1.55	5.1
D20L2	1.86	6.5
D25H	1.67	3.4
D40H	1.69	2.0
D40L1	1.61	3.5
D40L2	1.92	4.7
D100	1.77	1.0

Table 3.4 Experimental Results using Aperture Feeds

The direct microstrip feed does not match the DRA directly to the 50 ohm impedance microstrip transmission line. The two types of matching circuits that were used were a low impedance quarter wave transformer or an open circuited stub matching circuit, depending on the location of the resonance loop. These matching circuits were used because they could be implemented using copper tape without having to trim any of the printed circuit.

The measured values of resonant frequency and bandwidth for the aperture or feed excitation as compared to the direct microstrip feed are not consistent. This result is further investigated in Chapter 4.

DRA	Type of Matching	Resonant Frequency (GHz)	Impedance Bandwidth (%)
D12H	No coupling		
D20L1	quarter-wave	1.68	7.7
D25H	quarter-wave	1.87	9.0
D25M	quarter-wave	1.99	6.6
	quarter-wave plus stub	1.99	10.0
D40H	quarter-wave plus stubs	2.035	6.8
D40L1	quarter-wave	1.67	7.2
D40L2	quarter-wave		6.0

Table 3.5 Experimental Results using Direct Microstrip Feeds

3.3.2 Accuracy of Theoretical Calculations

In Table 3.6 the measured values, Tables 3.4 and 3.5, are compared to the theoretical values, Table 3.1, of resonant frequency and impedance bandwidth for the rectangular DRA excited in the TE_{111} mode. Figure 3.4 displays graphically a plot of the average prediction errors versus the dielectric constant of the DRA. The theoretical resonant frequency is high for lower values of permittivity and low for higher values of permittivity. The predicted resonant frequency is most accurate for a dielectric constant of between 20 and 25. The resonant frequency design error was within 10% for dielectric constants between 10 and 100, with the exception of D12L which was difficult to excite making the results somewhat suspect. The resonant frequency results verify the results of [58], where a prediction error of 8% was observed. The impedance bandwidth design error was within 35%, not considering the narrow band D100, with an average error of 25%.

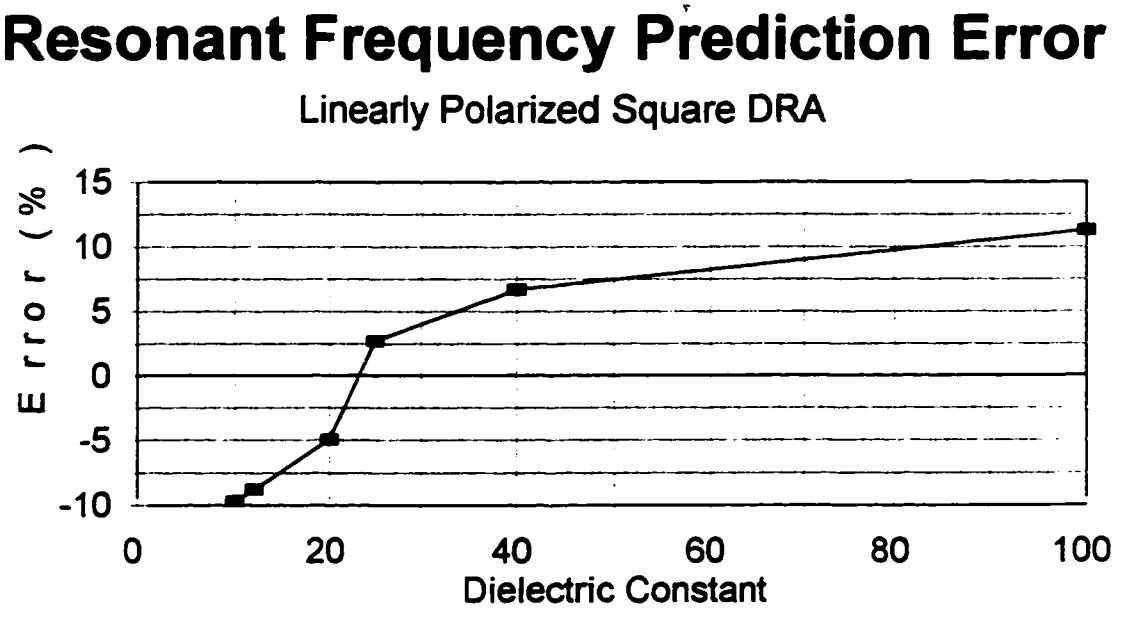

Figure 3.4
Plot of Resonant Frequency Prediction for Linearly Polarized Square DRA

DRA	Resonant Frequency Prediction Error (%)	Ratio of Calculated to Measured Bandwidth
D10L1	-10.3	1.10
D10L2	-9.4	1.06
D10L3	-9.3	1.31
D12H	-3.3	0.86
D12L	-14.3	1.49
D20L1	-2.3	0.96
D20L2	-7.5	1.32
D25H	+3.6	0.85
D25M	+2.8	0.84
D25S	-1.0	0.64
D40H	+8.1	0.72
D40L1	+1.2	1.14
D40L2	-2.6	1.23
D100	+11.3	0.50

Table 3.6 Prediction Error for Rectangular DRA Theory

These results verify that concept of the truncated dielectric waveguide, and therefore the field structure of Equation 2.17, is a useful model of the behaviour of the lowest order TE_{111} mode resonance of the rectangular DRA.

3.3.3 Radiation Pattern

The radius of the two ground planes used was approximately 0.2m and 0.5m, which corresponds to an average normalized radius of λ_0 and 2.5 λ_0. The 2.5 λ_0 radius ground plane was the largest that could practically be implemented in the anechoic

chamber used. The DRA was used as the receiving antenna, while a directional horn was used as the transmitter. The DRA was rotated about a vertical axis located at the centre of the front face of the DRA, which was approximated as the phase centre for the DRA.

Measured radiation patterns of the principal radiation planes of a representative DRA (D25H) are shown in Figure 3.5. The ripple superimposed on the radiation pattern comes from interference due to scattered energy from the edges of the ground plane [60]. The scale of the ripple on the patterns makes it difficult to precisely determine the beamwidth of the radiation pattern. However, the results were similar to those recorded in [50] with an E-plane beamwidth that is nearly omni-directional and a broad H-plane beamwidth, as predicted by the method of Section 2.4. All measurements were performed using the large ground plane since it generated a smaller ripple than did the small ground plane.

The magnitude of the cross polarization component was less than -15 dB of the level of the principal polarization for probe, aperture or direct microstrip feed excitation for the square planform DRA, Annex A . The good cross polarization performance of the square planform DRA illustrates the isolation between the degenerate TE_{111}^{x} and TE_{111}^{z} modes, and the success with which the three feed excitation structures exclusively excite the desired resonant mode.

3.4 Dual Linear Polarization

Several of the square planform DRA were implemented as dual linearly polarized antennas, Figure 3.6. The objective was to generate spatially orthogonal polarization patterns at the same frequency, with high isolation between the feed ports. Probe feeding was used because it was the simplest to implement, however dual aperture feeds or dual direct microstrip feeds should work as well since the values of cross polarization measured

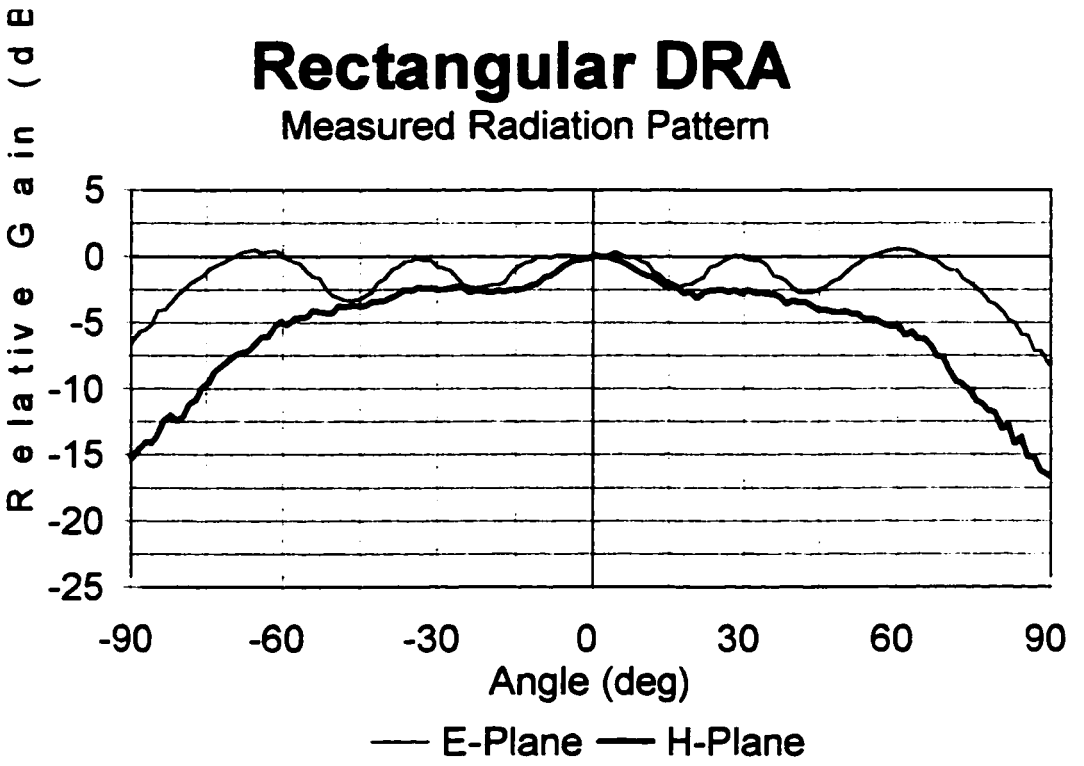

Figure 3.5
Typical Measured Radiation Pattern for DRA

for the three feed structures were equally low.

The presence of a second probe, located at x=0, z=-d, has little effect on the behaviour of the TE_{111}^{z} mode excited by the first probe. The fields of the TE_{111}^{z} mode at the line x=0, z=-d are given by :

$$\begin{aligned} E_x &= K_1 \sin(k_y y)\cos(k_z z) \\ E_y &= 0 \\ E_z &= 0 \\ H_x &= 0 \\ H_y &= K_2 \sin(k_y y)\cos(k_z z) \\ H_z &= A \cos(k_y y)\cos(k_z z) \end{aligned} \qquad \textbf{(3.3)}$$

Coupling to the second probe would occur most strongly for the electric field parallel to the probe, E_y, and the magnetic field directed around the probe, H_x and H_z. The second probe is located in a null for those components of the TE_{111}^{z} mode, resulting in minimal coupling to the probe and high isolation between the ports.

The D25M and D40H DRA were implemented as probe fed dual linearly polarized antennas as shown in Figure 3.6. The measured cross polarization level was at least as good as for a single probe. The isolation between the two feed ports was better than 27 dB across the bandwidth of the DRA, Appendix C. The isolation between the ports for the probe fed rectangular DRA is much better than that of a broadband probe or direct fed printed patch antenna (isolation of 10 to 20 dB), and better than that reported in Section 1.3.1 for dual slot feeds (isolation of 22 dB). This feature of the dielectric resonator antenna makes it an excellent candidate for a polarization diversity antenna for a PCS 1.9 type application.

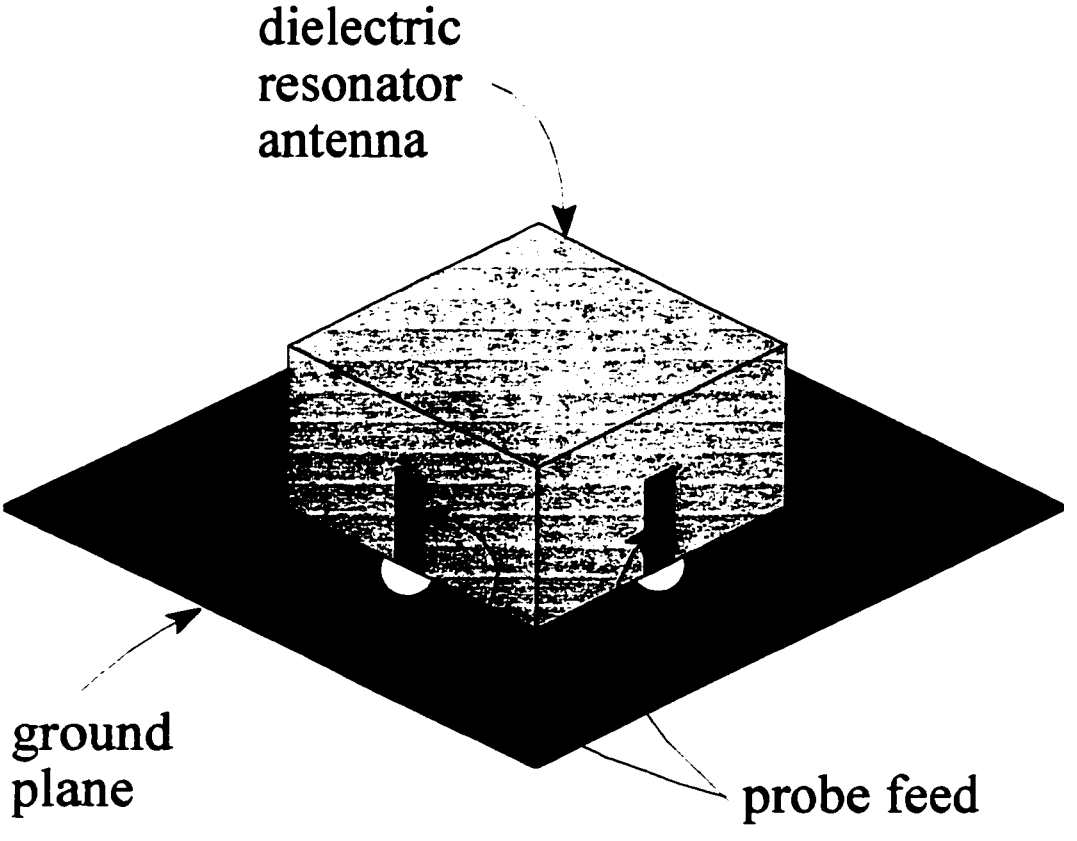

Figure 3.6
Dual Linearly Polarized Probe Fed DRA

3.5 Circular Polarization

Several rectangular DRA were designed using the technique described in Section 2.3. The objective of the design and measurement of rectangular circularly polarized dielectric antennas using this method was to verify the design procedure, and to verify the experimental results that were reported in literature. The dimensions of the two CP DRA elements can be found in Table 3.1. Table 3.7 lists the predicted values for the resonant frequency and impedance bandwidth of the two orthogonal linear TE_{111} modes. The predicted values of frequency of circular polarization and of design error are shown.

DRA	CP design Frequency (GHz)	TE_{111}^{X} mode		TE_{111}^{Z} mode		CP Error Function
		Resonant Frequency (GHz)	Impedance Bandwidth (%)	Resonant Frequency (GHz)	Impedance Bandwidth (%)	
CP20	1.855	2.015	5.0	1.731	4.35	0.035
CP40	1.577	1.651	2.25	1.511	2.12	0.042

Table 3.7 Theoretical Values of CP Designed DRA

3.5.1 Experimental Results

The CP DRA were excited linearly as in Section 3.3 to measure the properties of the orthogonal linear modes. The CP DRA were then excited as shown in Figure 2.4 to generate circular polarization. A linearly polarized horn antenna was used for all radiation measurements in the anechoic chamber. When measuring the circularly polarized DRA the linearly polarized transmitting antenna was spinning around the axis perpendicular to the linear polarization vector. The measured parameters of the circularly polarized radiation were axial ratio, read off the plot as the peak to valley swing of the received power, and beamwidth, which was measured as the range of angles over which a specified

axial ratio was maintained.

The measurements of the CP DRA aperture fed to excite the TE_{111} linear polarization modes are listed in Table 3.8. Slot S3 was used for both CP20 and CP40.

DRA	TE_{111}^{x} mode		TE_{111}^{z} mode		CP Error Function
	Resonant Frequency (GHz)	Impedance Bandwidth (%)	Resonant Frequency (GHz)	Impedance Bandwidth (%)	
CP20	1.924	4.9	1.72	3.4	0.012
CP40	1.825	2.4	1.6	2.8	0.100

Table 3.8 Linear Polarization Measurements on CP DRA

The linear mode design prediction errors are shown in Table 3.9. It is evident that the relative error in predicting the resonant frequency and bandwidth is different for the two orthogonal modes. The prediction errors for CP20 were complementary, reducing the CP design error by a factor of 3. The prediction errors for the resonant frequency and bandwidth of the linear modes for CP40 increased the CP design error by a factor of 2.4. This shows the dependence of this CP design procedure on the accuracy of the linear model.

DRA	CP design Frequency	TE_{111}^{x} mode		TE_{111}^{z} mode		CP Error Function
		Resonant Frequency	Impedance Bandwidth	Resonant Frequency	Impedance Bandwidth	
CP20	-2.6 %	-4.7 %	1.02	-0.6 %	1.3	3x better
CP40	7.8 %	9.5 %	0.94	5.6 %	0.76	2.4x worse

Table 3.9 Prediction Error for CP DRA

To generate circular polarization the DRA was angled at 45 degrees with respect to the aperture geometry as shown in Figure 2.4. Slot S5 was used for CP20 and S3 was used for CP40. Table 3.10 lists the centre frequency, the impedance bandwidth, the 3dB axial ratio bandwidth, and the 3dB axial ratio beamwidth of the measured circularly polarized radiation. The input match to CP40 was not better than -10 dB, so an impedance bandwidth was not listed. Network analyser measurements of the linear and circular mode resonances shown in Appendix D illustrate the conceptual design procedure of Section 2.3.

DRA	CP Centre Frequency (GHz)	Impedance Bandwidth (%)	3 dB Axial Ratio Bandwidth (%)	3 dB Axial Ratio Beamwidth (deg)
CP20	1.808	13.3	3.5	100
CP40	1.71	-	1.1	60

Table 3.10 Circular Polarization Measurements on CP DRA

The design procedure for the circularly polarized rectangular DRA, outlined in Section 2.3, was experimentally verified. The experimental results for the single aperture fed rectangular DRA agreed with the impedance and axial ratio bandwidths reported in [46].

3.5.2 Practical Usefulness

The results from Oliver show the performance of the near cube shaped DRA with a dielectric constant of 10 to be close to the MSAT benchmark of 1.2.2. With a dielectric constant of 10, the DRA is compact enough to be closely packed for use in an array with the tilted beam peak. The wide beam pattern of the DRA would improve array efficiency as shown in [10].

The simple analytic design methodology developed by Oliver for the rectangular CP DRA is a practical means of design. While prediction errors of the resonant frequencies and bandwidths of the linear modes can be significant, the errors can easily be quantified with network analyser measurements and the DRA dimensions modified accordingly to minimize the CP design error. The ability to make those measurements on the individual linear modes of the DRA is a major advantage for this element, since measuring the radiation patterns of each prospective design would be an expensive and time consuming process.

3.6 Parasitic Array

The objective of this investigation was to determine the feasibility of using a circularly polarized DRA as the feed element of a parasitic array to achieve a circularly polarized beam pattern squinted to low elevation angles, as was demonstrated with microstrip patches [11]. This technique of beam squinting has the advantage of a simple feed with only one driven element. Petosa reported in [47] a four element parasitic DRA array which squinted the H-plane pattern. An experimental investigation was undertaken to implement a dual polarized squinted beam with a parasitic array of dielectric resonators, Figure 3.7.

3.6.1 Experimental Results

The H-plane beam squint result of Petosa was verified and an E-plane squinted array was demonstrated. However, for a fixed parasitic element spacing achieving a simultaneous beam squint in the E-plane and the H-plane was difficult. The frequency dependent beam squints of the two planes was different and narrowband. Figure 3.8 show the best simultaneous beam squint achieved, using D25H as the driven element and 3 D25S spaced 0.017 λ_0 apart as the directive elements. A reflector element was not shown to improve the patterns. At 20 degrees elevation the difference between the two polarizations has been reduced from 7.5dB for a single element to 2.5dB for the array,

however a large null was observed at 45 degrees in the E-plane pattern. It was not investigated what effect the ground plane had on the radiation pattern.

3.6.2 Practical Usefulness

The potential for implementing a circularly polarized pattern squinted towards the zenith with an array of parasitic DRA was demonstrated. However, the narrowband nature of the beam squinted patterns is not a good use of the intrinsically broad band DRA and implementation of an array of this form does not seem to be practical.

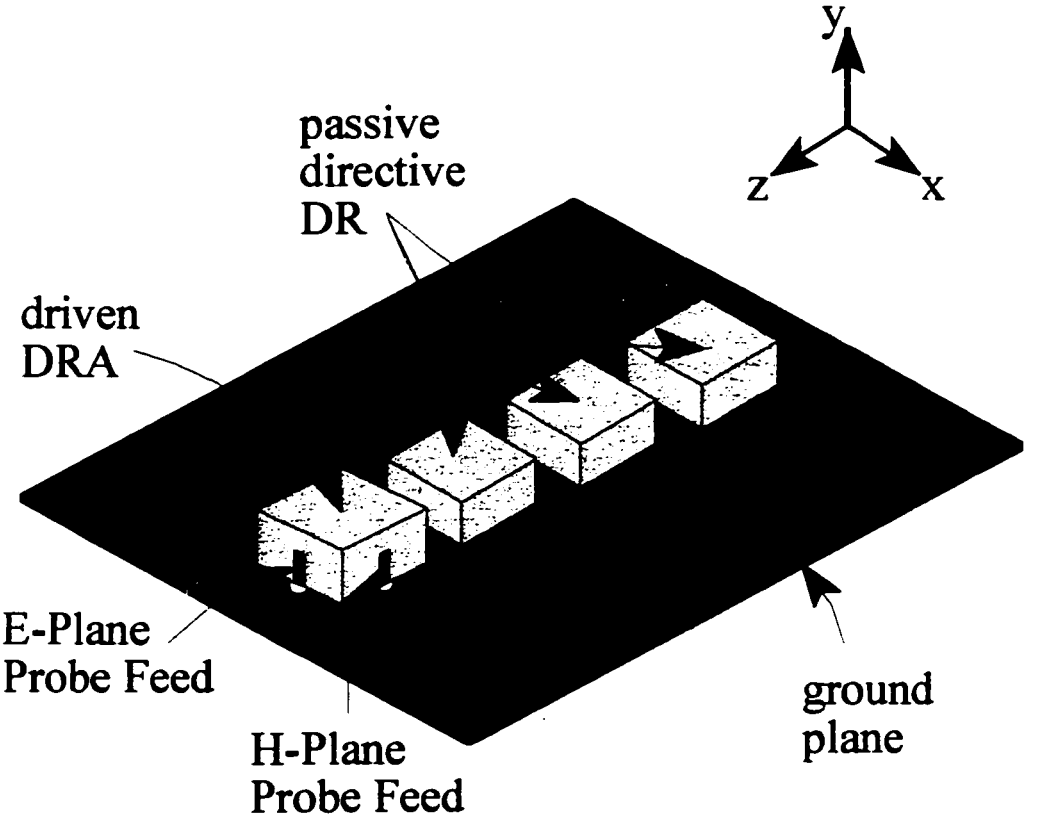

Figure 3.7
Dual Linearly Polarized 4 Element Parasitic Array of DRA

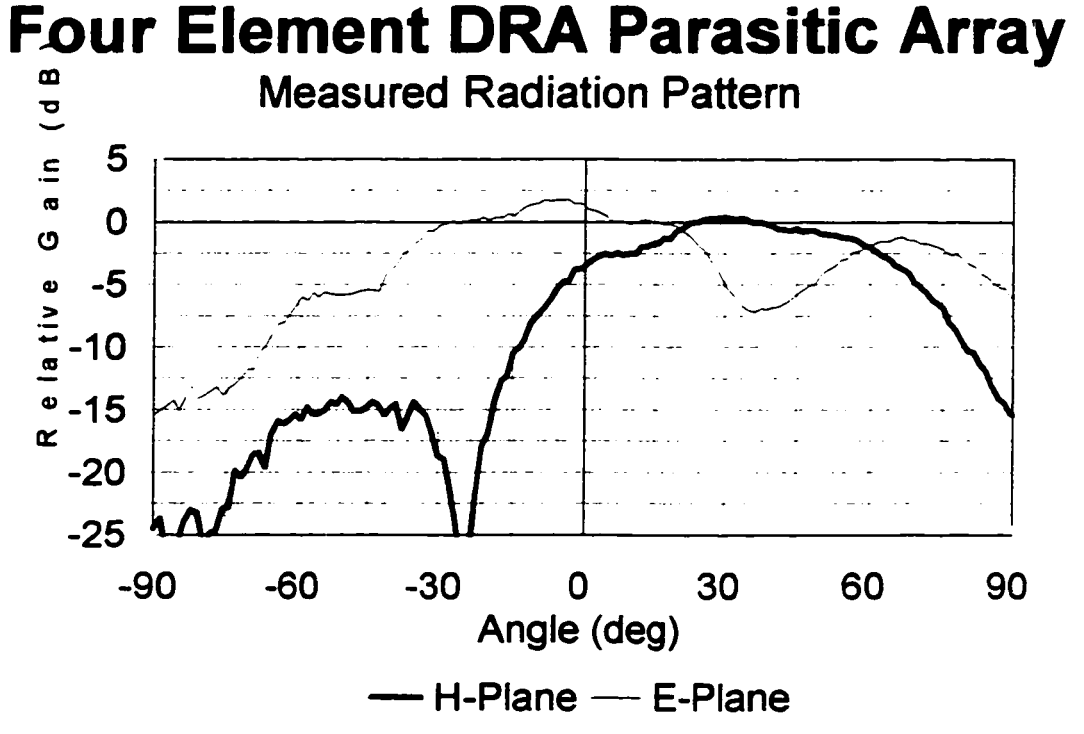

Figure 3.8
Measured Radiation Pattern 4 Element Parasitic Array of DRA

Chapter 4

Multi-Segment Rectangular DRA

4.1 General

The work presented in Chapters 4 & 5 is novel experimental and theoretical work on modifications to the rectangular dielectric resonator antenna. The objective of the development of a modified rectangular DRA was to produce a more compact and broadband DRA than was possible with the homogeneous rectangular DRA. The focus of the experimental and theoretical work is on the geometry, resonant frequency and impedance bandwidth of these elements. Few measurements were taken of the radiation patterns of these elements beyond verifying that the radiation was similar to the radiation of the horizontal magnetic dipole TE_{111} mode. Chapter 4 covers the analysis and results for the implementation of the probe fed rectangular multi-segment dielectric resonator. A theoretical model of the novel homogeneous edge-grounded DRA is developed and compared to measured results in Chapter 5. Chapter 5 also includes analysis and results of the compact broad band edge-grounded multi-segment DRA.

The theory of the TE_{111} mode resonance of the rectangular dielectric antenna will be applied to understand and to attempt to predict the behaviour of these modified

rectangular dielectric resonator antennas. Assumptions about the nature of the internal fields of the new structures will allow the design equations developed in Section 2.2 for the homogeneous DRA to be used to predict the resonant frequency and bandwidth of the modified DRA.

4.2 DRA Bandwidth Standard Comparison

At this point it will be discussed what more compact and increased bandwidth mean in the context of a DRA. The broad band modifications to DRA presented here, as well as the ones from literature such as [33][35][42], are designed to increase the bandwidth of the DRA. However, DRA can be made in many aspect ratios and dielectric constants, so if a two DRA with dielectric constants of 40 and a bandwidth of 5% are stacked to produce an element with similar radiation properties and a bandwidth of 15%, is this an improvement in bandwidth? Well, it is an improvement over the performance of the individual DRA, but the stacked element is much larger. If a single DRA of arbitrary dielectric constant and the same size as the stacked element resonates at the same frequency and has the same impedance bandwidth, then the stacked structure is not an improvement over a single DRA.

The use of this standard is one of the criteria that will be used in the evaluation of the modified DRA. For each modified structure, a regular DRA of the same total dimensions will be designed to have the same resonant frequency as the measured resonant frequency of the modified DRA. The ratio of the measured bandwidth of the modified DRA to the bandwidth of the regular DRA standard will be used as a tool to quantify the bandwidth improvement achieved with the various different modifications.

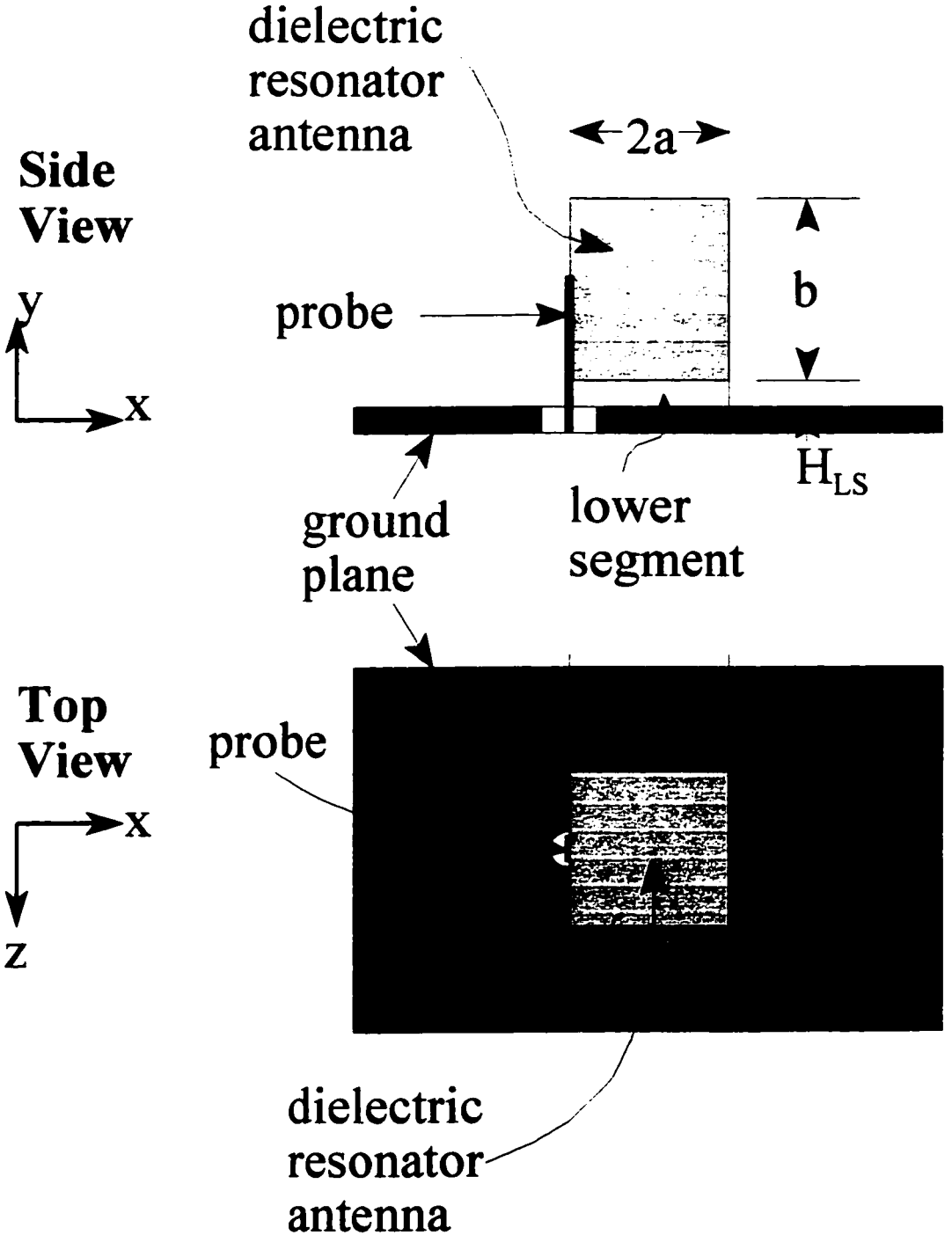

Figure 4.1
Dimensions of Rectangular Multi-Segment DRA and Probe Feed

4.3 Introduction

The multi-segment dielectric resonator antenna is shown in Figure 4.1. A number of different implementations of multi-segment and stacked DRAs have been reported to increase the impedance bandwidth of different modes of both cylindrical and rectangular DRAs. The multi-segment DRA, as labelled by Petosa [42], uses thin non-resonant dielectric layers placed between a DRA and the ground plane. The stacked dielectric resonator antenna uses multiple DRA segments [33] [35]. For the experimental work presented here only two layer multi-segment DRAs were considered, where the top layer was one of the DRAs of Table 3.1 and the thinner bottom layer was a low dielectric constant material (ε_r=1 to 4). For all reported results the dielectric constant of the lower segment was 2.0. The exception to the rule is for lower segment heights (d) of 5.0 and 10.0 mm, for which the dielectric constant was 4.0.

The initial motivation behind the implementation of this structure was the observation from Section 3.3 that the direct microstrip feed excitation technique resulted in the largest impedance bandwidths. A comparison of probe fed DRAs implemented normally and as in Figure 4.2 was performed to investigate the broad band effect that was observed when the direct microstrip feed was used. As can be seen from Table 4.1, it was the insertion of the thin substrate material between the DRA and the ground plane which resulted in the increase in the impedance bandwidth observed with the direct microstrip feed technique.

DRA	Feed Configuration	Lower Segment Height (mm)	Resonant Frequency (GHz)	Impedance Bandwidth (%)
D12H	Coaxial probe	0	1.974	9.4
	Probe from proximity microstrip line	0	2.058	12.0
		0.9	2.112	13.4
D25S	Coaxial probe	0	1.848	3.8
		0.9	2.112	6.25
		1.8	2.184	6.9
	Probe from proximity microstrip line	0.9	2.148	7.0

Table 4.1 Results of Probe Fed DRAs on Ground Plane and on Dielectric Substrate

Measurements were made on many multi-segment DRAs to observe the effect of the thickness of the lower segment on the frequency and bandwidth of the DRA. The probe feed excitation technique was used exclusively since the lower segments had low dielectric constants, and neither the direct microstrip nor the slot feed excitation techniques couple energy well into very low permittivity materials.

The objective of this experimentation was to determine the magnitude of improvement of the impedance bandwidth that was possible over that of a normal homogeneous rectangular DRA. The theoretical analysis attempted to model the multi-segment DRA as a homogeneous DRA in order to use the previously developed equations to predict resonant frequency and bandwidth.

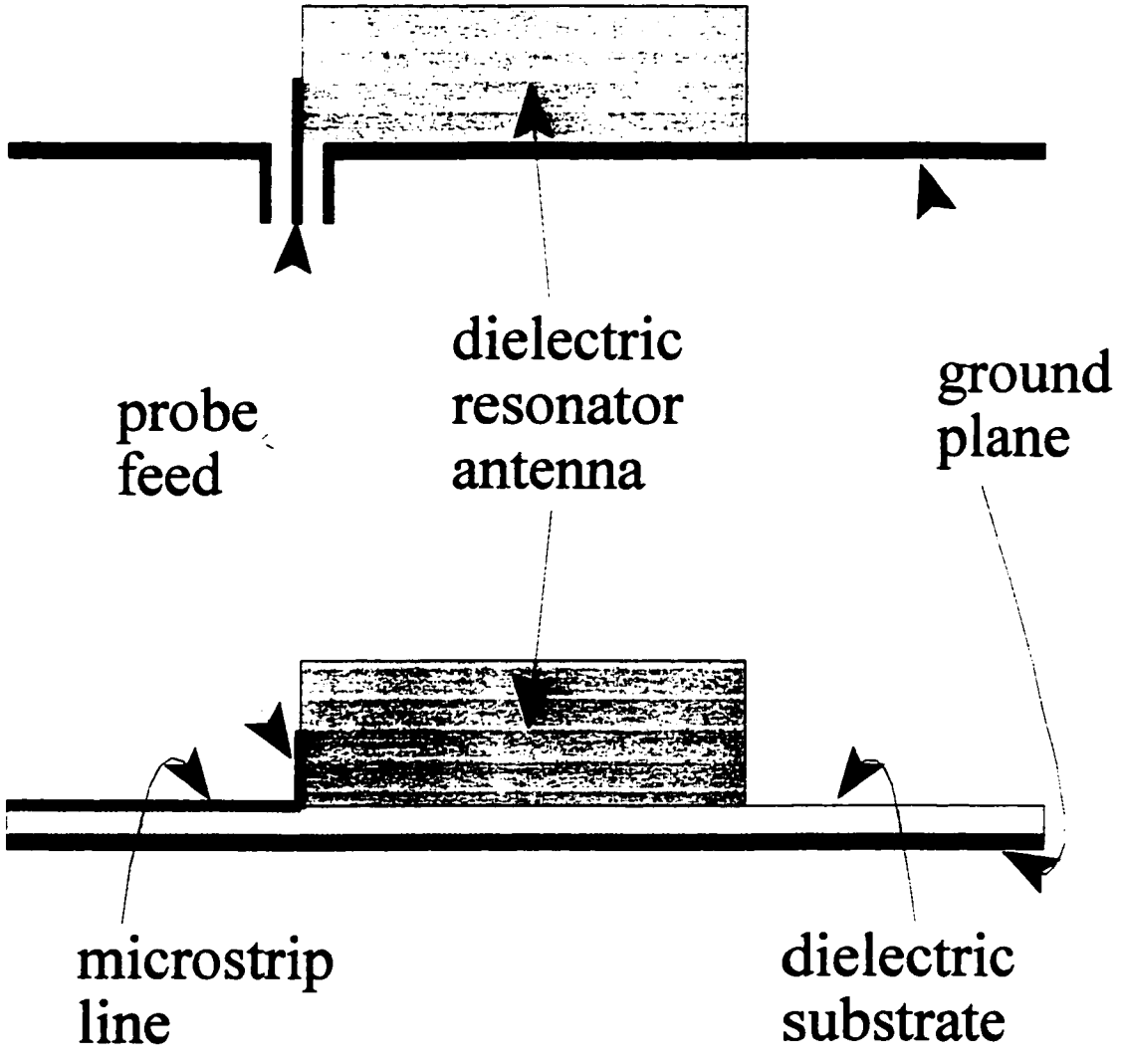

Figure 4.2
Probe Through Ground Plane Versus Probe From Microstrip Line

4.4 Theoretical Analysis

The resonance of this structure is not of the same straight forward TE_{111} form as for the homogeneous DRA. For the multi-segment DRA made up of a higher dielectric constant body and lower dielectric constant spacer. The limiting cases of the lowest order TE_{111}^{Z} modes are shown conceptually in Figure 4.3. The term 'limiting' refers to frequency of operation. At one extreme, there is no lower segment and the resonator is placed directly on the ground plane. This corresponds to the lowest possible resonant frequency of the multi-segment DRA. At the other extreme the height of the lower segment of the multi-segment DRA is so large that the effect of the ground plane is insignificant on the resonance of the DRA. This corresponds to the resonant frequency of the isolated DRA which represents the upper limit of the resonant frequency of the multi-segment DRA. Since the geometry of the multi-segment DRA lies between the two extremes, so should the resonance frequency. Inspection of the two principal modes of the limiting cases for the multi-segment DRA does not lead to a simple prediction for the impedance bandwidth of this structure.

Figure 4.4 shows a conceptual cross sectional view of the expected field structure of the hybrid mode for the multi-segment DRA. The magnetic wall boundary conditions are maintained at the air interfaces of the upper dielectric segment. This structure could be analysed similarly to the theoretical treatment of the homogeneous rectangular dielectric waveguide presented in Chapter 2, however the field structure is significantly more complicated and that form of analysis was left for future development.

When comparing the multi-segment DRA to the limiting case of just the top segment on a ground plane, the wave number k_x will be unchanged and k_z would be expected to be similar to the value calculated for the regular DRA of dimension '2a x b x 2d', since wave numbers are mainly determined by the air/dielectric interface. The wave number k_y could be smaller or larger depending on whether the magnetic wall boundary

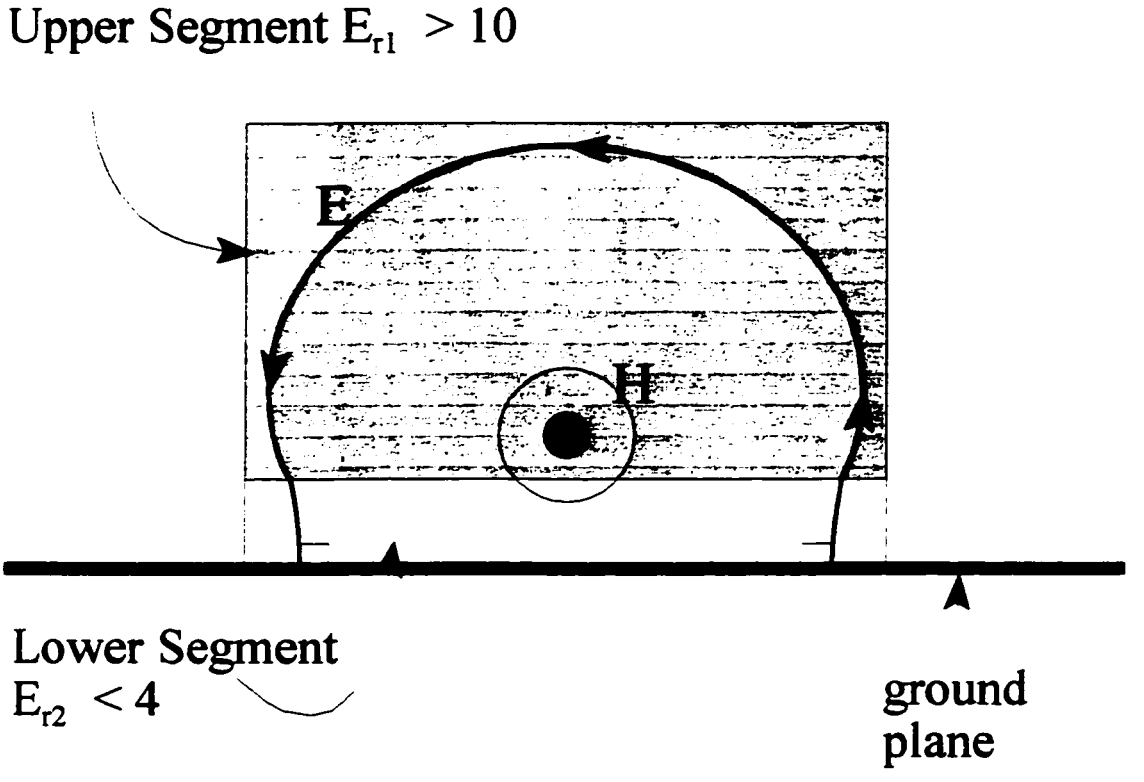

Figure 4.3
Limit Cases of Thin and Thick Lower Segments

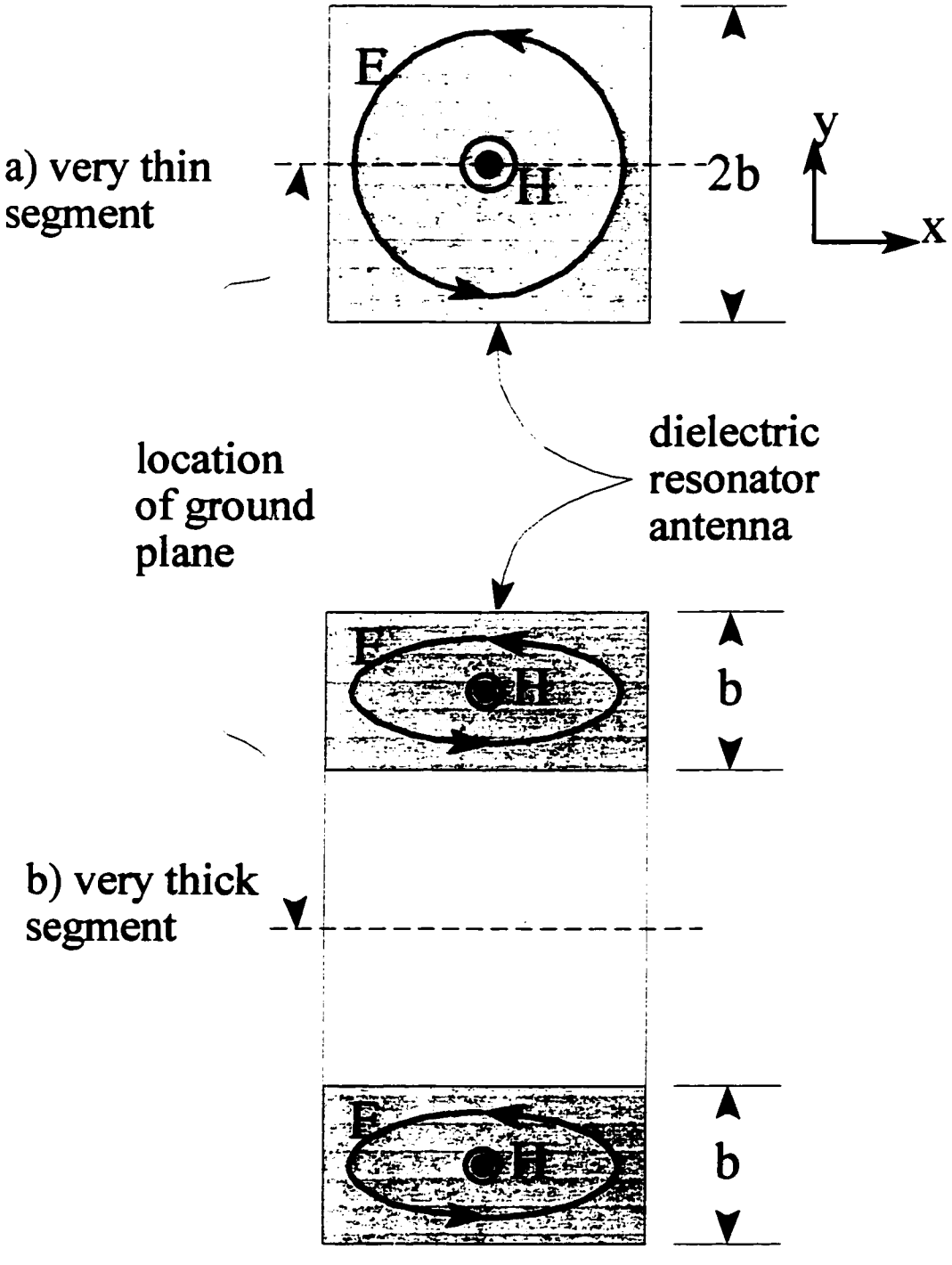

Figure 4.4
Conceptual Orientation of Transverse Electric Field for Multi-segment DRA

condition was more strongly supported in the upper or lower segment, see Figure 4.4. For the selection of segment geometry and relative dielectric constant in this investigation, the magnetic wall boundary condition is always more strongly supported in the upper segment. Thus the value for k_y would be less for the multi-segment DRA, confirming the conceptual field structure of Figure 4.4 is reasonable.

Using the simple design relations developed for the TE_{111} mode, it was investigated whether a single 'average' value for dielectric constant could be used to predict the resonant frequency and bandwidth for this structure. This model would approximate the different values of dielectric constant in the y-direction by an average value. Since the wavelength in a dielectric is proportional to the square root of the dielectric constant, a first order average value can be determined from the expression :

$$\sqrt{E_{r_{AVG}}} = \frac{b\sqrt{E_{r_{upper}}} + H_{LS}\sqrt{E_{r_{lower}}}}{b + H_{LS}} \qquad \textbf{(4.1)}$$

The dimensions of the DRA to be used in the calculation of its electrical properties using the average value of dielectric constant are the total dimensions of the multi-segment DRA as shown in Figure 4.1 (2a x 2{b+H_{LS}} x 2d). The average value concept for the dielectric constant predicts values for resonant frequency and bandwidth between the limits described in the previous paragraph on the extreme cases.

DRA	H_{LS} (mm)	Average Dielectric Constant			Limit $H_{LS} = 0$		Limit $H_{LS} = \infty$	
		ε_{avg}	f_{res} (GHz)	BW (%)	f_{res} (GHz)	BW (%)	f_{res} (GHz)	BW (%)
D10L1	0.9	9.6	1.46	9.4	1.45	9.0	2.2	13.65
	3.6	8.7	1.472	10.6				
D10L3	10	8.0	1.60	13.0	1.59	9.2	2.29	12.3
D25S	0.9	23.1	1.75	3.1	1.92	2.7	2.92	4.1
	1.65	24.8	1.78	3.3				
	5	17.0	2.03	4.5				

Table 4.2 Prediction of Multi-Segment DRA using Average Dielectric Constant

The principal resonant modes of both limiting cases have similarly broad boresight directed patterns and thus it is expected that the multi-segment structure would have a radiation pattern similar to that of the TE_{111} mode, as seen in other multi-segment DRA in the literature.

4.5 Experimental Results

Table 4.3 lists the measured resonant frequency and impedance bandwidth for several multi-segmented DRA. Impedance bandwidths of up to 40% were recorded.

DRA	Lower Segment Height (mm)	Resonant Frequency (GHz)	Impedance Bandwidth (%)	Normalized Width (λ_0)
D10L3	0	1.459	7.0	0.22
	5	1.57	13.3	0.24
	10	1.68	34.0	0.25
D25S	0	1.895	4.2	0.16
	5	2.10	9.5	0.18
	10	2.10	40	0.18

Table 4.3 Multi-Segment DRA Broad Band Results

Table 4.4 illustrates the effect of varying the probe length when exciting multi-segment DRAs. A shorter probe lowers the resonant frequency and a longer probe increases the resonant frequency. The values of resonant frequency shown are the widest range of frequencies that could be probe matched for that multi-segment DRA.

DRA	Lower Segment Height (mm)	Probe Length (mm)	Resonant Frequency (GHz)	Impedance Bandwidth (%)
D10L2	0	18	1.394	8.4
	0.9	16	1.456	7.6
	1.8	14	1.492	8.8
		22	1.596	10.2
	2.7	13	1.526	11.0
	3.6	10	1.53	11.6
		15	1.67	12.6
D10L3	0	16	1.459	7.0
	3.6	19	1.75	11.4
		10	1.6	14.4
	7.2	8	1.64	22.0

Table 4.4 Effect of Probe Length on Resonance of Multi-Segment DRA

The radiation pattern of the direct microstrip fed DRA, which has been shown to be a multi-segment DRA, is identical to the pattern of the same DRA on a ground plane excited by a probe, Figure 3.5. The measured cross polarization level was less than -15 dB and the pattern was broad in both planes.

4.6 Comparison of Theoretical and Experimental Results

The resonant frequency predicted by the average value of dielectric constant has a error of within 5% except for the thin lower segments for D25S which have a much larger error, Table 4.5. There was not very good agreement between measured and calculated results for the bandwidth. The probe feed excites a combination of the lower and upper

limit case modes in the multi-segment DRA, but the calculation of the stored versus radiated energy of Section 2.2.3 does not account for the excitation of higher order modes.

DRA	Lower Segment Height (mm)	Resonant Frequency Prediction Error (%)	Ratio of Calculated to Measured Bandwidth
D10L1	0.9	-2.1	0.91
	3.6	+0.3	0.76
D10L3	10	+4.8	0.38
D25S	0.9	+17.1	0.50
	1.65	+17.1	0.48
	5.0	+3.3	0.45

Table 4.5 Prediction Error for Average Dielectric Constant Technique

To characterize the bandwidth improvement to be had with the multi-segment DRA, the DRA standard bandwidth was determined from the measured value of resonance frequency, Table 4.6.

DRA	Lower Segment Height (mm)	DRA Standard		
		Effective Dielectric Constant	Measured Resonant Frequency (GHz)	Calculated Impedance Bandwidth (%)
D10L3	5.0	8.9	1.57	10.5
	10	7.2	1.68	14.7
D25S	1.8	17.0	2.184	4.4
	5	15.8	2.1	5.0
	10	14.0	2.1	6.6

Table 4.6 DRA Standard Using the Measured Value of Resonant Frequency

The multi-segment DRA provides significant increases in bandwidth when compared to the DRA standard. Table 4.7 shows a bandwidth increase of up to 6 times over the standard dielectric resonator antenna.

DRA	Lower Segment Height (mm)	Measured Bandwidth Increase vs Standard DRA
D10L3	5.0	1.27
	10.0	2.3
D25S	1.8	1.56
	5.0	1.89
	10.0	6.3

Table 4.7 Multi-Segment Bandwidth Increase

An interesting result was observed when the probe length for elements D10L2 and D10L3 were varied, see Appendix E. An impedance match to 50 ohm was maintained over a wide range of probe dimensions. The desired resonant frequency occurs for the shortest probe length, since the lower frequency corresponds to the most compact

element. The direct relationship between frequency and probe length means that the impedance match was not being sustained by unwanted probe radiation. The coupling from the probe to the resonant mode of the DRA occurs most strongly where there is a maximum in the electric field. For the TE_{111}^{z} mode this is at edge of the resonator close to the ground plane. For the hybrid mode of the multi-segment DRA, this location is somewhere along the side wall of the resonator. A point further up the wall corresponds to a decrease in the value of k_y and an increase in frequency. Thus the observation of this effect in the multi-segment DRA supports the field structure concept for the multi-segment DRA of Figure 4.4.

Also shown in Appendix E are the return loss plots for D25S with lower segment heights of 5 and 10mm. The concept of an interaction between the limiting case modes can be seen. The two resonances seen for H=5mm are close to the upper and lower limit case resonance frequencies of the D25S DR, shown in Table 4.2. When the lower segment is increased to 10 mm the probe can now excite both modes, resulting in an operational bandwidth of 40%.

4.7 Other Broadband DRA Structures

Several other multi-segment or stacked dielectric resonator antenna structures have been reported. Petosa has reported a multi-segment DRA implemented in conjunction with the direct microstrip feed excitation. In general, lower dielectric constants are used to increase the bandwidth of the DRA but they do not couple well to the direct microstrip feed structure. The thin high dielectric constant layer of the bottom is used to increase the level of coupling to the DRA. This arrangement combines the benefits of the bandwidth advantage of using a low dielectric constant DRA and the simplicity and compactness of the direct microstrip feed excitation structure. However, it appears that to get large increases in bandwidth it is necessary to use a very low dielectric constant segment as demonstrated by Kishk with a bandwidth >25% for the $HEM_{11\delta}$ mode

using stacked cylindrical DRA (Er = 4, 10) and by Shum with a bandwidth of 18% for the $TM_{01\delta}$ mode using stacked annular ring DRA with air gaps between them.

4.8 Practical Usefulness

The multi-segment DRA is a potentially useful compact broadband antenna element. The radiation pattern has a wide beamwidth and impedance bandwidths of up to 40% have been demonstrated. Since it can be square, the two orthogonal modes can be fed separately for polarization diversity or together for circular polarization. The 40% impedance bandwidth was achieved with a multi-segment DRA with a footprint of only $0.18\lambda_0$, a factor of 6 improvement over a standard DRA. Thus it is suitable for use in a planar array implementation such as MSAT which requires closely spaced elements. The radiation pattern variation across the full 40% bandwidth was not experimentally verified. The average value concept predicts resonant frequency for moderate lower segment heights to a similar accuracy as the standard DRA design expressions for regular DRA. Unfortunately, the simple expressions were not able to predict the impedance bandwidth of the multi-segment DRA.

Chapter 5
Novel Edge-Grounded Rectangular DRA

5.1 Introduction

This is believed to be the first reported development of the edge-grounded rectangular dielectric resonator antenna, shown in Figure 5.1 [64]. The resonator wall opposite the probe feed is covered with a conductor, in the case of this investigation the conductor is a piece of copper tape. The conductor is electrically grounded at the plane of intersection between the dielectric wall and the ground plane that the DRA is resting on.

The edge-grounded DRA was developed in an attempt to improve the bandwidth to size ratio of the multi-segment DRA. The presentation of the research into the edge-grounded DRA is separated into two parts. In the first section, the edge-grounded DRA under consideration has a homogeneous dielectric and the expressions developed for the calculation of resonant frequency and bandwidth in Chapter 2 are modified to accurately predict the performance of the new structure.

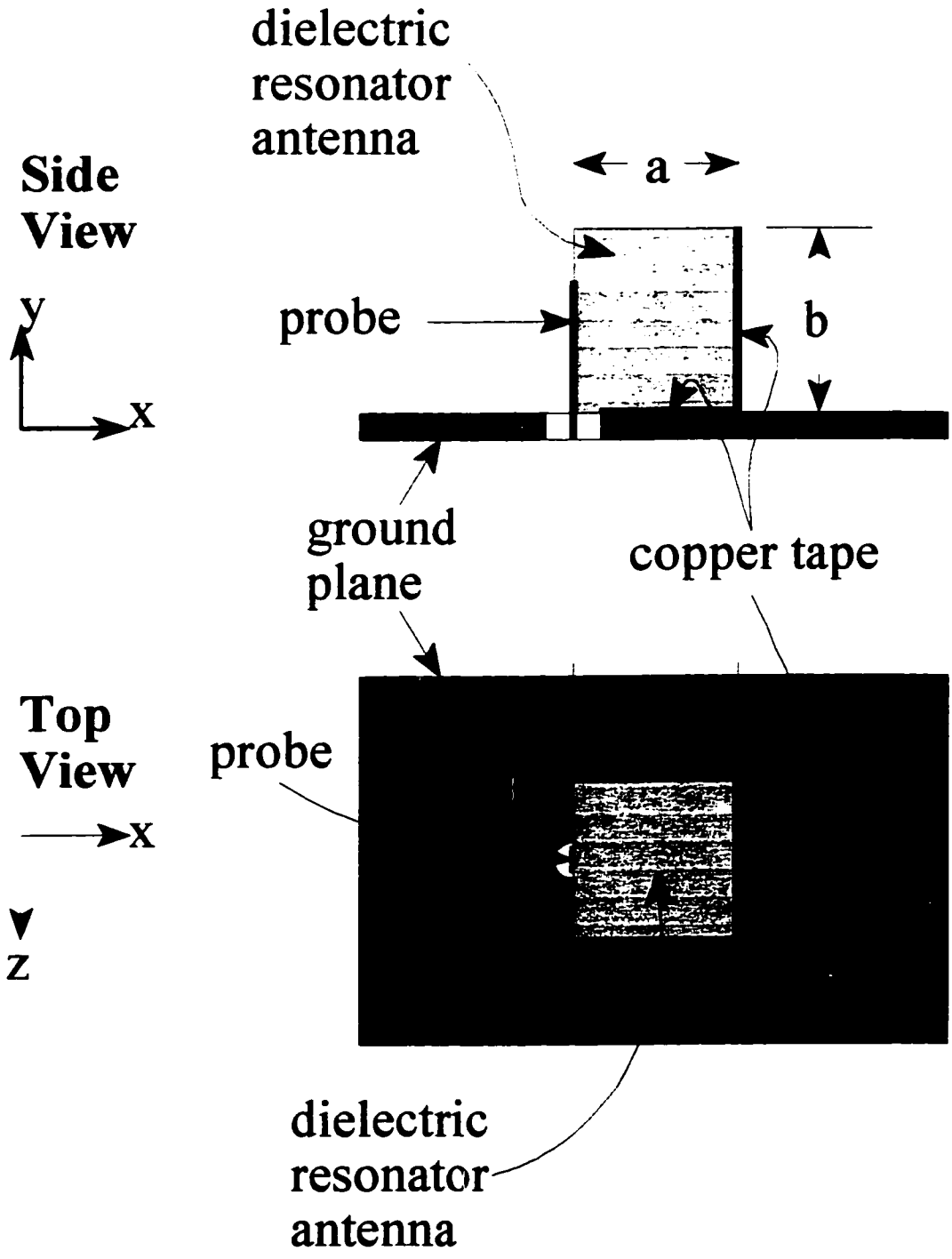

Figure 5.1
Dimensions of Rectangular Edge-grounded DRA and Probe Feed

In the second part, the edge-grounded technique will be applied to the broad band multi-segment DRA. The bandwidth performance of the edge-grounded multi-segment DRA will be shown to be almost as good as for the multi-segment DRA which is twice as large. The approximate analysis of the multi-segment DRA of Chapter 4 will be combined with the accurate theory of the homogeneous edge-grounded DRA to predict the resonant frequency of this new structure. The experimental results for several very compact broad band linearly polarized rectangular dielectric resonator antennas will be presented.

5.2 Homogeneous DRA

5.2.1 Resonant Frequency

The edge-grounded homogeneous DRA can be viewed as a full DRA excited in the TE_{111}^{z} mode which has been truncated at x=0 by a perfect electrical conductor, Figure 5.2. The electric and magnetic fields derived in Chapter 2 reduce to Equations 5.1 in the YZ-plane defined by x=0.

$$\begin{aligned} E_x &= j\omega\mu_0 \frac{k_y}{k_x^2 + k_y^2} A \sin(k_y y)\cos(k_z z) \\ E_y &= 0 \\ E_z &= 0 \\ H_x &= 0 \\ H_y &= \frac{k_y k_z}{k_x^2 + k_y^2} A \sin(k_y y)\sin(k_z z) \\ H_z &= A\cos(k_y y)\cos(k_z z) \end{aligned} \tag{5.1}$$

If Equations 5.1 satisfy the boundary conditions for a perfect electric conductor at the YZ-plane defined by x=0, then the edge-grounded DRA is analogous to the regular rectangular DRA and the theory developed for the lowest order resonant mode can be applied to this new structure.

$$\begin{aligned} \boldsymbol{n} \times \boldsymbol{E} &= 0 \\ \boldsymbol{H} \cdot \boldsymbol{n} &= 0 \end{aligned} \tag{5.2}$$

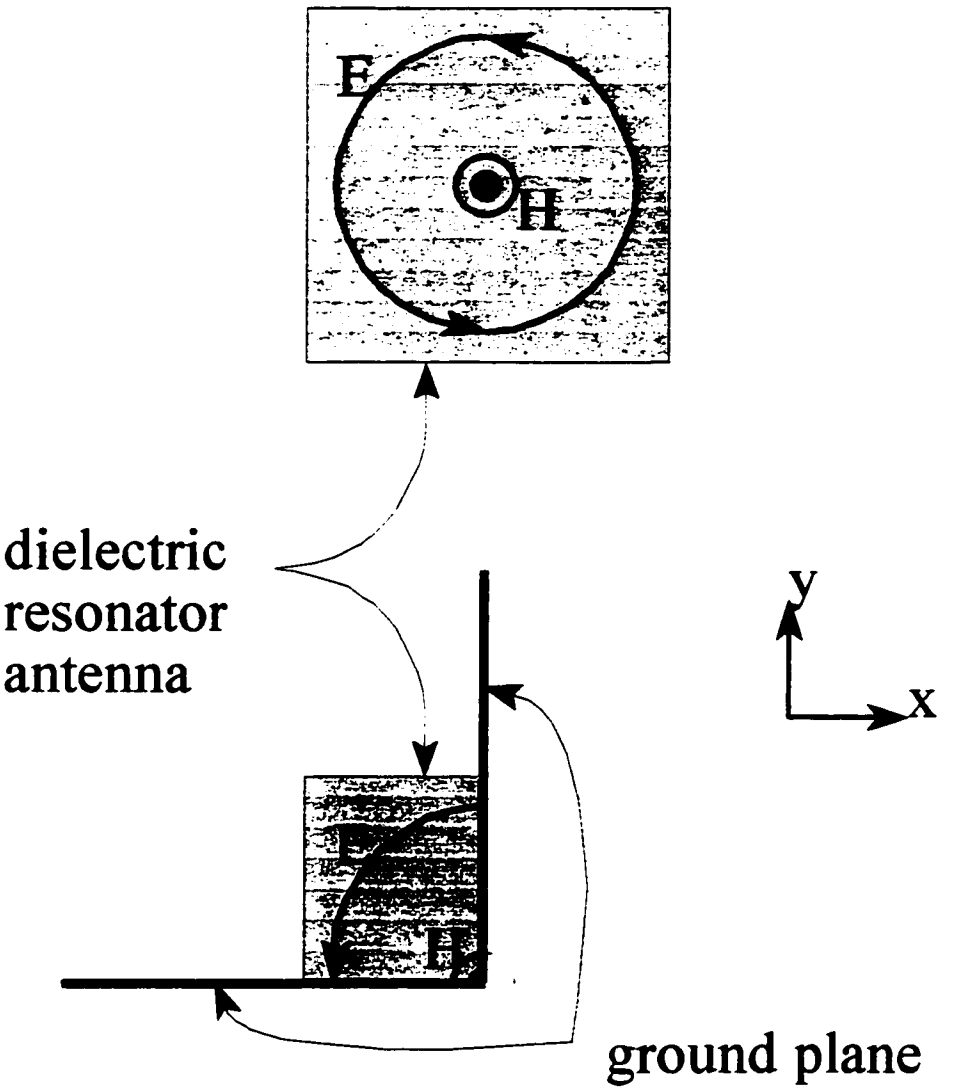

Figure 5.2
Orientation of Transverse Electric Field for Lowest Order Mode

For the geometry of Figure 5.1, the normal to the surface is represented by $\mathbf{a}_x$. Substituting the expressions for the electric and magnetic fields of the $TE_{111}{}^z$ mode into Equations 5.2 yields :

$$\begin{aligned} \boldsymbol{a}_x \times (E_x,\ 0,\ 0) &= 0 \\ (0,\ H_y,\ H_z) \cdot \boldsymbol{a}_x &= 0 \end{aligned} \qquad \textbf{(5.3)}$$

Equations 5.3 show that the substitution of a perfect electric conductor at x=0 does not affect the internal field structure of the $TE_{111}{}^z$ mode of rectangular DRA. Thus the new edge-grounded DRA structure, Figure 5.1, with dimensions (a x 2d x b) can be analysed using the techniques developed in Section 2.2.1 for a DRA with dimensions (2a x 2d x b). The resonant frequency of the edge-grounded DRA is then calculated exactly as in Equations 2.17. Due to the labelling convention of Figure 5.1, the width of the regular DRA is denoted as '2a' and the width of the edge-grounded DRA as 'a'. So the expression for the wave number, Equation 2.8, used in the calculation of the resonant frequency remains $k_x = \pi/2a$.

The actual implementation of the PEC at x=0 as a piece of copper tape on the side wall of the DRA will introduce some error into the model. However, the fields are strongest inside the DRA so the copper tape will appear as a grounded PEC to the majority of the resonant field structure.

For a particular DRA core, the resonant frequency will be reduced for the edge-grounded DRA. Conversely, for a particular resonant frequency the edge-grounded DRA will be half the size of an equivalent full size DRA.

5.2.2 Impedance Bandwidth

The conductive surface covering the side of the DRA is not an infinite ground plane, so the edge-grounded DRA cannot use the isolated DRA model to predict bandwidth. The fields inside the DRA are assumed to be the same as those determined for the TE_{111}^{z} mode of the regular isolated DRA. However, the edge-grounded side is not an infinite ground plane so the radiated power from the DRA would be different from the regular DRA. The structure of Figure 5.2 is equivalent to the edge-grounded rectangular DRA on a ground plane. The technique presented in Section 2.2.2 for determining the radiation Q-factor and hence the impedance bandwidth of the isolated regular DRA can be applied to the edge-grounded structure of Figure 5.2 assuming an internal field structure given by Equation 2.17.

The modal wave numbers k_x, k_y, and k_z are determined the as before by Equations 2.8 and 2.10. The volume occupied by the resonator is now :

$$\begin{aligned} -a < x < 0 \\ -b < y < b \\ -d < z < d \end{aligned} \qquad \textbf{(5.4)}$$

Since we know that the edge-grounded DRA also radiates like a magnetic dipole, the magnetic dipole moment can be determined as in Section 2.2.2. The homogeneous dielectric resonator radiates like a volume electric current as before, and for simplicity radiation from the metal edge is ignored.

$$
\begin{aligned}
\boldsymbol{p}_{m_{EG}} &= \frac{1}{2}\int \boldsymbol{R}\times\boldsymbol{J}_p\,dV \\
&= \frac{-\omega^2\mu_0\epsilon_0(\epsilon_r-1)A}{2(k_x^{\,2}+k_y^{\,2})}\iiint z k_x \sin(k_x x)\cos(k_y y)\cos(k_z z)\,\boldsymbol{a}_x \\
&\qquad + z k_y \cos(k_x x)\sin(k_y y)\cos(k_z z)\,\boldsymbol{a}_y \\
&\qquad - x k_x \sin(k_x x)\cos(k_y y)\cos(k_z z) \\
&\qquad - y k_y \cos(k_x x)\sin(k_y y)\cos(k_z z)\,\boldsymbol{a}_z \; dx\,dy\,dz \qquad \textbf{(5.5)} \\
&= \frac{\omega^2\mu_0\epsilon_0(\epsilon_r-1)A}{2(k_x^{\,2}+k_y^{\,2})}\left[\ \frac{8\sin(k_z d)}{k_x k_y k_z}\boldsymbol{a}_z\ \right] \\
\boldsymbol{p}_{m_{EG}} &= \frac{\boldsymbol{p}_{m_{full}}}{2}
\end{aligned}
$$

Thus the magnetic dipole moment of the edge-grounded DRA (a x 2d x 2b) is equal to half the magnetic dipole moment of the regular full size DRA (2a x 2d x 2b). The stored energy for the edge-grounded DRA is calculated from the electric field in the DRA as in Section 2.2.2. By inspection it can be seen that the energy stored in the edge-grounded DRA (a x 2d x 2b) is half that for the equivalent regular DRA of dimension (2a x 2d x 2b).

$$
(W_e)_{EG} = \frac{(W_e)_{full}}{2} \qquad \textbf{(5.6)}
$$

So the ratio of the bandwidth of the edge-grounded DRA to the equivalent full size DRA is given by :

$$BW_{EG} = \frac{P_{rad}}{2\omega W_e}$$
$$= \frac{10k_0^4 |\frac{p_{m_{full}}}{2}|^2}{2\omega \frac{W_{e_{full}}}{2}} \quad (5.7)$$
$$= \frac{BW_{full}}{2}$$

The resonant frequency and bandwidth of the edge-grounded DRA are predicted to be half the values calculated using Equations 2.30 for an equivalent DRA twice the width of the edge-grounded DRA. In Table 5.1 the predicted resonant frequency and bandwidth are given for three measured edge-grounded DRA. Using the theoretical value of resonant frequency, the theoretical bandwidth of the edge-grounded DRA is approximately 9% greater than the bandwidth of the DRA standard. Based on the comparison with the DRA standard, the theoretical analysis of the edge-grounded DRA predicts the new structure does not provide a more compact or broader band element than a regular DRA, but approximately the same performance.

DRA	Equivalent Width = 2a		DRA Standard (Width = a)		
	Resonant Frequency (GHz)	Impedance Bandwidth (%)	Effective Dielectric Constant	Resonant Frequency (GHz)	Impedance Bandwidth (%)
D12H	1.4	3.65	25.0	1.4	3.2
D25M	1.33	1.4	41.5	1.33	1.3
D25S	1.59	1.6	36.1	1.59	1.5

Table 5.1 Edge-Grounded DRA Theoretical Values

5.2.3 Experimental Results

Several of the dielectric resonator antennas from Section 3.1, with dielectric constants ranging from 10 to 40 and various aspect ratios, were implemented as edge-grounded DRA, Table 5.2. Both the resonant frequency and impedance bandwidth were reduced for the edge-grounded DRA when compared to core DRA measured in Chapter 3, Table 3.1. It was not necessary to completely cover the end of the DRA with a conductor to achieve the edge-grounded effect. The use of a grounded probe no larger than the feed probe was sufficient to achieve the same result or reduction in resonant frequency and bandwidth.

.

DRA	Resonant Frequency (GHz)	Impedance Bandwidth (%)
D12H	1.24	5.6
D25M	1.34	1.5
D25S	1.335	1.9

Table 5.2 Edge-grounded DRA Measurements

The radiation pattern for a probe fed rectangular edge-grounded DRA is similar to the broad beamwidth pattern of the regular rectangular DRA. The radiation pattern for an edge-grounded DRA with the grounded edge covering only the centre third of the side of the DRA had the same broad beam shape, but with an increased cross polarization level of -10 dB, Appendix F.

5.2.4 Comparison of Measurement and Theory

The measured resonant frequency and impedance bandwidth agreed with the values predicted from the theoretical treatment of Section 5.2. The resonant frequency prediction was within 16 % and the average bandwidth error was 25% which is close slightly more than that for the regular DRA, but acceptable considering the approximate

nature of the analysis.

DRA	Equivalent Width = 2a		Effective Dielectric Constant for Width = a
	Resonant Frequency Prediction Error (%)	Ratio of Calculated to Measured Bandwidth	Measured Bandwidth Increase vs DRA Standard
D12H	-12.9	0.65	1.75
D25M	-0.8	0.93	1.15
D25S	+16	0.84	1.27
Average	9.9	0.81	1.35

Table 5.3 Prediction Error for Edge-Grounded DRA Theory

The measured bandwidth of the edge-grounded DRA was on average 25% larger than the predicted bandwidth and 35% greater than the bandwidth calculated using the effective dielectric constant. The ratio of the measured bandwidth to the standard value is slightly larger than the typical bandwidth error prediction for the rectangular DRA, and so it appears that the bandwidth of the edge-grounded DRA may be slightly larger than that of a regular DRA of the same size. Thus the edge-grounded technique does miniaturize the DRA somewhat.

5.2.5 Practical Usefulness

In terms of meeting the requirements for broad band compact antenna elements, the edge-grounded DRA structure does not significantly improve upon the results achievable with a regular DRA. The technique could be useful if a particular larger value of dielectric constant was not available to produce a more compact antenna. The increased bandwidth of the edge-grounded structure is only slightly more than the typical prediction error and in general does not justify the increase in complexity of implementation. Far greater improvements can be achieved through selection of an

appropriate DRA geometry, Section 2.5. The advantage of the edge-grounded structure is most significant when combined with the multi-segment structure.

5.3 Multi-Segment DRA

5.3.1 Introduction

The multi-segment edge-grounded rectangular dielectric resonator antenna is shown in Figure 5.3. As the name implies, the two previously described variations on the rectangular DRA are combined in a novel manner to form a compact broadband antenna element. The multi-segment edge-grounded DRA were probe fed and had low dielectric constant lower segments and higher dielectric constant upper segments. The edge of both segments of the DRA opposite the probe feed were completely covered with a piece of copper tape. The tape was electrically connected to the aluminum surface used as the ground plane, Figure 5.3.

In general, applying the edge-grounded technique to a DRA results in an antenna that is much smaller, but with an equal narrowing of the bandwidth of operation of the DRA. With the multi-segment DRA of Chapter 4, the frequency separation of the limit cases appeared to contribute to the very broad band nature of the DRA with thicker lower segments. If the frequency separation difference between the limit cases is a more important contributor to the bandwidth of the multi-segment resonator than the bandwidth of the limit cases, then the edge-grounded multi-segment element should have an equally broad bandwidth as the multi-segment, but at half the size.

5.3.2 Theoretical Analysis

The edge-grounded technique was able to be implemented on a regular rectangular DRA because the field structure at the YZ-plane satisfied the conditions for a perfect electric conductor. The exact expressions for the electric and magnetic fields internal to the multi-segment DRA were not determined. However, the approximate nature of these

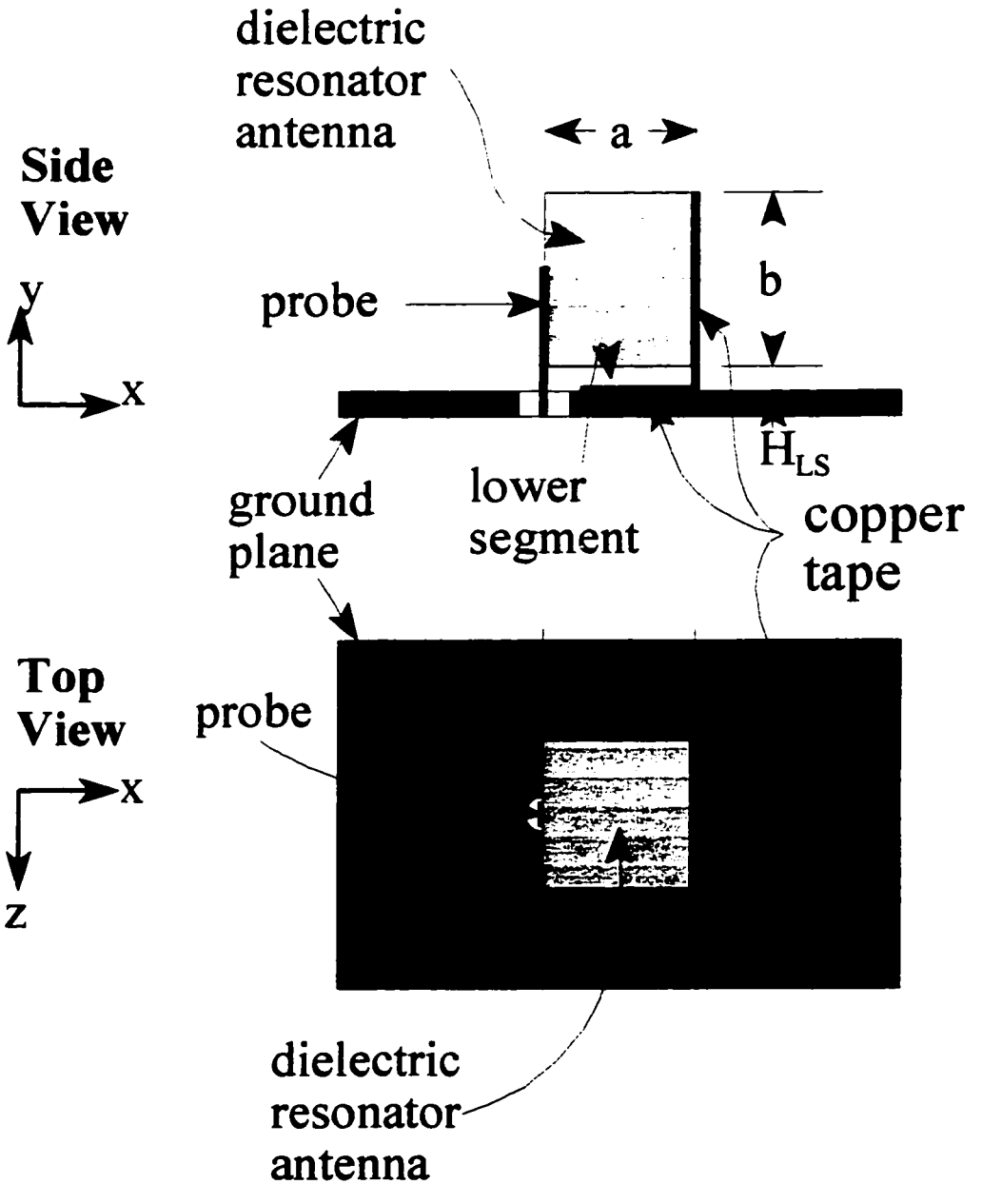

Figure 5.3
Dimensions of Rectangular Edge-grounded Multi-segment DRA and Probe Feed

fields was described in Section 4.4 and illustrated in Figures 4.3 and 4.4. The field components have the same ($k_x x$) dependence as the $TE_{111}{}^z$ mode so the magnetic wall boundary condition at |x|=a is satisfied. Thus the internal fields of the multi-segment DRA in the YZ-plane have the same form as in Equations 5.1, although the ($k_y y$) and ($k_z z$) dependencies will differ. Therefore, at x=0 the internal fields of the multi-segment resonator satisfy Equations 5.2, the boundary conditions for a PEC, see Figure 5.4.

Applying the same theory developed for the analysis of the edge-grounded DRA to the multi-segment structure allows for the calculation of the limiting frequencies for the new structure. The extreme cases representing a lower segment height of zero and infinity are given by the edge-grounded homogeneous DRA on a ground plane and the edge-grounded homogeneous DRA of the same dimensions in free space, Table 5.4. The limit cases of edge-grounded DRA are modelled using the equivalent width = 2a. The resonant frequency is expected to lie between these extremes.

DRA	H_{LS} (mm)	Limit $H_{LS} = 0$		Limit $H_{LS} = \infty$	
		f_{res} (GHz)	BW (%)	f_{res} (GHz)	BW (%)
D10L3	10	1.26	10.4	2.09	18.7
D25S	5	1.59	3.2	2.725	6.8

Table 5.4 Multi-Segment Edge-Grounded DRA Limiting Resonances

The average value of dielectric constant of the multi-segment DRA is used in conjunction with the equivalent width = 2a edge-grounded model to predict the resonant frequency of the multi-segment edge-grounded DRA, Table 5.5.

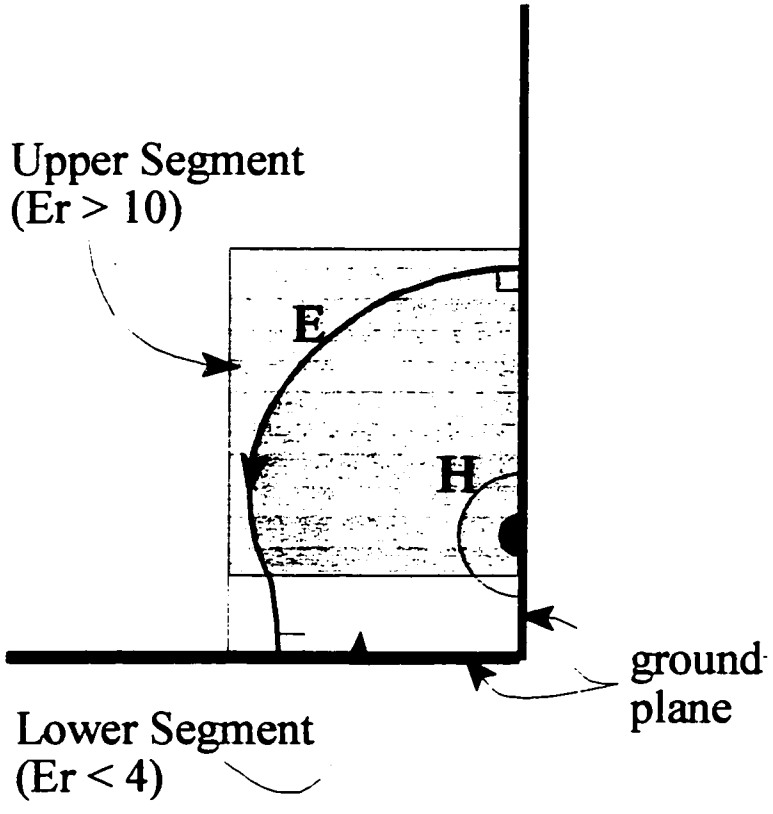

Figure 5.4
Conceptual Orientation of Transverse Electric Field for
Edge-grounded Multi-segment DRA

DRA	Lower Segment Height (mm)	Average Dielectric Constant	Resonant Frequency (GHz)	Impedance Bandwidth (%)
D10L3	10	8.0	1.17	12.0
D25S	5	17.0	1.56	4.8

Table 5.5 Resonant Frequency Prediction for Multi-Segment Edge-Grounded DRA

The radiation pattern of the edge-grounded multi-segment DRA is expected to have the same broad pattern as did the regular, the edge-grounded, and the multi-segment DRA.

5.3.3 Experimental Results

The measurement results for two multi-segment edge-grounded DRA are shown in Table 5.6. The measured impedance bandwidths are nearly as broad as for the multi-segment DRA, but the normalized width is much smaller. From the graph of Figure 2.7 for regular square planform DRA, $0.19\lambda_0$ is located near the minimum bandwidth value for most dielectric constants. A width of $0.12\lambda_0$ is not even an achievable dimension except for dielectric constants of greater than 40.

DRA	Lower Segment Height (mm)	Resonant Frequency (GHz)	Impedance Bandwidth (%)	Normalized Width
D10L3	10	1.274	30	$0.19\ \lambda_0$
D25S	5	1.365	7.3	$0.12\ \lambda_0$

Table 5.6 Multi-Segment Edge-Grounded DRA Measurements

5.3.4 Comparison of Theoretical and Experimental Results

The measured resonant frequency of D10L3 was shown to lie between the limit cases of a lower segment of very small and very large height, however this was not the case for the D25S where the estimated lower resonance frequency was much too high. The radiation pattern has the same typical DRA broad pattern at boresight.

The average value of dielectric constant applied with the edge-grounded reduction in resonant frequency prediction technique results in an average accuracy of 11.3% in predicting the resonant frequency of the combination DRA, Table 5.7. The combination of the multi-segment and edge-grounded techniques is a useful estimation tool for the resonant frequency.

DRA	Lower Segment Height (mm)	Resonant Frequency Prediction Error (%)	Ratio of Calculated to Measured Bandwidth
D10L3	10	+8.2	0.4
D25S	5	-14.3	0.66

Table 5.7 Prediction Error : Multi-Segment Edge-Grounded DRA

The bandwidth of the DRA standard using the measured resonance frequency of the multi-segment edge-grounded DRA are shown in Table 5.8.

DRA	Lower Segment Height (mm)	Effective Dielectric Constant	Resonant Frequency (GHz)	Impedance Bandwidth (%)
D10L3	10	12.6	1.274	7.2
D25S	5	37.5	1.37	1.5

Table 5.8 Bandwidth of DRA Standard

The multi-segment edge-grounded DRA increased the element impedance bandwidth by 4.5 times the DRA standard. That was twice the increase for the same geometry of multi-segment DRA, see Table 5.9 and Table 4.7 respectively.

DRA	Lower Segment Height (mm)	Measured Bandwidth Increase vs DRA Standard
D10L3	10	4.2
D25S	5	4.8

Table 5.9 Multi-Segment Edge-Grounded DRA Bandwidth Increase

The edge-grounded multi-segment DRA is the most compact of the broadband DRA investigated in this thesis. Results for regular (Table 3.3), multi-segment (Table 4.3), edge-grounded (Table 5.2) and edge-grounded multi-segment (Table 5.6) DRA based on the D25S segment have been reported. Comparison of the measured values of impedance bandwidth with the bandwidth standard presented in Section 4.2 shows the edge-grounded multi-segment DRA to have the broadest bandwidth relative to its size and resonant frequency. While the edge-grounded DRA is strictly the smallest relative to resonant frequency, it is presumed that use of higher dielectric constant materials in the edge-grounded multi-segment DRA could yield a more compact DRA with a broader bandwidth, based on the results of comparison with the DRA bandwidth standard in Tables 5.3 and 5.9 respectively.

5.3.5 Practical Usefulness

The edge-grounded multi-segment dielectric resonator antenna presented here is a more compact broadband antenna that any previously reported DRA configuration. Unfortunately, the asymmetry of this antenna means that it can excite only a single linear polarization. The size of this DRA, $0.12\lambda_0$ for BW=7%, is such that a 2-dimensional planar array with interelement spacing of $0.25\lambda_0$ could be implemented, allowing

beamscanning to cover a complete hemisphere. The advantages of this novel configuration are wide impedance bandwidth, compact size and broad beamwidth. No simple expression for predicting impedance bandwidth was found. The resonant frequency prediction is less accurate than the design relation for a regular DRA, but close enough to get the designer to the point of starting experimentation or a numerical simulation.

Chapter 6

Conclusions and Recommendations

6.1 General

The motivation behind this research initially was to investigate the feasibility of using rectangular dielectric resonator antennas in L-Band applications. While it was demonstrated that the performance of individual DRA was sufficient, the true test of the applicability of this technology to a particular application is to fabricate a complete antenna unit and compare it to existing solutions.

Research should add to the fundamental knowledge of the field, generate useful analytic and design techniques, and provide practical experience to the researcher. These criteria were successfully achieved. Practical experience was gained through extensive testing of the antennas on a Wiltron 360 Network Analyser, and in an anechoic chamber using a Flam & Russell automated antenna measured system, at the Communications Research Centre. As a result of this testing, several previously reported design techniques including the DRA modelled as a dielectric waveguide with mixed magnetic walls, a

radiation pattern prediction tool based on the internal mode structure of the DRA, and a design procedure for a circularly polarized rectangular DRA were experimentally verified. Independent verification of research adds to the general knowledge base of the field. Finally, resonant frequency and bandwidth predictors were developed for the modified rectangular DRA structures.

Thus this thesis meets the general objectives of research work as spelled out above.

6.2 Objectives Accomplished

The specific objectives of the experimental and theoretical portions of this research were also met.

6.2.1 Experimental

A primary focus of the experimental work was to verify published results for a broad selection of rectangular dielectric resonator antenna implementations, thereby confirming the reproducibility and reliability of DRA technology. Probe, aperture, and direct coupling to many rectangular DRA of various aspect ratios and dielectric constants was observed. Radiation patterns, resonant frequencies and impedance bandwidths of the DRA were measured. The circular polarization design procedure of Oliver was implemented and experimentally verified.

The other objective of this thesis was to characterize the performance of novel rectangular DRA modified for compactness and increased bandwidth. The performance of the novel broad band elements exceeded expectations. Some results, edge-grounded in particular, agreed well with theory. The increased bandwidth results for the multi-segment DRA were not predicted, however the results are now available for comparison with future analytic work.

6.2.2 Analytical

The existing theory of a dielectric waveguide with mixed magnetic walls was the basis of the analytical treatment of the rectangular DRA in this thesis. As was previously demonstrated, it was used to predict resonant frequency and impedance bandwidth for the linear lowest order mode of the rectangular DRA, and compared against measurement. Existing DRA design techniques also based on this theory including rectangular circularly polarized DRA design procedure and the prediction of the radiation pattern, from the internal mode structure, were implemented and verified. The resonant frequency and bandwidth predictors were applied to previously reported results on the triangular DRA, with good agreement.

Predictors for the resonant frequency and impedance bandwidth of the modified rectangular DRAs were developed, based on the mode structure described by the DWM with IMW theory and the simple predictors for regular DRA. The analytic treatment of the modified DRA was very approximate and did not predict many of the experimentally observed results. However, the attempt to extend the simple model for regular DRA to the describe the modified DRA permitted an intuitive understanding of the behaviour of the antennas. Finally, a standard procedure was proposed for the comparison of the relative performance benefits of the modifications techniques to the rectangular DRA.

6.3 Significance of This Work

The important contributions of this work to the field of dielectric resonator antenna research are :

a. Verification of the single feed rectangular circularly polarized DRA of Oliver, both the design methodology and the broadband experimental results.
b. Novel theoretical and experimental work on the edge-grounded DRA.
c. Experimental measurement of the most compact broad band DRA element

reported in literature.

d. Development of a standard for comparison of bandwidth enhancement techniques for DRA.

6.4 Future Work

As the field of rectangular DRA technology is mostly still in the experimental stage, there are many possible areas of further inquiry. Some topics of relevance to this thesis are :

Analytical

a. The development of a theory to predict the broadband behaviour of the multi-segment DRA.

b. The use of numerical modelling techniques to gain insight into the field structure of the edge-grounded and multi-segment geometries.

c. The further development of analytic expressions to better predict the resonance of rectangular DRA.

d. The development of analytic expressions for the determination of input impedance for rectangular DRA fed by a variety of coupling structures.

Experimental

a. The measurement of radiation patterns for a range of edge-grounded multi-segment DRA across the full bandwidth to verify that other modes are not being excited. This should be undertaken at a higher frequency so the geometry of the test apparatus does not impact the results.

b. Characterization of multi-segment structures with more than two segments, and with higher dielectric constants on the lower segment so that aperture and direct coupling can be implemented.

References

1. M. G. Douglas, et al. "A Planar Diversity Antenna for Hand-Held PCS Devices". **ANTEM 96 Conf Proc**, 1996, pp 447-450.

2. GANDEC Systems Inc. **Microplanar PCS Basestation Antennas**, April 1997.

3. Private Communication with Microcell Technology Inc.

4. P.C. Strickland. "Planar Arrays for MSAT and INMARSAT Land Mobile Satellite Communications", **IEEE AP Society International Symposium**, 1995, pp 1388-1391.

5. S.A. Long, L.C. Shen, P.B. Morel. "Theory of the Circular Disc Printed Circuit Antenna", Proc Int of Elec Eng, Vol 125, 1978, pp 925-928.

6. A.A. Kishk, M.R. Zunoubi, D. Kajfez. "A Numerical Study of Dielectric Disk Antenna Above Grounded Dielectric Substrate". IEEE Trans on Ant and Prop, **Vol AP-41**, June 1993, pp 813-821.

7. M. Sawamura, M. Tabata, M. Haneishi. "Radiation Properties of Ring Microstrip Antenna Fed by Symmetrical Cross Slot", **IEEE AP Society International Symposium**, 1995, pp 2074-2077.

8. F. Rostan, W Wiesbeck. "Design Considerations for Dual Polarized Aperture-Coupled Microstrip Patch Antenna", **IEEE AP Society International Symposium Digest**, 1995, pp 2086-2089.

9. H. Iwasaki. "A Circularly Polarized Rectangular Microstrip Antenna Using Single-Fed Proximity-Coupled Method", IEEE Trans. Ant. Prop., Vol **AP-43**, 1995, pp 895-897.

10. R. Telikepalli. "A Comparison Between Stacked Slotted and Solid Square Patches in Phased Array Environment for Wide Angle Coverage", **IEEE AP Society International Symposium, 1995**, pp 930-933.

11. J. Huang, A. Densmore. "Microstrip Yagi Antenna for Mobile Satellite Service", **IEEE AP-S Digest**, 1991, pp. 616-619.

12. R.D. Richtmeyer. "Dielectric Resonator", Journal of Applied Physics, **Vol 10**, June 1939, pp 391-398.

13. A. Okaya & L.F. Barash. "The Dielectric Microwave Resonator", Proc IRE, Vol 50, October 1962, pp 2081-2092.

14. Trans-Tech, "A Designer's Guide to Microwave Dielectric Ceramics", Trans - Tech Publication 50080040 Rev. 3, April 1993.

15. S.B. Cohn. "Microwave Bandpass Filters Containing High-Q Dielectric Resonators", IEEE Trans. On Microwave Theory and Techniques, Vol MTT-16, April 1968, pp 218-227.

16. H.Y. Yee, "Natural Resonant Frequencies of Microwave Dielectric Resonators", IEEE Trans on Microwave Theory and Tech, Vol MTT-13, March 1965, pp 256.

17. A. Karp, H. Shaw & D.K. Winslow. "Circuit Properties of Microwave Dielectric Resonators", IEEE Trans on Microwave Theory and Techniques, Vol MTT-16, October 1968, pp 818-828.

18. J. Van Bladel. "On the Resonances of a Dielectric Resonator of Very High Permittivity", IEEE Trans on Microwave Theory and Techniques, Vol MTT-23, February 1975, pp 199-208.

19. J. Van Bladel. "The Excitation of Resonators of Very High Permittivity", IEEE Trans on Microwave Theory and Techniques, Vol MTT-23, February 1975, pp 208-217.

20. E.A.J. Marcatili. "Dielectric Resonator Waveguide and Directional Coupler for Integrated Optics", **Bell System Technical Journal**, Sept 1969, pp 2071-2102.

21. P. Guillon & Y. Garault, "Accurate Resonant Frequencies of Dielectric Resonators", IEEE Trans on Microwave Theory and Tech, Vol MTT-25, November 1977, pp 916-922.

    P. Guillon & Y. Garault, "Correction to Accurate Resonant Frequencies of Dielectric Resonators", IEEE Trans on Microwave Theory and Tech, Vol MTT-28, November 1980, pp 434.

22. J.F. Legier, et al. "Resonant Frequencies of Rectangular Dielectric Resonators", IEEE Trans on Microwave Theory and Tech, **Vol MTT-28**, September 1980, pp 1031-1034.

23. R.K. Mongia. "Half-Split Dielectric Resonator Placed on a Metallic Plane for Antenna Applications", Electronic Letters, **Vol EL-25**, March 1989, pp 462-464.

24. D. Kajfez & P. Guillon (Editors). Dielectric Resonators, Artech House, 1986.

25. M.T. Birand & R.V. Gelsthorpe, "Experimental Millimetric Array Using Dielectric Resonators Fed by Means of Dielectric Waveguide", Electronics Letters, Vol 17, Sept 1981, pp 633-635.

26. S.A. Long, M.W. McAllister, W.M. Chen. "The Resonant Cylindrical Dielectric Cavity Antenna", IEEE Trans on Ant and Prop, Vol AP-31, May 1983, pp 406-412.

27. M. McAllister, S.A. Long, G.L. Conway. "Rectangular Dielectric Resonator Antennas". Electronic Letters, **EL-19**, March 1983, pp 219-220.

28. R.A. Kranenburg, S.A. Long. "Microstrip Transmission Line Excitation of Dielectric Resonator Antennas", Electronic Letters, **Vol EL-24**, Sept 1988, pp 1156-1157.

29. J.T.H. St-Martin, et al. "Dielectric Resonator Antenna Using Aperture Coupling", Electronic Letters, **Vol El-26**, Oct 1990, pp 2015-2016.

30. R.A. Kranenburg, S.A. Long, J.T. Williams. "Coplanar Waveguide Excitation of Dielectric Resonator Antennas", IEEE Trans on Ant and Prop, **Vol AP-39**, 1991, pp 119-122.

31. A. Ittipiboon, et al. "Aperture Fed Rectangular and Triangular Dielectric Resonators for use as Magnetic Dipole Antennas". IEE Electronics Letters, **EL-29**, September 1993.

32. K.W. Leung, et al. "Input Impedance of Aperture Coupled Hemispherical Dielectric Resonator Antenna", Electronics Letters, 1993, **Vol EL-29**, pp 1165-1166.

33. A.A. Kishk, B. Ahn, D. Kajfez. "Broadband Stacked Dielectric Resonator Antennas". Electronic Letters, 1989, **EL-25**, pp 1232-1233.

34. R.N. Simons, R.Q. Lee. "Effect of Parasitic Dielectric Resonators on CPW/Aperture Coupled Dielectric Resonator Antennas", IEEE Proc-H, Vol 140, Oct 1991, pp 336-338.

35. S.M. Shum, K.M. Luk. "Stacked Annular Ring Dielectric Resonator Antenna

Excited by Axi-Symmetric Coaxial Probe". IEEE Trans. Ant. Prop., **Vol AP-43**, 1995, pp 889-892.

36. R. K. Mongia, P. Bhartia. "Dielectric Resonator Antennas - A Review and General Design Relations for Resonant Frequency and Bandwidth", **Int. Journal of Microwaves and Millimetre-Wave Computer-Aided Engineering**, Vol 4, No. 3, pp 230-247, 1994.

37. R.K. Mongia, et al. "A Half Split Cylindrical Dielectric Resonator Antennas Using Slot Coupling", IEEE Trans on Microwave Theory and Tech, **Vol MTT-3**, 1993, pp 38-39.

38. R.K. Mongia, et al. "Electric-Monopole Antenna Using a Dielectric Ring Resonator", IEE Electronics Letters, **EL-29**, 1993, pp 1530-1531.

39. R.K. Mongia, et al. "Measurement of Radiation Efficiency of Dielectric Resonator Antennas". **IEEE Microwave and Guided Wave Letters**, 1994, Vol. 4, No. 3, pp 80-82.

40. R. K. Mongia, et al. "Low Profile Dielectric Resonator Antennas Using a Very High Permittivity Material". IEE Electronics Letters, 1994, **EL-30**, pp 1362-1363.

41. R. K. Mongia, et al. "Magnetic Quadrupole Mode Dielectric Resonator Antenna", **Conference Proceedings IEEE Antennas and Propagation**, 1995, pp 734-737.

42. A. Petosa, et al. "A Novel Microstrip-Fed Multi-Segment Dielectric Resonator Antenna", **ANTEM 1996 Conf. Proc.**, pp 705-708.

43. M. Haneishi, H. Takazawa. "Broadband Circularly Polarized Planar Array Composed of a Pair of Dielectric Resonator Antennas", Electronics Letters, **Vol EL-21**, May 1985, pp 437-438.

44. R.K. Mongia, et al. "Circularly Polarised Dielectric Resonator Antenna". IEE Electronics Letters, 1994, **EL-30**, pp 1361-1362.

45. A. Ittipiboon, et al. "A CP Dielectric Guide Antenna with a Single Slot Feed", **1994 ANTEM Conf. Proc.**, pp 427-430.

46. M. B. Oliver, et al. "A New Broadband Circularly Polarized Dielectric Resonator Antenna". **IEEE Proceedings Antennas and Propagation Conference**, 1995, pp 738-741.

47. A. Petosa, et al. "Investigation of Various Feed Structures for Linear Arrays of Dielectric Resonator Antennas". **IEEE Proceedings Antennas and Propagation Symposium Digest**, 1995, pp 1982-1985.

48. R.K. Mongia, A. Ittipiboon, M. Cuhaci. "Experimental Investigations on Microstrip-Fed Series Dielectric Resonator Antenna Arrays", **ANTEM Conf Proc**, 1994, pp 81-83.

49. A. Petosa, et al. "Design of Microstrip-fed series array of dielectric resonator antennas", IEE Electronic Letters, **Vol 31**, No 16, August 1995, pp 1306-1307.

50. G. D. Loos. Thesis : **Investigation of a Novel Aperture-Coupled Rectangular Dielectric Resonator Antenna Array**, Royal Military College of Canada, 1994.

51. A.A. Kishk, H.A Auda, B. Ahn. "Accurate Predictions of Radiation Patterns of Dielectric Resonator Antennas". Electronic Letters, 1987, **EL-23**, pp 1374-1375.

52. K.W.Leung, et al. "Theory and Experiment of Coaxial Probe Fed Hemispherical Dielectric Resonator Antenna", IEEE Trans on Ant and Prop, 1993, **Vol AP-41**, pp 1390-1398.

53. K.W.Leung, K.M. Luk. "Moment Method Solution of Aperture Coupled Hemispherical Dielectric Resonator Antenna", **Conf Proc AP & S International Symposium**, 1994, pp 752-755.

54. S.M. Shum, K.M. Luk. "Analysis of Aperture Coupled Rectangular Dielectric Resonator Antenna". Electronic Letters., **Vol EL-30**, 1994, pp 1726-1727.

55. A. Dhouib, et al. "TLM Analysis of Rectangular Dielectric Resonator Antennas". **Conference Proceedings IEEE Antennas and Propagation**, 1995, pp 782-785.

56. J. Carrie, et al. "A Ka-Band Circularly Polarized Dielectric Resonator Modelled Using the Transmission-Line-Matrix Method". **ANTEM 1996 Conf. Proc.**, pp 709-712.

57. D. Faggetter, Y.L. Chow. "A Simple Moment Method for a Dielectric Resonator in Free Space". **ANTEM 1996 Conf. Proc.**, pp 789-792.

58. C.A. Balanis. **Advanced Engineering Electromagnetics**. John Wiley & Sons, 1989.

59. R.K. Mongia, et al. "Radiation Q-Factor of Rectangular Dielectric Resonator Antenna, Theory and Experiment", Conference Proceedings IEEE AP & S

International Symposium, 1994, pp 764-767.

60. C.A. Balanis. **Antenna Theory: Analysis and Design**, John Wiley & Sons, 1982.

61. R. K. Mongia. **Theoretical and Experimental Investigations on Dielectric Resonator Antennas.** Communications Research Centre, 1994.

62. M.B. Oliver. Thesis : **Circularly Polarized Rectangular Dielectric Resonator Antenna using a Single Feed**, Royal Military College of Canada, 1995.

63. T.K. Sarkar, E. Arras, S. Ponnapalli. "Electromagnetic Scattering from Dielectric Bodies", IEEE Trans on Ant and Prop, **Vol AP-37**, May 1989, pp 673-676.

64. M. Cooper, et al. "Investigation of Dielectric Resonator Antennas for L-Band Communications", **ANTEM 1996 Conf. Proc.**, pp 167-170.

Appendix A
Direct Microstrip Feed Measurements

A.1 Network Analyser Measurements Showing Weak Coupling for Direct Microstrip Fed D25M and D40H DRA

A.2 Libra Simulation of Broad Band Performance of Direct Microstrip Fed D25M DRA Using Measured Results of A.1

A.3 Radiation Pattern Measurements of the Direct Microstrip Fed D25M DRA Showing Horizontal Dipole Mode Pattern

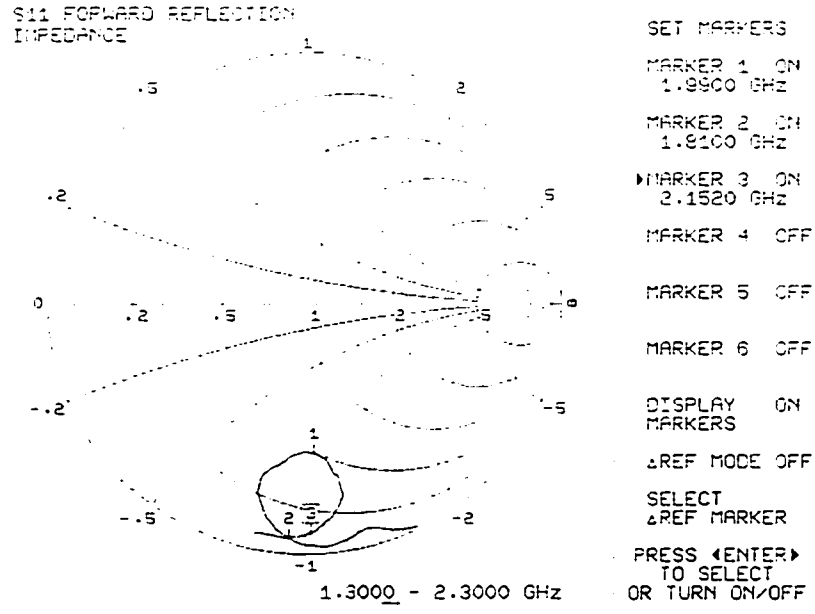

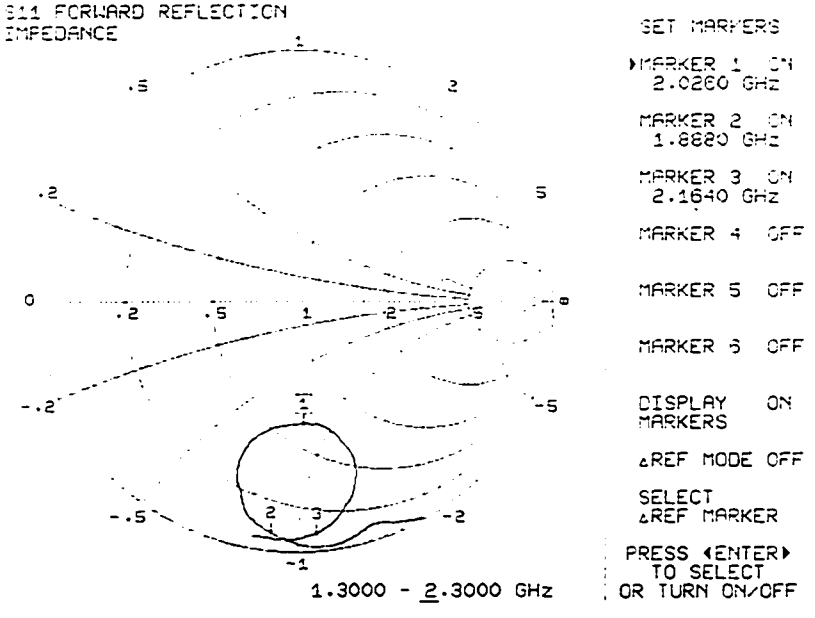

A.1 Network Analyser Measurements Showing Weak Coupling for Direct Microstrip Fed D25M (Top) and D40H (Bottom) DRA

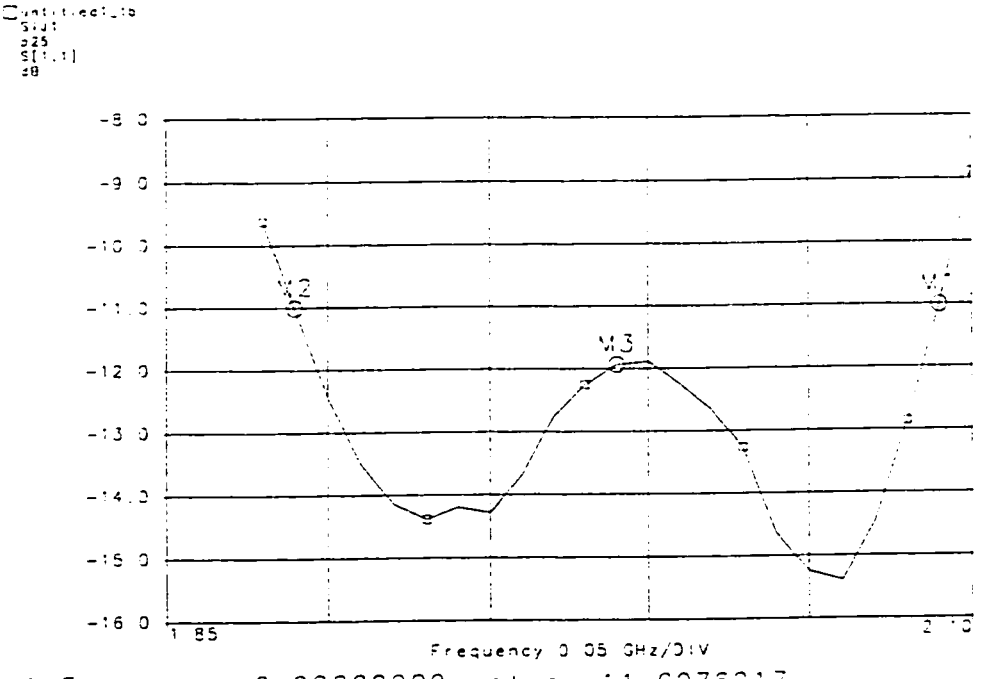

M1 Frequency=2.09000000 value=-11.0076217
M2 Frequency=1.89000000 value=-11.0076631
M3 Frequency=1.99000000 value=-11.9335853

A.2 Libra Simulation of Broad Band Performance of Direct Microstrip Fed D25M DRA Using Measured Results of A.1

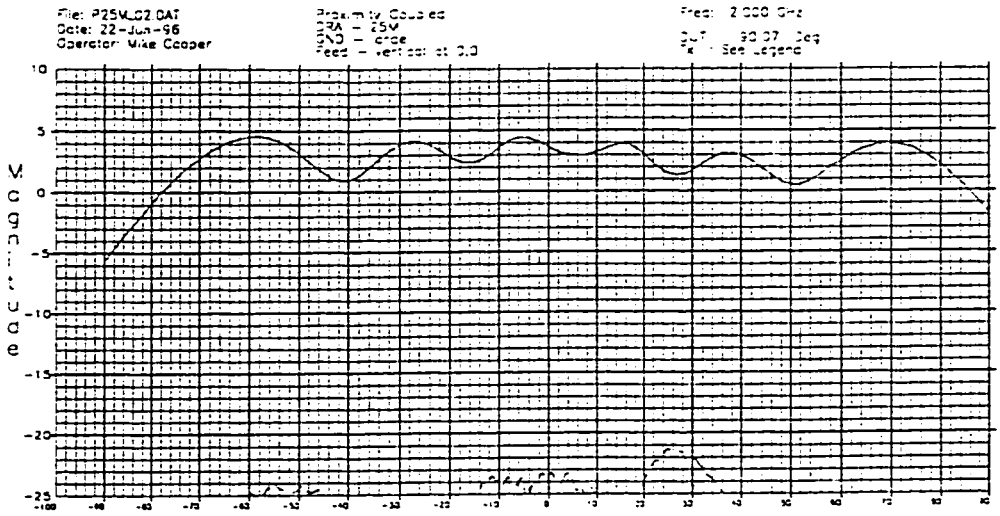

Radiation Pattern : E-Plane

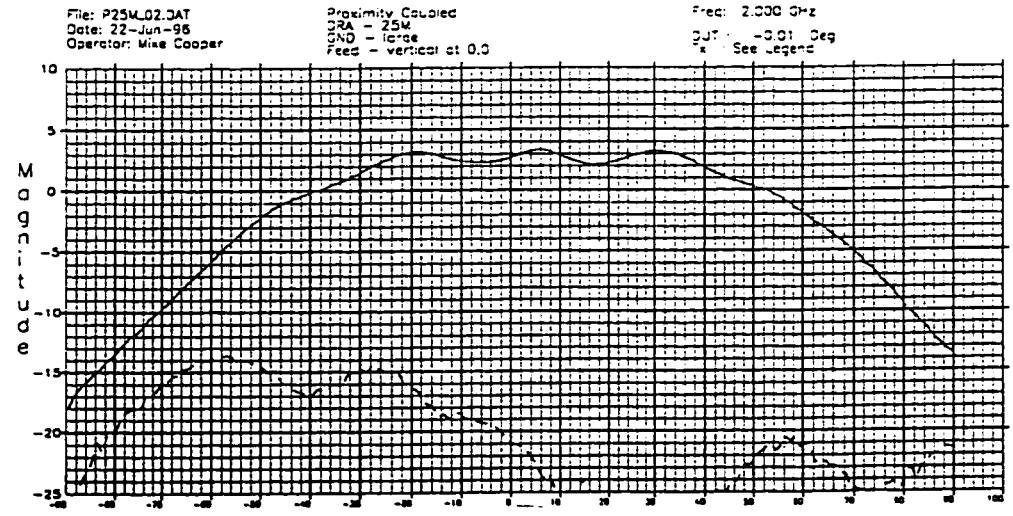

Radiation Pattern : H-Plane

A.3 Radiation Pattern Measurements of the Direct Microstrip Fed D25M DRA Showing Horizontal Dipole Mode Pattern

Appendix B
Linear Pattern Simulation vs Measurement

B.1 Measured E- and H-Plane Radiation Patterns for D40L1 DRA

B.2 Simulated E- and H-Plane Radiation Patterns for D40L1 DRA

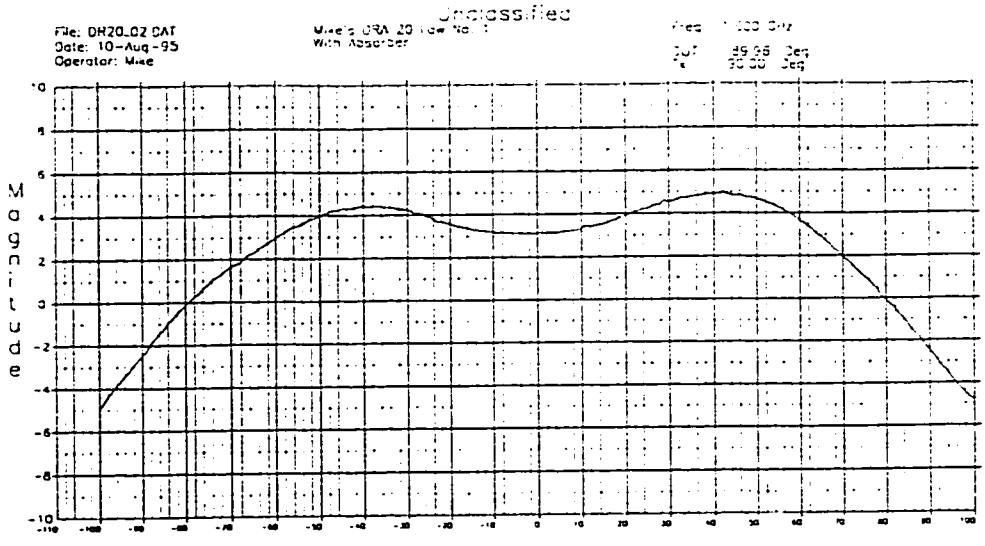

Radiation Pattern : E-Plane

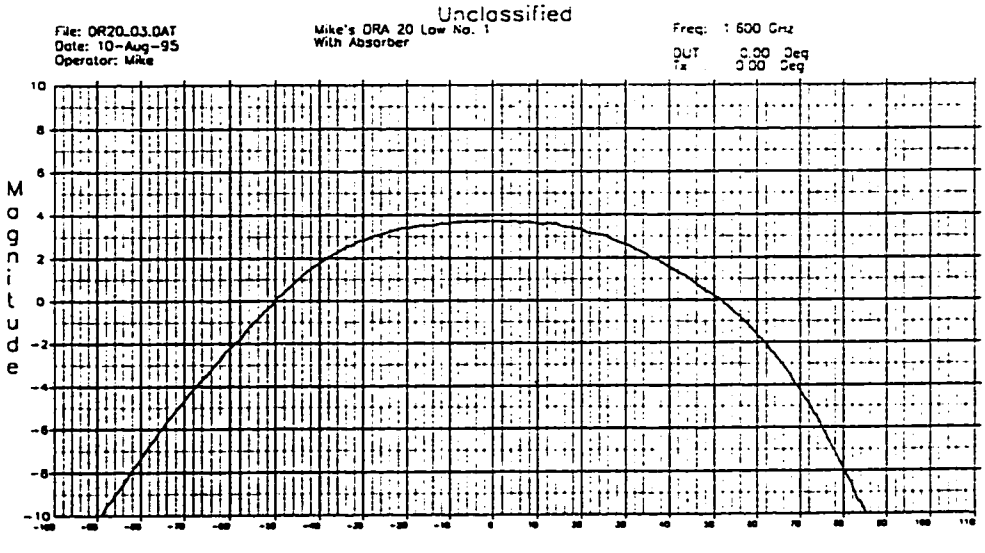

Radiation Pattern : H-Plane

B.1 Measured E- and H-Plane Radiation Patterns for D40L1 DRA

(Note Small Ground Plane Used)

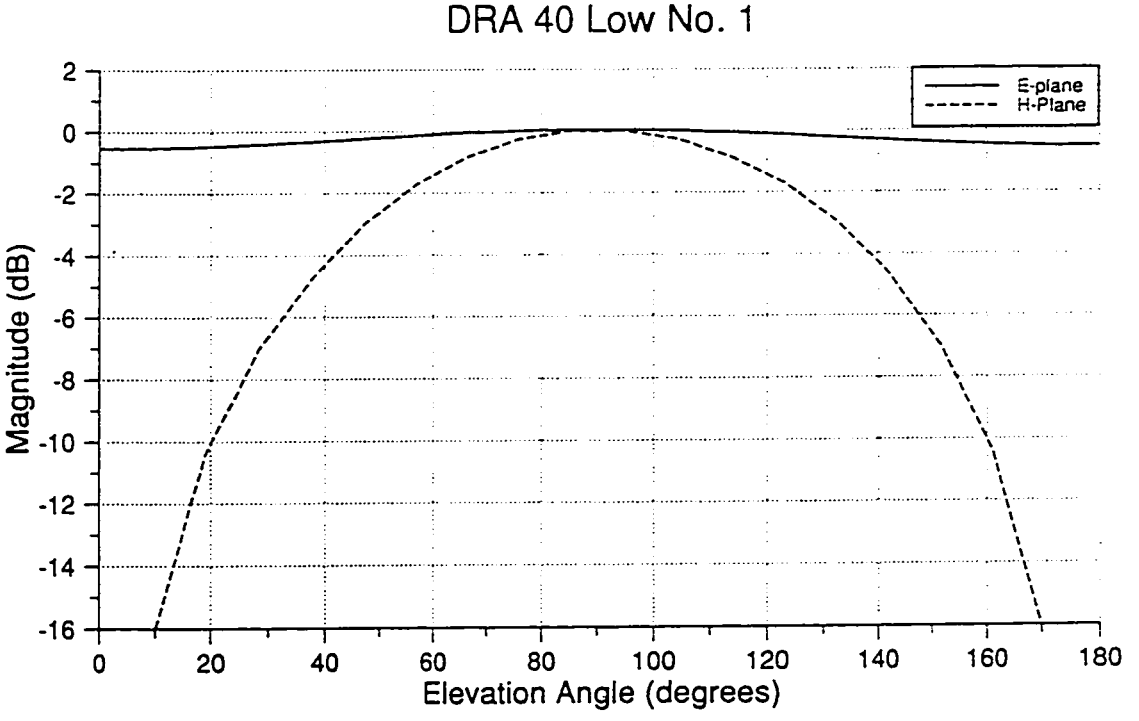

B.2 Simulated E- and H-Plane Radiation Patterns for D40L1 DRA

Appendix C
Dual Polarization Isolation Measurements

C.1 Network Analyser Measurement of Input Match and Port to Port Isolation for Dual Linear Fed D25H DRA

C.2 Network Analyser Measurement of Input Match and Port to Port Isolation for Dual Linear Fed D40H DRA

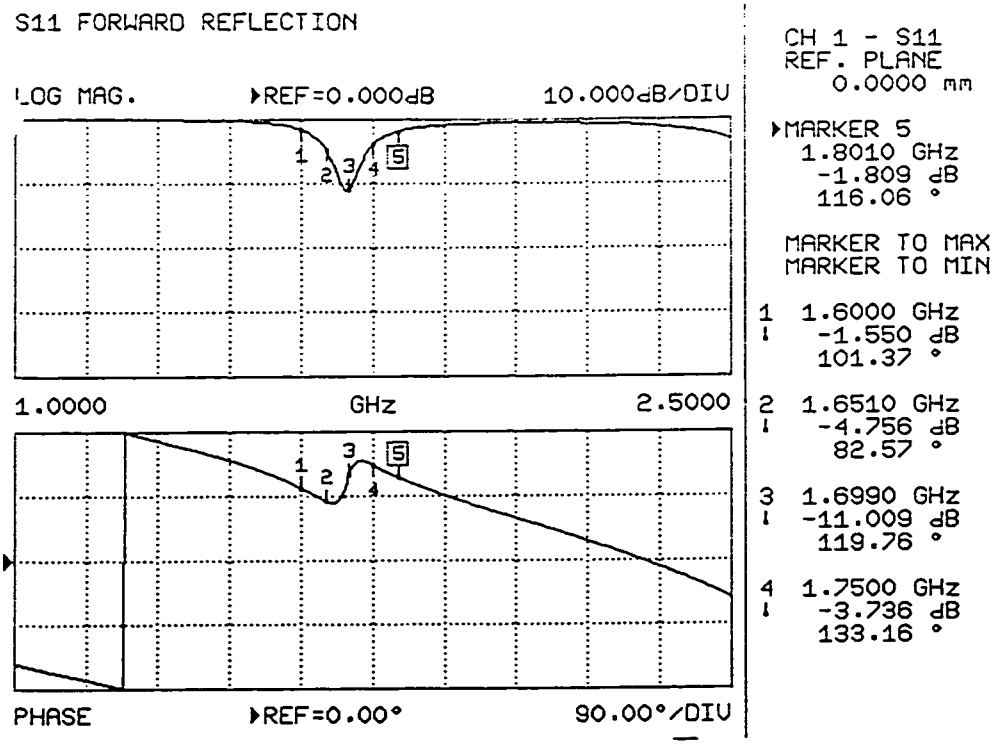

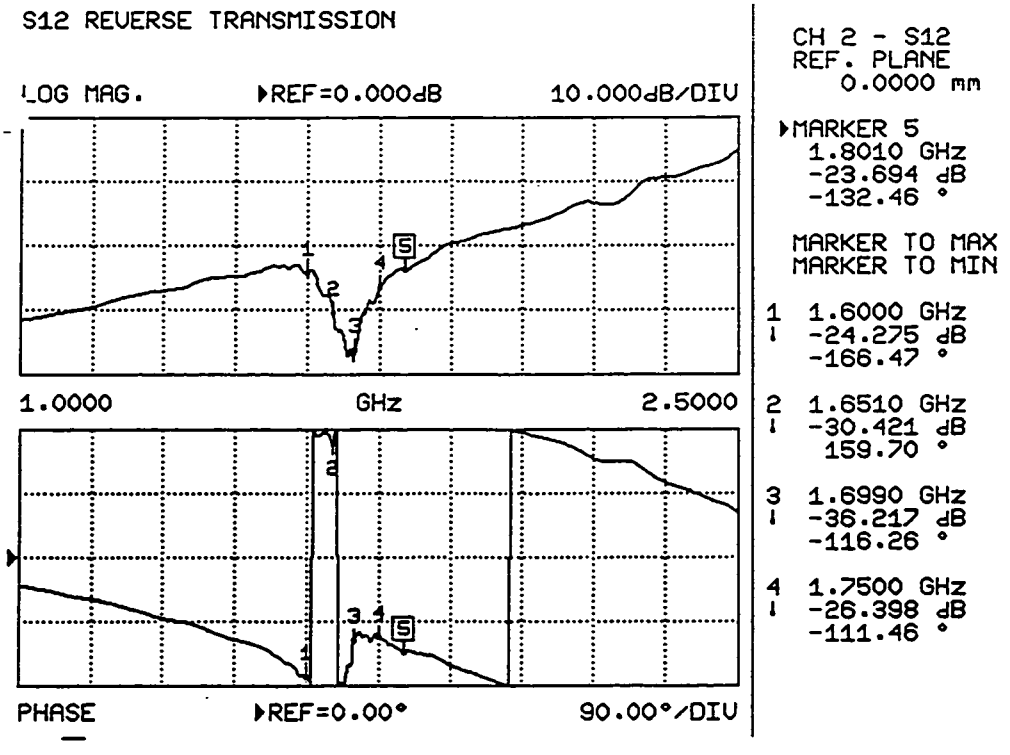

C.1 Network Analyser Measurement of Input Match and Port to Port Isolation for Dual Linear Fed D25H DRA

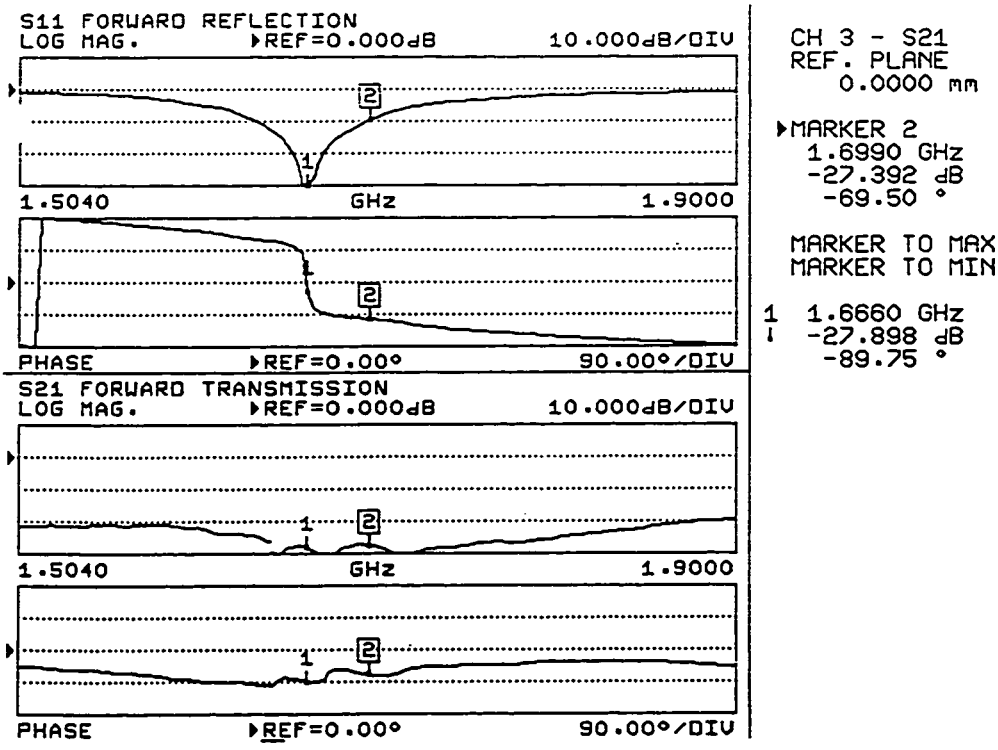

C.2 Network Analyser Measurement of Input Match and Port to Port Isolation for Dual Linear Fed D40H DRA

Appendix D
Rectangular Circularly Polarized DRA Measurements

D.1 Measurement of CP20 DRA Showing Resonant Frequency and Phasing of Linear Modes

D.2 Network Analyser Measurement of CP resonance of CP20 DRA, and Sample Radiation Pattern

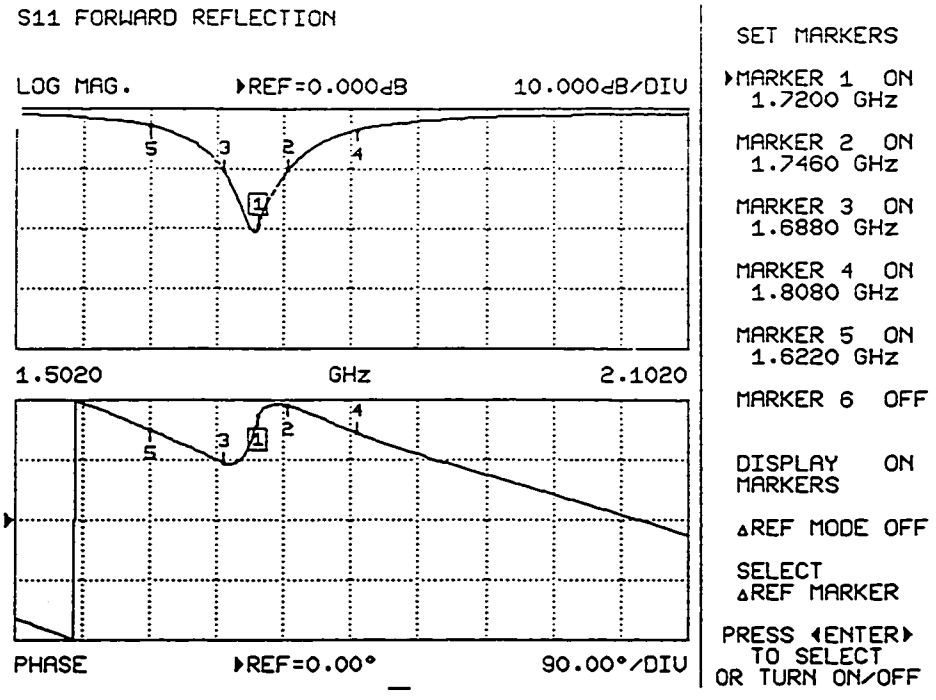

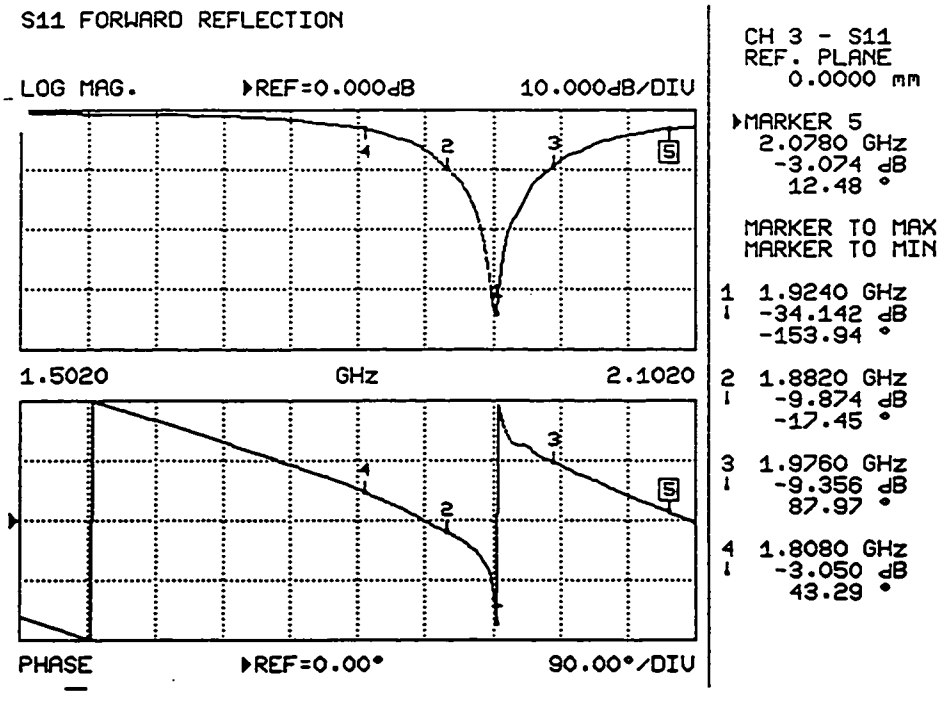

D.1 Measurement of CP20 DRA Showing Resonant Frequency and Phasing of Linear Modes

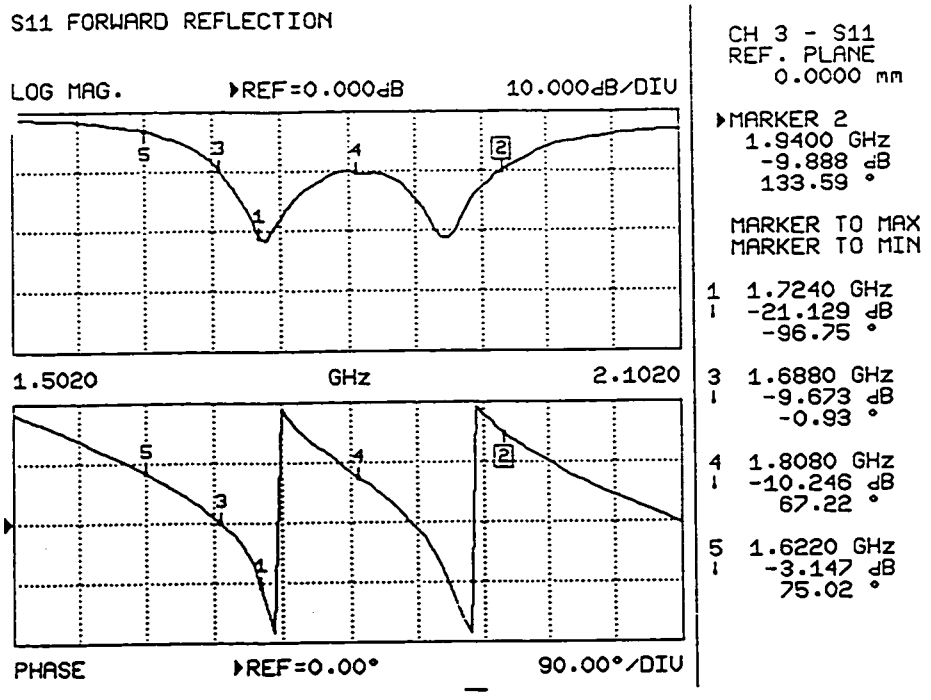

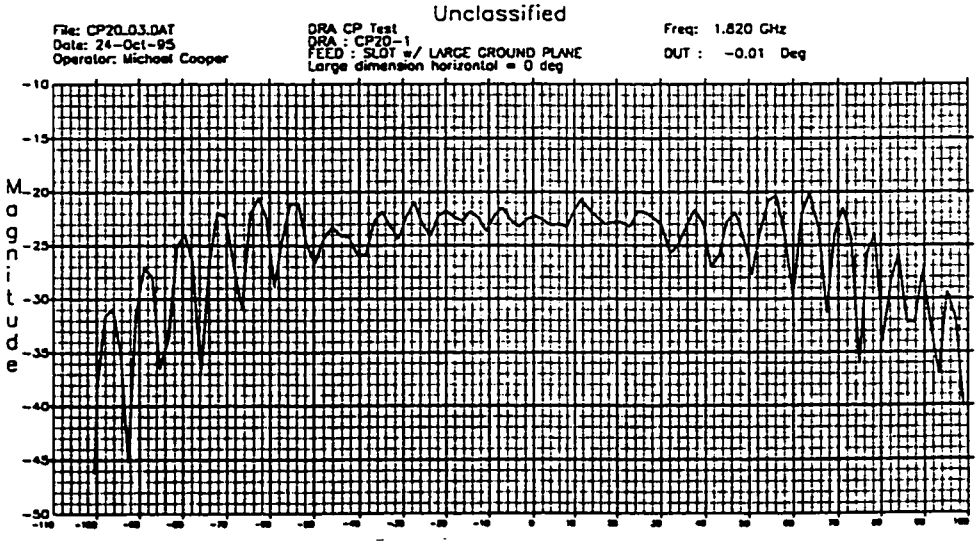

Elevation Radiation Pattern

D.2 Network Analyser Measurement of CP resonance of CP20 DRA, and Sample Radiation Pattern

Appendix E
Multi-Segment Rectangular DRA Network Analyser Measurements

E.1 Broad Band Measurement of Multi-Segment DRA Based on D10L3 Segment

E.2 Frequency Shift with Probe Length for Multi-Segment DRA Based on D10L3 Segment

E.3 Broad Band Measurement of Multi-Segment DRA Based on D25M with Limiting Mode Resonances Visible

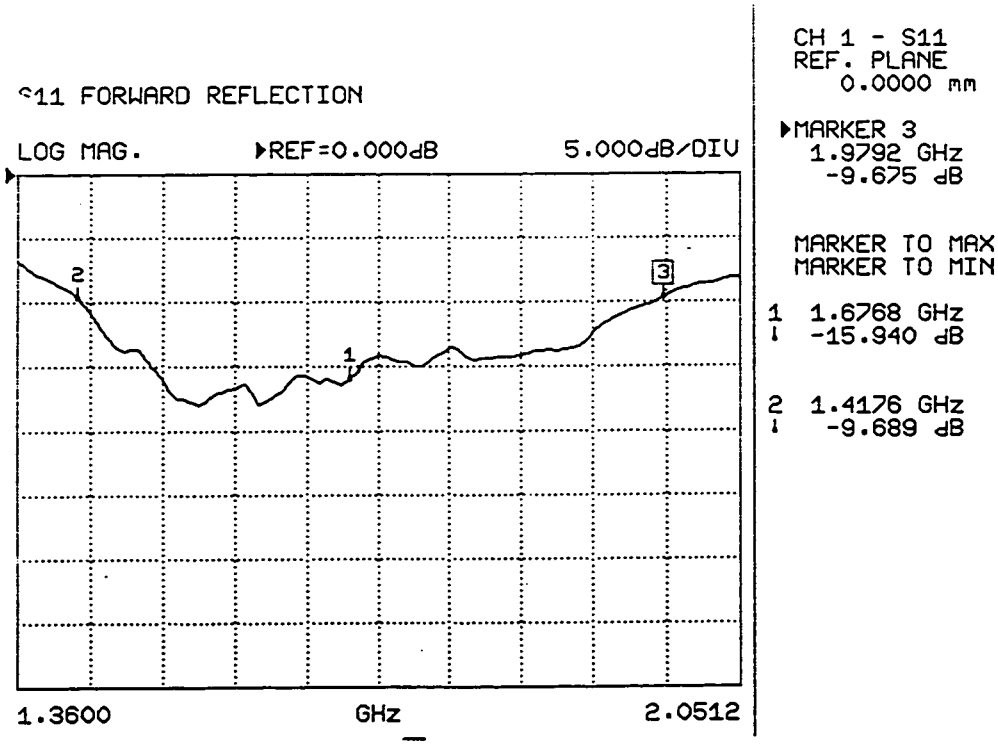

E.1 Broad Band Measurement of Multi-Segment DRA Based on D10L3 Segment

Lower Segment Height = 1.0 cm, Dielectric Constant = 4.0

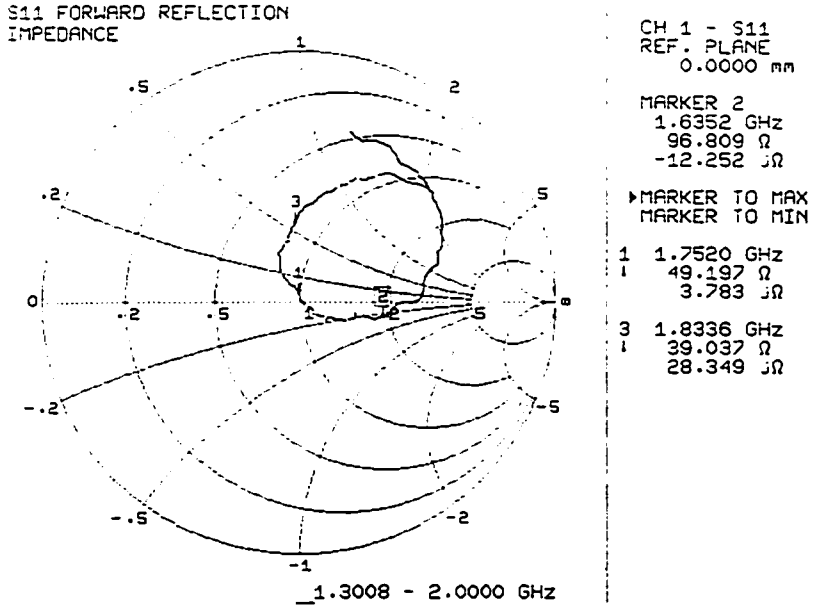

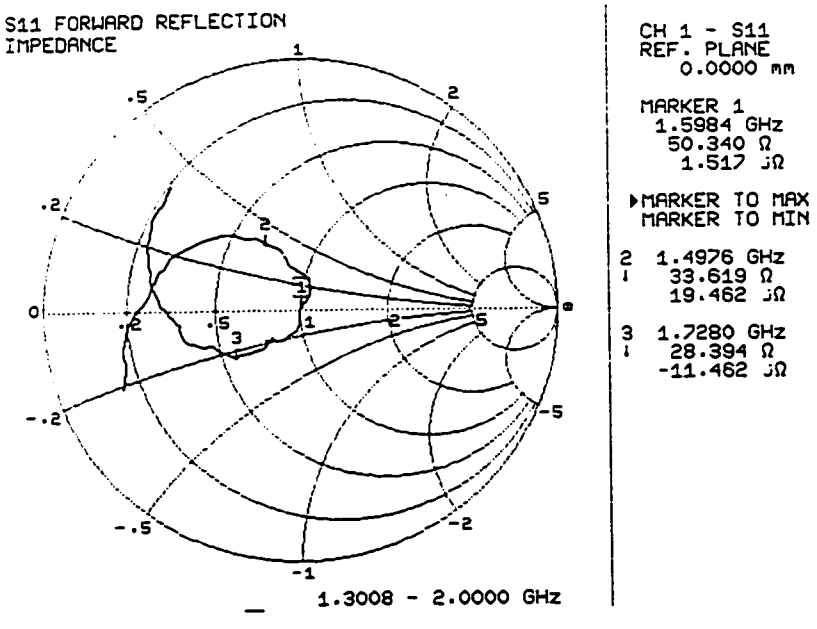

E.2 Frequency Shift with Probe Length for Multi-Segment DRA

Based on D10L3 Segment

Lower Segment Height = 0.4 cm, Probe Length = 1.9 cm (Top), 1.0 cm (Bottom)

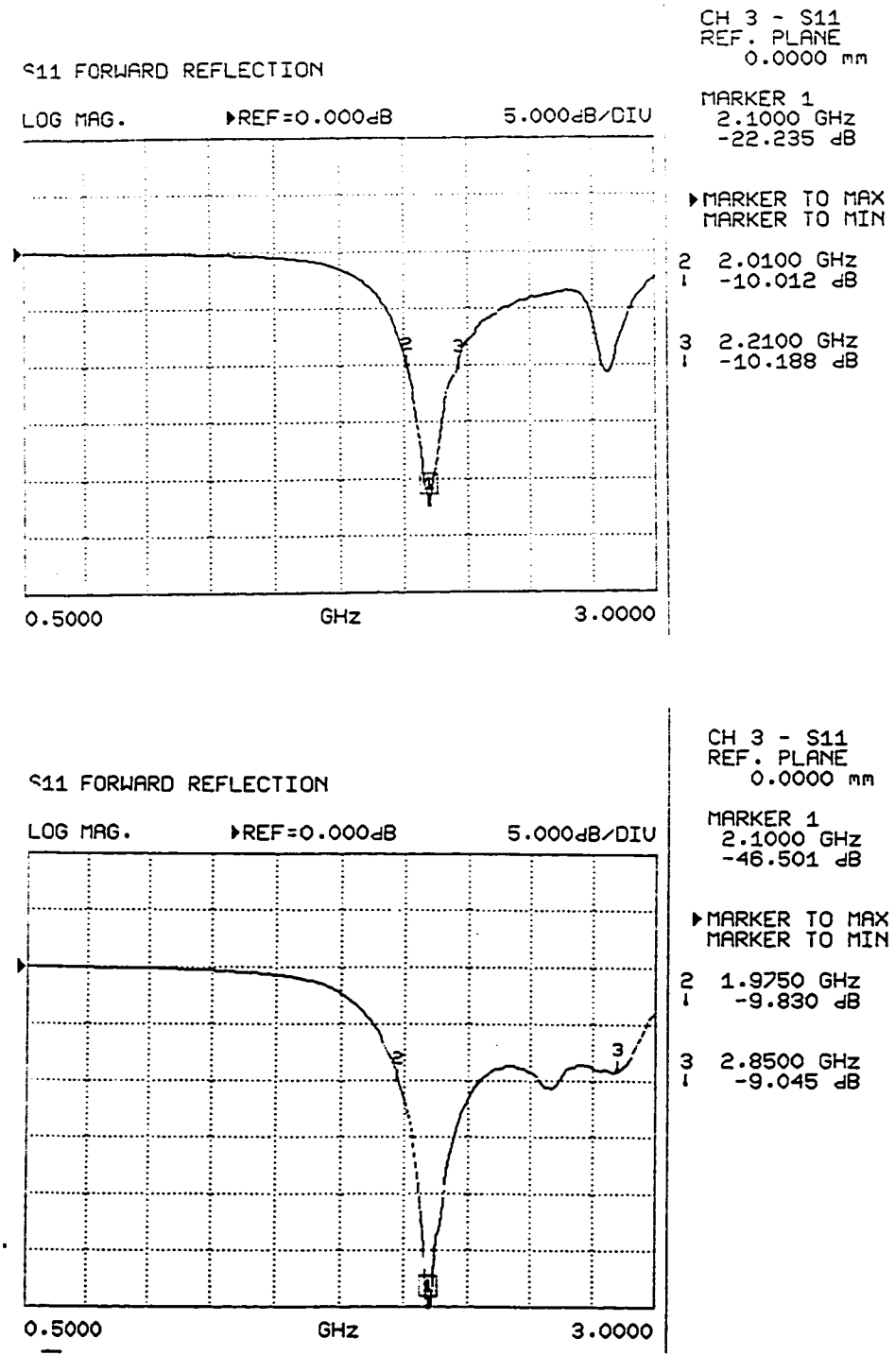

E.3 Broad Band Measurement of Multi-Segment DRA Based on D25M with Limiting Mode Resonances Visible

Lower Segment Height = 0.5 cm (Top), 1.0 (Bottom)

Appendix F
Edge-Grounded Rectangular DRA Measurements

F.1 Radiation Pattern Measurements for Edge-grounded DRA based on D25S segment

F.2 Comparison of Network Analyser Measurements for Regular, Edge-grounded and Edge-grounded Multi-Segment Rectangular DRA based on D25S Segment

F.3 Network Analyser Measurement Results for Compact Broad Band Edge-grounded Multi-segment DRA Based on D10L3 Segment

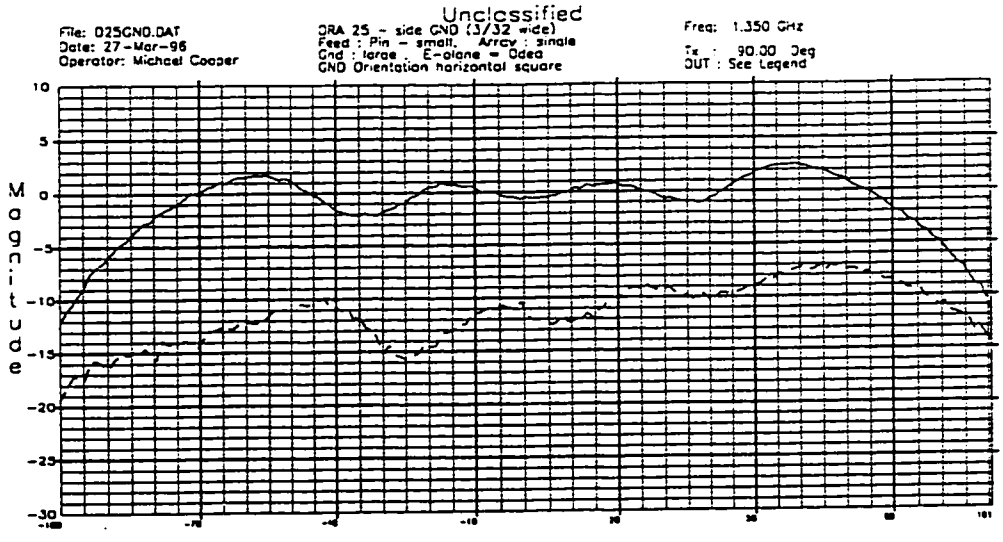

Radiation Pattern : E-Plane

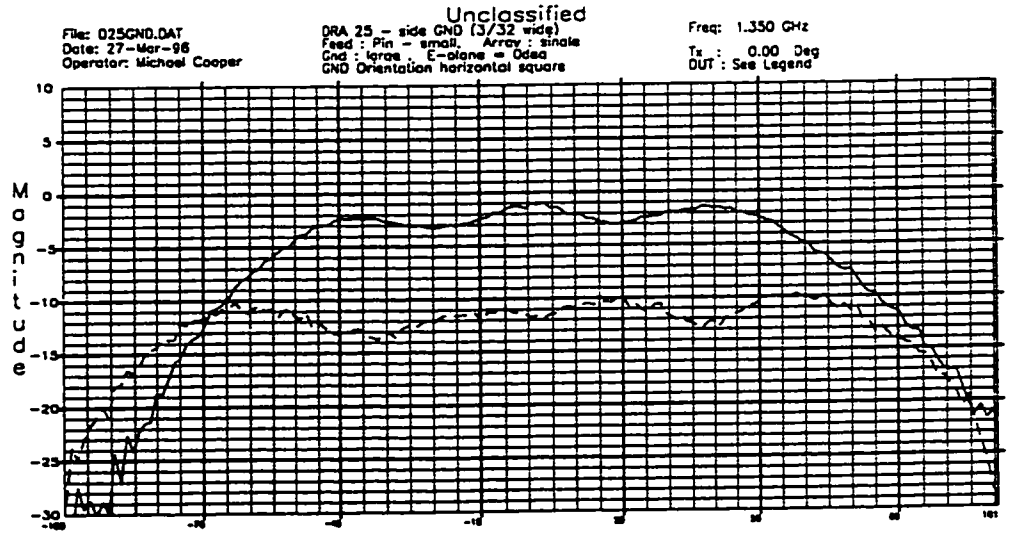

Radiation Pattern : H-Plane

F.1 Radiation Pattern Measurements for Edge-grounded DRA based on D25S segment (Tape covers centre third of DRA sidewall)

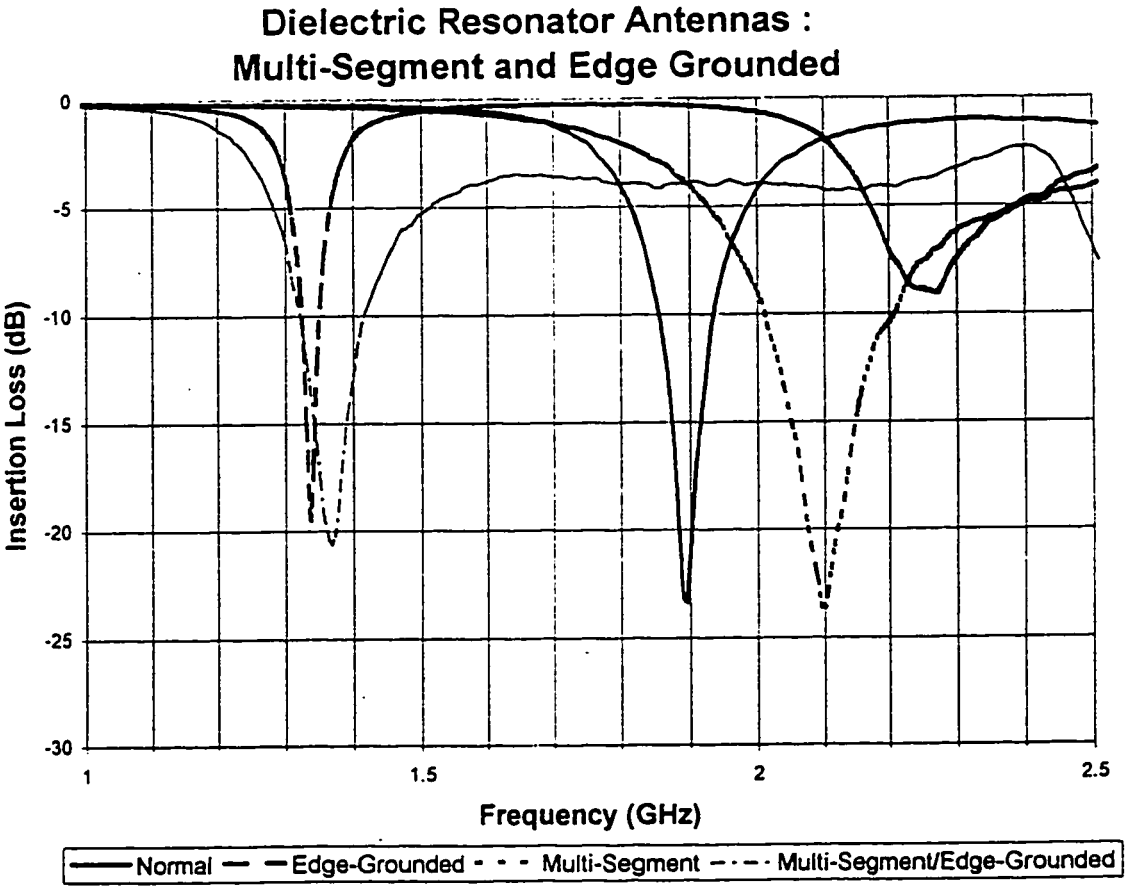

F.2 Comparison of Regular, Edge-grounded and Edge-grounded Multi-Segment Rectangular DRA based on D25S Segment Lower Segment Height = 0.5 cm, Dielectric Constant = 4.0

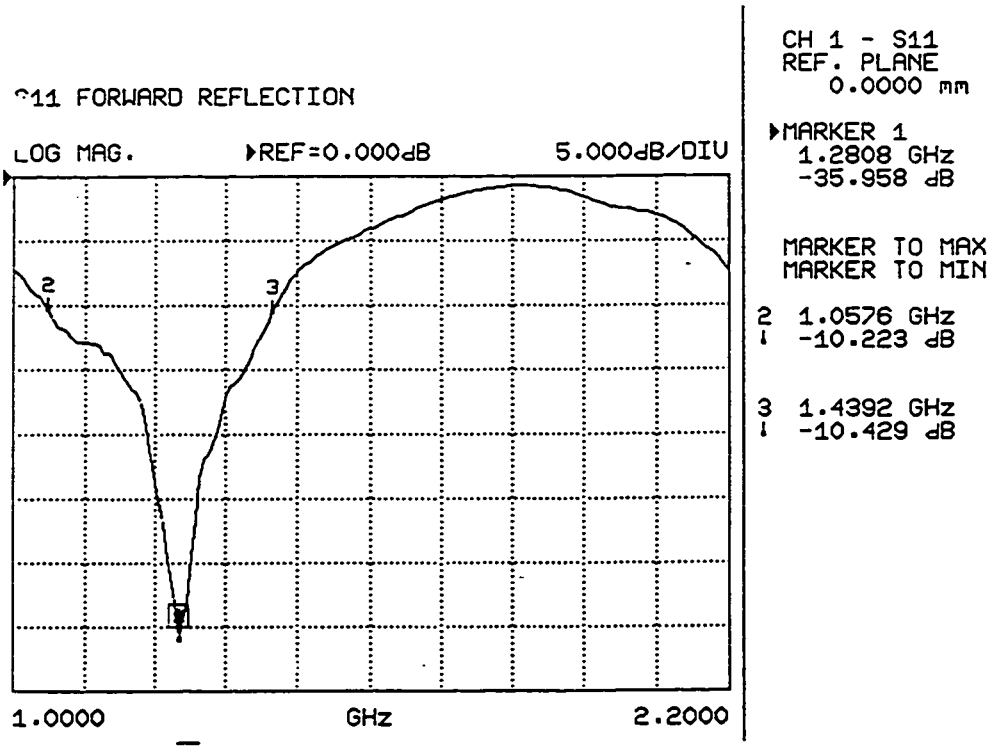

F.3 Measurement Results of Compact Broad Band Edge-grounded Multi-segment DRA Based on D10L3 Segment

Lower Segment Height = 1.0 cm, Dielectric Constant = 4.0

IMAGE EVALUATION
TEST TARGET (QA-3)

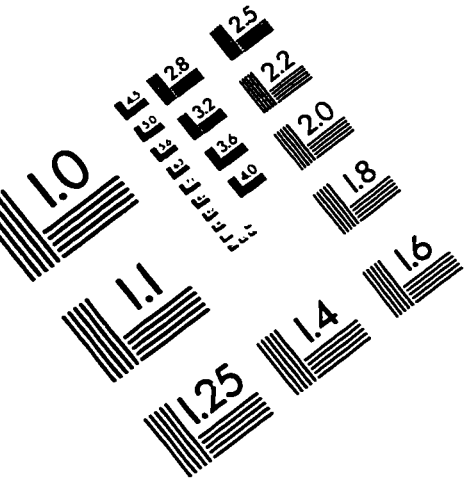

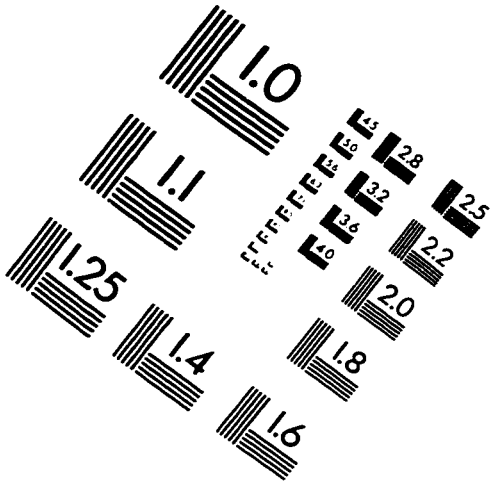

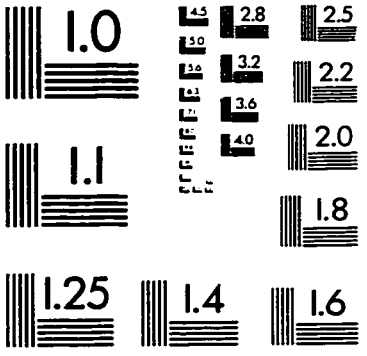

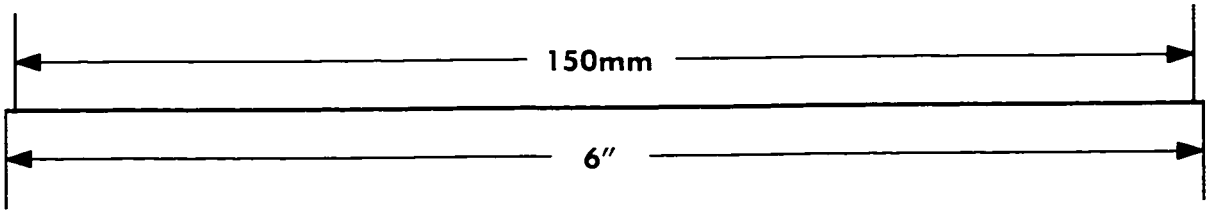

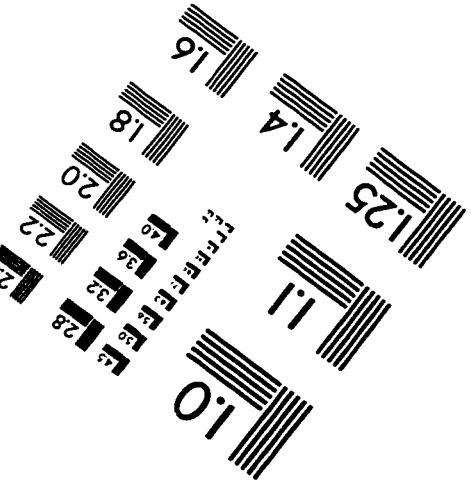

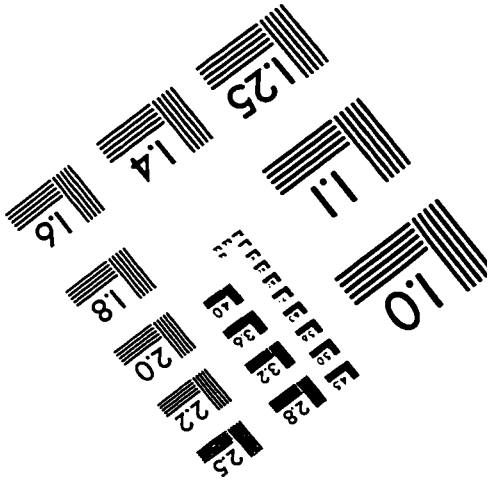

APPLIED IMAGE, Inc
1653 East Main Street
Rochester, NY 14609 USA
Phone: 716/482-0300
Fax: 716/288-5989